Solvent ordering near cyclohexadienyl type radicals, and ferroelectric ordering of pyridinium perchlorate

Von der Fakultät Chemie der Universität Stuttgart zur Erlangung der Würde eines Doktors der Naturwissenschaften (Dr. rer. nat.) genehmigte Abhandlung

vorgelegt von

Dipl.-Chem. Danilo Vujosevic
aus Belgrad, Serbien

Hauptberichter:	Prof. Dr. Emil Roduner
Mitberichter:	Prof. Dr. Klaus Müller

Tag der mündlichen Prüfung: 24.01.2007

Institut für Physikalische Chemie der Universität Stuttgart, 2007

Eidesstattliche Erklärung

Ich versichere, dass ich diese Dissertation selbständig verfasst und nur die angegebenen Quellen und Hilfsmittel verwendet habe.

Stuttgart, 31.10.2006 Danilo Vujosevic

Contents

1 Introduction, objectives and methods of the work

1.1 Introduction

Free radicals play a very important role in everyday life. They serve in our immune system against invading bacteria and viruses, and cells use free radicals in communication with each other.[1] However, when present in too high concentrations free radicals can become harmful. Oxidative damage by free radicals is involved in almost every major disease.[2] Production of free radicals in living organism is stimulated by UV radiation, aging, disease, physical and emotional stress, an unhealthy environment, etc. When oxidized, DNA, proteins, lipids, and other important biochemical molecules deviate from their normal function and may even become harmful.[3] For example, damaged DNA may provide the wrong genetic code leading to unregulated protein synthesis and/or cell growth, which may result in cancer. Free radicals also play a very important role in various processes of importance for industry such as polymer synthesis,[4] polymer degradation,[5] fuel cell membrane degradation,[6] materials aging, etc. Common for most of these interactions is that they take place in the liquid or amorphous phases. For this reason it is of great importance to understand the underlying mechanisms of free radicals' interaction with their environment in the liquid phase.

The interaction of the solutes' electric dipole moment with the solvent consisting of molecules with dipole moments leads to a partial orientation of the surrounding solvent molecules. Additional dipole moment at each nearby solvent molecule is induced, as well. The result of these orientational and induction effects is that the vicinity of the solute becomes polarized.[7] The polarized solvent molecules in the vicinity of the solute generate an electric field (*reaction field*) at a solute molecule. The reaction field may also originate in other electrostatic interactions (dipole-induced dipole, induced dipole-induced-dipole, dipole-quadrupole, etc.). The reaction field in return, influences the solute molecules' properties making them different from that in gas phase. These effects are called *solvent effects*, and they are of paramount importance, since most of

the chemistry and biochemistry takes place in a solution. Solvent effects can influence the charge distribution, structure, conformational choice and many other properties of the solute molecule, thereby affecting the reaction rates, chemical equilibrium, IR, UV, and NMR spectra, etc.[8]

Solvent effects can sometimes have a tremendous effect on free radical reactions.[3] An appropriate solvent can significantly increase the rate of formation and the product yield in organic synthesis.[9–11] The changes in reaction rates are the result of solvent stabilization of reactants or transition states, accompanied by changes in their geometric and electronic structures. The hyperfine coupling constants (hfcs) are a sensitive means of examining the electronic structure of a radical and monitoring how this is altered through solvent interactions.

There have been many studies of solvent effects on stable free radicals such as di-tert-butyl-nitroxide (DTBN), and the results have been typically interpreted in terms of a reaction field model. Solute-solvent interactions are most commonly described by various continuum models,[12] basically inspired by those of Onsager[13] and Kirkwood.[14] Common for all of them is that they use the solvent dielectric constant as the property that determines the solute-solvent interaction. For example, when applying the continuum model approach to radicals, Al-Bala'a et al. found that the hfc correlates linearly with (ε-1)/(ε+1), where ε is the solvent dielectric constant.[15] Recently, the conventional theoretical dielectric continuum description of dipolar solvents has been extended to include effects arising from the molecular quadrupole moment of non-dipolar solvents,[16] but the treatment has not been tested for its suitability to describe solvent effects on hyperfine couplings. The main problem with most continuum solvation models is that the interaction energy saturates too quickly with increasing ε and that they do not take explicit solute-solvent interactions into account. Further criticisms can be found elsewhere.[17] Improvements in using the continuum model have been made by calculating a ´local´ dielectric constant,[18] but in this sense ε loses its meaning, since it is defined as a property of the bulk liquid. Once solvation is understood the hfc may be used as a probe of the radicals' environment.[19,20] There is a need for a more general model that describes the effects of solvent molecules on the electronic structure of radicals and of molecular solutes in general. In this sense, a dipole-dipole reaction field model of Reddoch and Konishi (henceforth abbreviated as RK) developed to account for the solvent depedence of ^{14}N hfc in di-tert-butyl-nitroxide radical (more details in Chapter 4) offers advantages in comparison to the continuum solvation models.[17]

Most of the free radicals of interest in nature and in industrial processes contain more than one functional group.[3] In this case interaction of these radicals with the

solvent is typically influenced by more factors such as conformation, properties of functional groups, etc. The conformation of the flexible solute molecule is often significantly changed in different solvents,[21,22] and analogously the solvent may also influence the radical conformation.[3] It is well known that a radicals' conformation may significantly affect its hfcs[23] and some free radical reactions.[24]

A sufficient and systematic understanding of molecular structure-physicochemical properties relationship is a basic requirement for design of new materials and processes. The ferroelectricity is the electrical phenomenon where a material exhibits a spontaneous electric polarization (dipole moment), which can be reversed by the application of an electric field. There are basically two classes of ferroelectric materials, a sublattice displacement type (centers of positive and negative charges of the unit cell shift from the equilibrium position) and an order-disorder type (dipole moments in the unit cell orient in the same direction inside the ferroelectric domain). However, in many materials ferroelectricity is of mixed origin.[25]

The ferroelectric materials are of interest in many microelectronic and micromechanical applications.[26,27] In the design of new ferroelectric materials, the main aim is to synthesise a material that exhibits ferroelectricity at the highest achievable temperature. Controlling the phase transition temperatures of ferroelectric and antiferroelectric materials has implications in other fields of science and industry, as well.

1.2 Objectives

One of the objectives in this work is to further develop the dipole-dipole reaction field model of RK[17] and to apply it to describe the solute-solvent interactions for the cyclohexadienyl radical (C_6H_7) and this is presented in Chapter 4. C_6H_7 is of interest in itself in that it is an intermediate in many chemical reactions.[28,29] More precisely the methylene proton hfc (A_p^{met}) of C_6H_7 was studied since it is the largest, making it the most suitable for studying the solvent effects that usually give small relative shifts of the hfc.[17,30] A_p^{met} of C_6H_7 is studied in the gas phase and in neat benzene over a wide temperature range,[31–34] but there is no information on the hfcs in other solvents.

After examining the solvent effects on C_6H_7, in order to be systematic it is informative to move one step further and to study the solvent effects on substituted cyclohexadienyl radicals. More precisely, the hydrogen adducts to 2-phenylethanol (PEA) and 5-phenylpentanol (PPA) were studied. These radicals are interesting as their parent molecules, PEA and PPA mimic molecules that have an important role in various biochemical and industrial processes. PEA in particular models many simple

biomolecules.[35] The hydrogen adduct radicals derived from the PEA and PPA (more precisely their muoniated isotopologues henceforth abbreviated as PEA-Mu and PPA-Mu), were previously used for monitoring the distribution of PEA and PPA between the surfactant micelles (cell membrane-like environment) and the water[19,20] with Muon Spin Resonance technique (μSR).[36] These radicals and this technique were proposed recently to be used for monitoring the drug partitioning between the cell fluids and lipid-like environments of a cell membrane.[37] But the question of their behaviour in isotropic liquids requires to be studied in detail and this is described in Chapter 5. The information of interest will be extracted by monitoring the relative behaviour of $A_{\mathrm{p}}^{\mathrm{met}}$ of PEA-Mu and PPA-Mu radicals. The absolute values of $A_{\mathrm{p}}^{\mathrm{met}}$ were also reported in Chapter 5, as they may be of interest in other studies.

The hfcs of PEA-Mu and PPA-Mu radicals are expected to be influenced by the conformation of the substituent hydroxyalkyl group. For this reason, a study of intramolecular hydrogen bonding and conformation of PEA-Mu and PPA-Mu radicals in water, methanol and octadecane was undertaken and presented in Chapter 6. In particular, in this part of the work, the focus is on the β-methylene protons hfcs (A_{p}^{β}) as the information about the preferential conformation of these radicals can be extracted from their temperature behaviour using the McConnell relations (described in section 2.1). However these hfcs were not yet monitored using the μSR technique and this is performed in this work for the first time. The hfcs of other in-plane protons will be presented in this chapter, as well.

One of the intentions in this work is to correlate the properties and the motions of individual molecules with the measurements of macroscopically observable phenomena. Pyridinium salts represent a very good example for studying the orientational ordering as an origin of the ferroelectricity, due to the pronounced electric dipole moment of the pydirinium cation. The pyridinium cation is of symmetry very similar to that of benzene and this fact simplifies the theoretical treatment. Since the recent discovery of ferroelectricity among pyridinium salts,[38] a lot of structural data was gathered, studies of ferroelectric properties were conducted and these data were used in this work. For these reasons, ferroelectricity of the pyridinium-perchlorate is studied in Chapter 7.

The relationship between the structure of individual ions in the crystal and the phase transition temperatures for the case of ferroelectric and nonferroelectric pyridinium salts is studied in Chapter 8. The paraelectric-ferroelectric phase transition temperatures in the family of pyridinium salts are compared and the influence of anions on the ferroelectricity is examined with the help of ab initio calculations. Factors influencing the appearance of ferroelectricity and the character of the phase transition

are also discussed.

1.3 Methods

The experimental studies of cyclohexadienyl type radicals are typically very challenging. In the case of C_6H_7 this is due to its high reactivity and the difficulty in producing it.[39] It has been observed by electron paramagnetic resonance upon irradiation of 1,4-cyclohexadiene[40] and solid benzene, but the temperature range and solvents in which it could be studied are extremely limited. The formation of other cyclohexadienyl radicals is even more complicated. A technique that allows very simple formation and monitoring of the cyclohexadienyl type radicals is μSR. For the purpose of formation and monitoring of the organic radicals this technique uses the light hydrogen isotope, Muonium (Mu), instead of "ordinary" hydrogen atom. It is advantageous to study the muoniated isotopologue of the cyclohexadienyl radical (C_6H_6Mu), as this radical can be easily produced in many different solvents and over a wide temperature range. In some cases it is necessary to distinguish between the muoniated and non-muoniated isotopologues as the light mass of Mu can have a large effect on the structure and dynamics. The effect of Mu substitution on the C_6H_7 radical is well understood. The main effect is that the C-Mu bond is elongated by approximately 4.9% due to the increased zero-point energy while the methylene proton bond is almost unchanged.[32] This allows to directly relate A_p^{met} of C_6H_6Mu to that of C_6H_7. The same argumentation as for C_6H_7 remains valid and allows the direct correlation of hfcs of the muoniated isotopologues to that of the "normal" hydrogen adducts to PEA and PPA. More details about the μSR technique may be found in section 2.2.1.

An excellent technique for studying the dynamics of molecules in the solids is ^{2}H NMR, as the interaction of the deuterium (heavy hydrogen isotope) nuclear electric quadrupole moment with the electric field gradient in the chemical bond dominates the solid-state NMR spectrum.[41] This means that the molecules studied have to contain deuterium instead of "ordinary" hydrogen atoms. The deuterium is the nonperturbing probe and its presence instead of "normal" hydrogen has negligible effects on the structure and dynamics. The dynamic range of ^{2}H NMR is large and the effect of various types of motion on the NMR spectra and relaxation is well understood.[42,43] More details about this technique may be found in section 2.2.2.

Many properties of molecules of interest (energies of radicals, influence of electric field on hfcs, polarizabilities of anions and their partial charges, etc.) were necessary for this work, but it was experimentally very challenging or impossible to measure

these properties. On the other hand, the recent significant progress in computational chemistry recommends ab initio calculations as a valuable additional tool when the experimental techniques cease to be applicable. So the ab initio calculations were widely used in this work, as they offer very informative results. More details about the ab initio calculations are available in the section 2.2.3.

2 Basics

2.1 Hyperfine coupling constants, McConnell relations

2.1.1 Hyperfine coupling constants

A fast reorientation of free radicals in isotropic liquids averages out all anisotropies. In this case, the isotropic Hamiltonian describes the magnetic interactions of the molecule with the unpaired electron. The isotropic Hamiltonian consists of the electron Zeeman term, a Zeeman term for each nucleus and an electron-nuclear hyperfine coupling term. In SI units it is given as

$$\hat{H} = \gamma_{\mathrm{e}} \hbar B_0 \hat{S}_{\mathrm{z}} - \sum_{\mathrm{n}} \gamma_{\mathrm{n}} \hbar B_0 \hat{I}^{\mathrm{n}}_{\mathrm{z}} + \sum_{\mathrm{n}} h A_{\mathrm{n}} \hat{S} \hat{I}^{\mathrm{n}} \ , \tag{2.1}$$

where γ_{e} and γ_{n} are the electron and nuclear (of the nucleus n) gyromagnetic ratios, B_0 is the external magnetic field in the z direction and h is the Planck's constant.[44] Moreover, $\hat{S}$ and $\hat{I}^{\mathrm{n}}$ are the electron and nuclear spin operators (z denotes the z-component) and A_{n} is the hyperfine coupling constant (hfc) of the nucleus n.

Electron-nuclear hyperfine coupling terms play a role only in free radicals. The information about the interaction of the nucleus n with the unpaired electron is contained in the hfc, A_{n}. The hfc characterizes the interaction energy between the unpaired electron spin and the magnetic moment of the nuclei. The hfcs are sometimes expressed in units of joules, but more often in units of MHz as is done in this work, or in units of Gauss (typically in Electron Paramagnetic Resonance).

The hfc consists of an isotropic and an anisotropic term. The anisotropic term is averaged out in isotropic liquids. The isotropic term is directly proportional to the square of the wavefunction amplitude of the unpaired electron at the position of the

nucleus n. This interaction is named the Fermi contact interaction:

$$A_{\mathrm{n}} = \frac{2\mu_0}{3h}\gamma_{\mathrm{e}}\gamma_{\mathrm{n}}\hbar^2|\Psi(\vec{r}=0)|^2 \ , \tag{2.2}$$

where μ_0 is the vacuum permeability.[44] The spin density in the volume element, $\rho(\vec{r})$, is defined as the electron density difference between electrons with spin α and spin β as

$$\rho(\vec{r}) = \rho^{\alpha}(\vec{r}) - \rho^{\beta}(\vec{r}) \ . \tag{2.3}$$

The spin population is defined as the integrated spin density over all orbitals at the position of the nucleus. The terms spin density and spin population are often used interchangeably. When this is included into eq. 2.2, the hfc is proportional to the spin population $\rho_{\mathrm{n}}^{\mathrm{spin}}$ at the position of nucleus n as

$$A_{\mathrm{n}} = \frac{2\mu_0}{3h}\gamma_{\mathrm{e}}\gamma_{\mathrm{n}}\hbar^2\rho_{\mathrm{n}}^{\mathrm{spin}}(\vec{r_{\mathrm{n}}}) \ . \tag{2.4}$$

The spin of the unpaired electron in a singly occupied molecular orbital (SOMO) polarizes the doubly occupied molecular orbitals.[45] This has the effect, that in doubly occupied molecular orbitals at certain atoms there is more electron spin α and at others there is more electron spin β. The unpaired electron spin α polarizes the core orbitals of the atom and the doubly occupied molecular orbitals in a way that it enhances the α spin population at the nucleus position, at the cost of the neighboring atoms. The SOMO is usually the key orbital that determines the spin population distribution and also the spin polarization in organic free radicals.[46]

The dependence of the spin population at the α and β protons' positions is described by the McConnell relations.[45] The McConnell relations are important because they allow one to extract the information about the preferred conformation of the radical and the spin populations at different nuclei in the free radical.

2.1.2 The McConnell relation for α-protons in planar π-radicals

The hfc of the α proton at the planar radical center is proportional to the π-electron spin population at the neighbouring carbon,[45]

$$A_{\mathrm{p}}(\mathrm{H}_{\alpha}) = Q_{\mathrm{H}}^{\alpha}\rho_{\pi} \ , \tag{2.5}$$

where $A_{\mathrm{p}}(\mathrm{H}_{\alpha})$ is the hfc of the α protons, Q_{H}^{α} the empirical proportionality parameter (it may vary a lot depending on the radical structure) and ρ_{π}, the π-electron spin

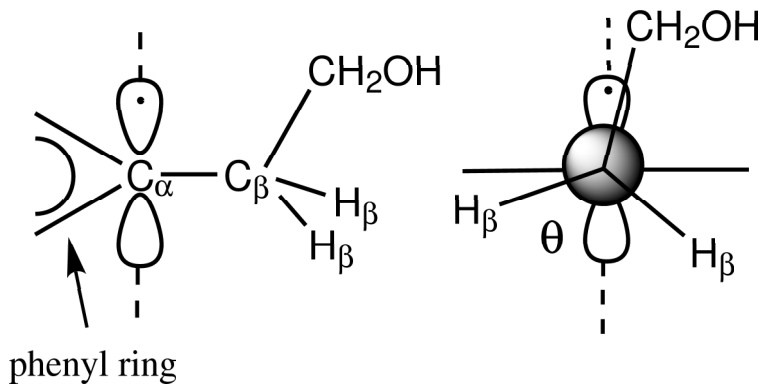

Figure 2.1: Conformation of PEA-Mu radicals - side view (left) and Newman projection (right). θ represents the dihedral angle between the p_z orbital axis and the plane containing the C_α, C_β and H_β atoms.

population on the neighbouring carbon atom, C_α.

2.1.3 The McConnell relation for β-methyl protons in π-radicals

This relation describes the angular dependence of the β-methyl proton hfc.[45] It is given as

$$A_{\mathrm{p}}^{\beta} = \rho_{\pi}(A + B\langle\cos^2\theta\rangle) \ , \tag{2.6}$$

where A_{p}^{β} is the β-methyl proton hfc. The constant A represents the small contribution due to the spin polarization that shows no angular dependence. B is the prefactor for the hyperconjugative contribution. θ is the averaged dihedral angle between the p_z orbital axis and the plane containing the C_α, C_β and H_β atoms, as shown in Figure 2.1. The temperature dependence of the A_{p}^{β} provides information about the preferred conformation, as shown in Figure 2.2. An increased value of A_{p}^{β} indicates that the substituent group is preferably eclipsed to the p_z orbital of the C_α atom ($\langle\cos^2\theta\rangle<1/2$; Figure 2.2). On the other hand, the decrease of A_{p}^{β} with increasing temperature indicates that the substituent group is preferably staggered to the p_z orbital of the C_α atom ($\langle\cos^2\theta\rangle>1/2$; Figure 2.2). A constant value of A_{p}^{β} means that the rotation of the substituent group is at the free rotation limit ($\langle\cos^2\theta\rangle=1/2$) where all the protons are equivalent.

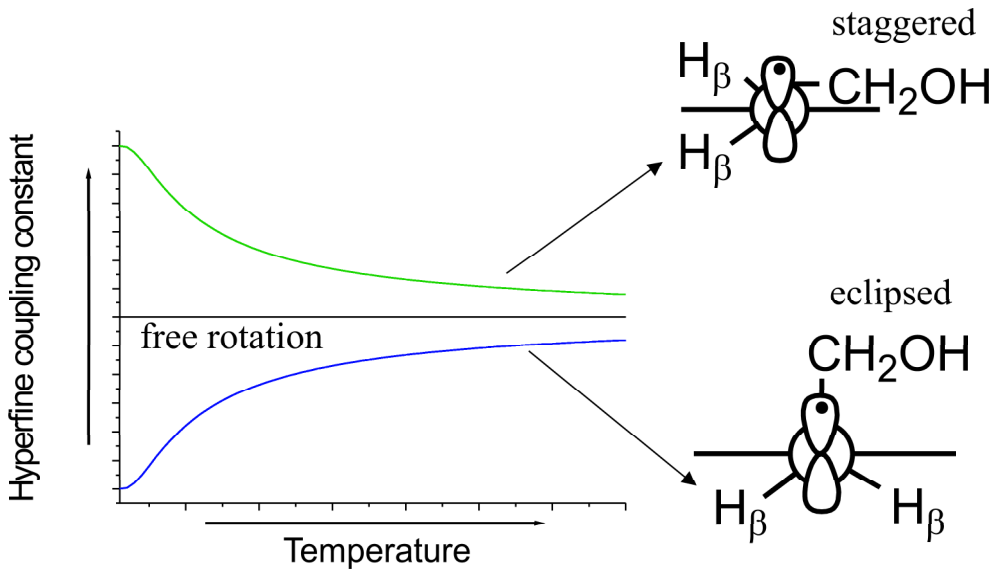

Figure 2.2: The temperature dependence of A_{p}^{β} and the corresponding preferential orientations of the substituent group (upper part of the figure: the substituent group staggered to the p_z orbital of the C_α atom, lower part of the figure: the substituent group eclipsed to the p_z orbital of the C_α atom).

2.2 Techniques

2.2.1 Muon spin resonance

2.2.1.1 Production and Decay of Muons

In nature, muons are formed by the collisions of cosmic rays with nuclei in the upper parts of the atmosphere. However, due to their importance in science, muons are also artificially produced in accelerator facilities. Typically this is performed by colliding protons with the appropriate energy with targets containing light nuclei, for example carbon, as in Figure 2.3. As a product of this process, the positive pion (π^+) is formed. It decays to a neutrino (ν_μ) and a positive muon (μ^+). π^+ is a spin 0 particle, whereas the neutrino is a spin 1/2 particle with a magnetic moment that is oriented antiparallel to the direction of the angular momentum (negative helicity). Due to the conservation laws, μ^+ must also be a spin 1/2 particle with negative helicity. For these reasons beams of mono-energetic muons come out almost 100% spin-polarized. The production of muons takes place at several accelerator facilities throughout the world: PSI-Switzerland, ISIS-UK and TRIUMF-Canada.

The positive muon (μ^+) is an elementary particle with a spin of 1/2, a mean lifetime of 2.2 μs, a mass approximately one-ninth that of a proton (207 times that of

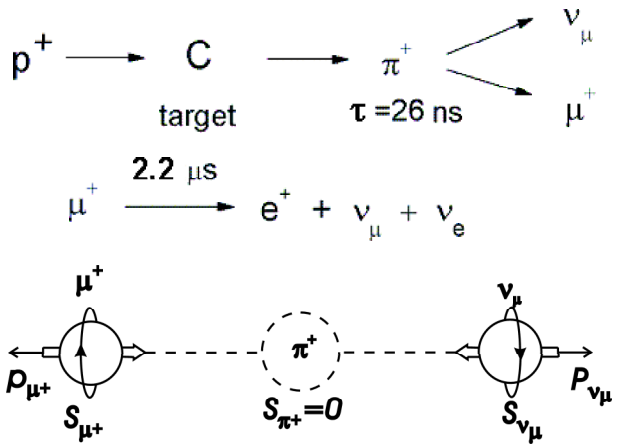

Figure 2.3: The production and decay of muons.

Table 2.1: Muonium and hydrogen atomic properties.[47]

Isotope	Mass / amu	Ionisation potential / eV	Bohr radius / pm	Spin	Magnetic moment / au
H	1	13.598	52.97	1/2	1
Mu	0.11	13.539	53.17	1/2	3.181

an electron) and a magnetic moment 3.18 times that of a proton. Thus, μ^+ is a very sensitive magnetic probe. Muons can be easily implanted into solid, liquid or gaseous samples and are widely used to probe magnetic phenomena.[47] A fraction of implanted muons can pick up an electron during the radiolysis process to form a one-electron hydrogen-like atom called muonium (Mu = [μ^+, e^-]). The Bohr radius and ionization potential of H and Mu are almost the same, as shown in Table 2.1. This implies that their chemical properties are also almost the same, so Mu can be considered an isotope of H, just like D or T. Mu can add itself to unsaturated bonds of organic molecules to produce an organic radical (called a muoniated radical), as in Figure 2.4, with the muon acting as a polarized spin label.[47] The muon decay, which violates parity, produces a positron (e^+) and two neutrinos. The violation of parity causes the positron to be emitted preferentially along the direction of the muons spin, as shown in Figure 2.5.

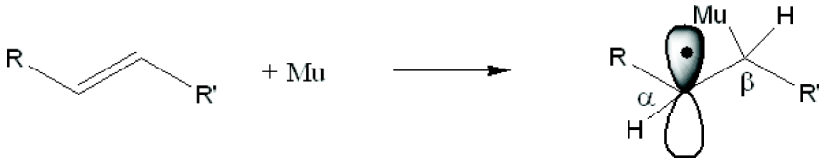

Figure 2.4: Muonium addition to the double bond.

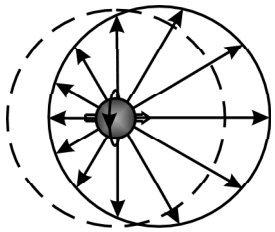

Figure 2.5: Muon decay. Arrows denote the possible directions of decay positrons (the anisotropy of muon decay). The relative probabilities of the positron decay directions are proportional to the arrow length. The dashed line represents the relative probabilities for case where the muon decay would be isotropic.[48]

The detection of the decay positrons as a function of time provides a convenient means of monitoring the evolution of the muons' spin. The information of interest is extracted by monitoring the anisotropy of muon decay.

2.2.1.2 Avoided Level Crossing Muon Spin Resonance

The Muonium atom (Mu) is considered to be a two-spin-1/2 system characterized by the corresponding Hamiltonian consisting of the electron and nuclear Zeeman term, and of the electron-nuclear hyperfine coupling term as[47]

$$\hat{H} = \gamma_{\mathrm{e}}\hbar\hat{S}_{\mathrm{z}} - \gamma_{\mu}\hbar\hat{I}^{\mu}_{\mathrm{z}} + \mathrm{h}A^{\mu}_{0}\hat{S}\hat{I}^{\mu} \ . \tag{2.7}$$

The electron and muon are coupled by the isotropic hfc of the muon, A_{μ}.

The particular situation in Avoided Level Crossing (ALC) Muon Spin Resonance (μSR) arises from the presence of a considerable number of other magnetic nuclei n, apart from the muon, which are also coupled to the unpaired electron. The corresponding spin Hamiltonian has to include additional interactions. It is given by

$$\hat{H} = \gamma_{\mathrm{e}}\hbar\hat{S}_{\mathrm{z}} - \gamma_{\mu}\hbar\hat{I}^{\mu}_{\mathrm{z}} + hA^{\mu}_{0}\hat{S}\hat{I}^{\mu} - \sum_{\mathrm{n}}\gamma_{\mathrm{n}}\hbar\hat{I}^{\mathrm{n}}_{\mathrm{z}} + \sum_{\mathrm{n}}hA^{\mathrm{n}}_{0}\hat{S}\hat{I} \ . \tag{2.8}$$

In Figure 2.6 a high magnetic field energy diagram of the three-spin-1/2 system is shown.

Over most of the field range no interaction takes place. But at specific values of the applied magnetic field, nearly degenerate pairs of spin states can mix through the hyperfine interaction, causing the oscillation of muons between two mixing states, leading to the loss of initial muon polarization. There are three types of ALC reso-

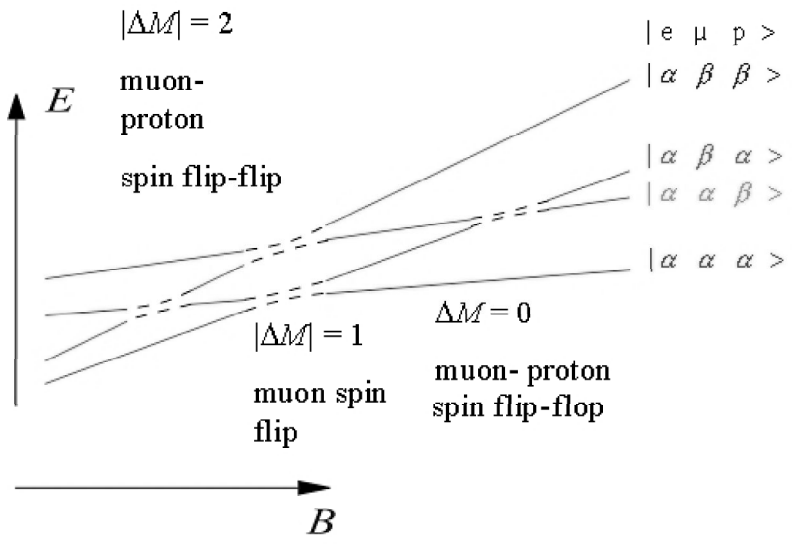

Figure 2.6: High field energy diagram of the three-spin-1/2 system (courtesy of Dr. R. Scheuermann).

nances, denoted Δ_0, Δ_1 and Δ_2, where the subscript refers to the change of M, the quantum number of the z-component of the total spin (sum of the quantum numbers for the z-components of the muon and nuclear spins), as shown in eq. 2.9.

$$\Delta M = \Delta m_\mu + \Delta m_\mathrm{p} \ , \tag{2.9}$$

where m_μ and m_p are quantum numbers of the z component of the muon and proton spin, respectively.

Δ_0 ALC resonances arise from the isotropic part of the hyperfine interaction and they are observable in isotropic and anisotropic environments. Δ_1 and Δ_2 arise from the dipolar part of the hyperfine interaction and they are observable only in anisotropic environments. The resonance position of the Δ_0 ALC resonance is dependent on the muon (A_μ) and proton (A_p) hfcs, as in eq. 2.10.[47]

$$B_\mathrm{r}(\Delta_0) = \frac{|A_\mu - A_\mathrm{p}|}{2(\gamma_\mu - \gamma_\mathrm{p})} - \frac{A_\mu + A_\mathrm{p}}{2\gamma_\mathrm{e}} \ , \tag{2.10}$$

where γ_μ, γ_p and γ_e are the muon, proton and electron gyromagnetic ratios, respectively.

The main advantage of the ALC-μSR technique is that it can be used in very dilute samples. The second advantage is, that with the ALC-μSR technique more than one magnetic nucleus may be monitored, if there is enough spin population at its

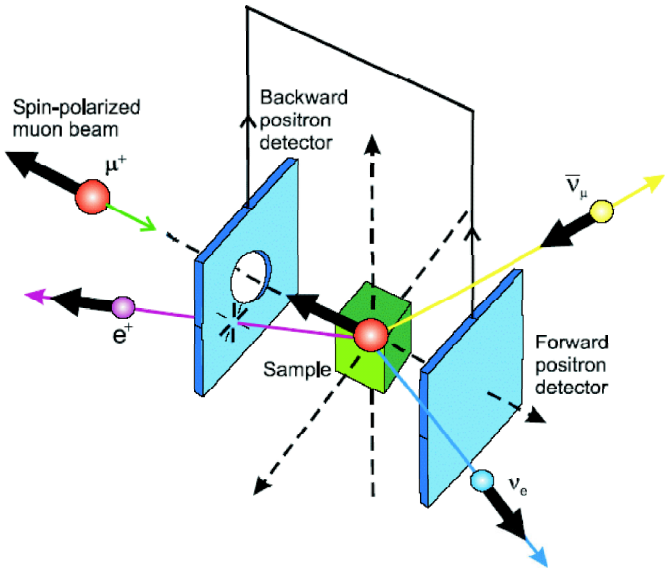

Figure 2.7: The ALC-μSR experiment.[49]

position.

In the ALC-μSR experiment, muons are injected into the sample with their spins parallel to the magnetic field (Figure 2.7). A muon spends some time in the sample, during which it may interact with its environment. Afterwards it decays producing a positron and a neutrino. Positron detection is then used to monitor the anisotropy of muon decay. The ALC-μSR technique is run in a time-integral mode, i.e. the number of positrons emitted in the forward and backward directions with respect to the incoming muon beam (N_f and N_b, respectively) is counted as a function of the applied magnetic field. The asymmetry is given by:[47]

$$Asym. = \frac{N_\mathrm{f} - N_\mathrm{b}}{N_\mathrm{f} + N_\mathrm{b}}. \tag{2.11}$$

In the case of no interaction the asymmetry remains constant, but at some magnetic fields an interaction takes place resulting in a resonant-like change in the asymmetry as the magnetic field is swept (examples in Figures 4.4, 5.2 and 5.3). The amplitude of the Δ_0 ALC resonance is given by:

$$I \propto \frac{\omega^2}{\omega^2 + {\lambda_\mathrm{eff}}^2}\ , \tag{2.12}$$

where λ_eff is the effective relaxation rate (muon decay rate plus any other relaxation contribution) and ω is the transition frequency between two spin states at resonance given by:[50]

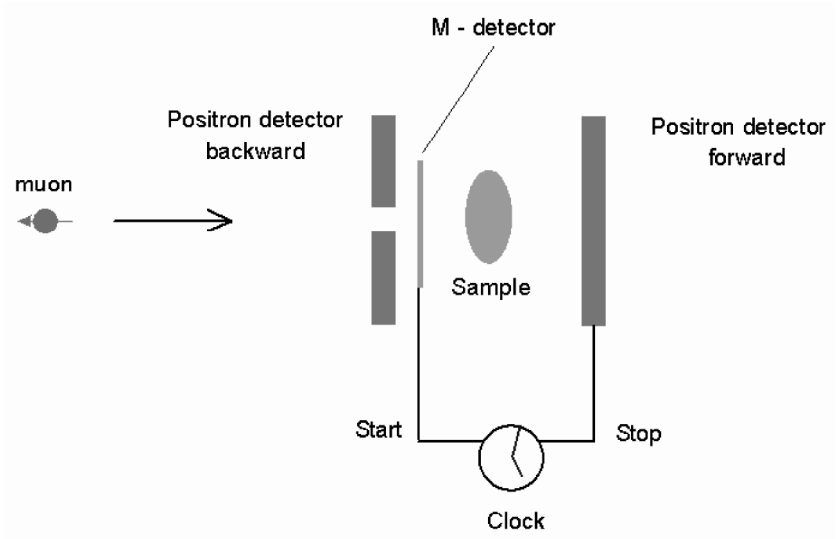

Figure 2.8: The principal scheme of a TF-μSR experiment (courtesy of Dr. H. Dilger).

$$\omega = \frac{\sqrt{c}\pi A_\mu A_\mathrm{p}}{\gamma_\mathrm{e} B} \ , \tag{2.13}$$

where c is the number of magnetically equivalent protons at resonance.

2.2.1.3 Transverse Field Muon Spin Resonance

In this type of μSR experiment muons enter the magnetic field with their spins perpendicular to the magnetic field. This technique runs in the time differential mode. Each arrival is detected in the muon counter, which starts a clock for measurement of the individual muon lifetimes (detector M in Figure 2.8). The clock is stopped when the corresponding decay positron is detected in the backward or forward detector and the event is stored in the histogram, $F(\mathrm{t})$. There are two histograms, forward and backward with respect to in which counter the decay positron is detected. In the histogram the number of decay positrons is stored as a function of the time that muon spent in the sample, as shown in Figure 2.9. In the absence of any time evolution of muon polarization $F(\mathrm{t})$ is simply the radioactive decay curve a of muon. In a nonzero magnetic field the muon undergoes a free induction decay (FID), similar to the response after a $\pi/2$ pulse in conventional magnetic resonance. Due to the decay anisotropy the FID appears in the histogram superimposed on the muon decay curve. In Figure 2.10, the Breit-Rabi diagram of a two-spin-1/2 system (μ^+ and e^-) is presented. The different oscillation frequencies relate to the transitions between the different magnetic energy levels in the muoniated adduct radical. Muoniated organic free radicals are usually

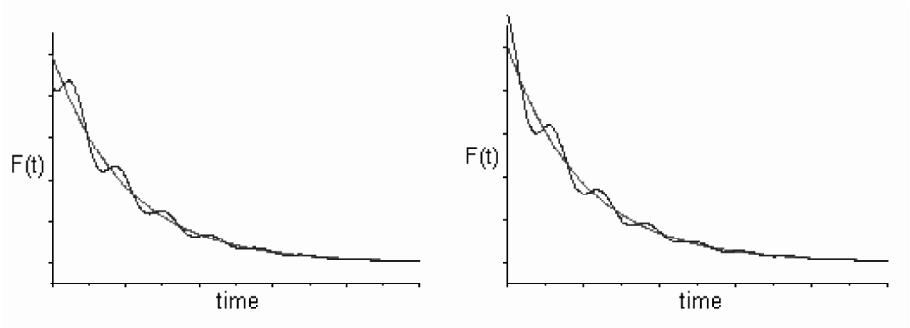

Figure 2.9: Backward (left) and forward (right) histograms.

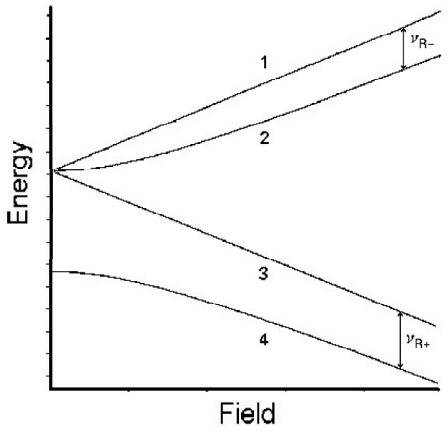

Figure 2.10: Breit-Rabi diagram for muonium with transitions indicated by arrows. In high fields, the four eigenstates become pure Zeeman states ($|1>=|\alpha^{\mu}\alpha^{e}>$, $|2>=|\beta^{\mu}\alpha^{e}>$, $|3>=|\beta^{\mu}\beta^{e}>$, $|4>=|\alpha^{\mu}\beta^{e}>$).

studied in higher magnetic fields. In this field region muon transitions (noted $\nu_{\mathrm{R}-}$ and $\nu_{\mathrm{R}+}$ in Figure 2.10) degenerate into two, which are independent of other magnetic nuclei that may be present. The A_{μ} may be determined from the time-domain TF-μSR spectrum or as is done in this work, from the spectrum in the frequency domain (Figure 2.11) using eq. 2.14:

$$\upsilon_{\mathrm{R}\pm} = |\frac{1}{2}A_{\mu} \pm \upsilon_{\mathrm{Mu}}| \ . \tag{2.14}$$

A_{μ} is obtained by summing the resonance frequencies belonging to the same radical in the frequency domain spectrum.

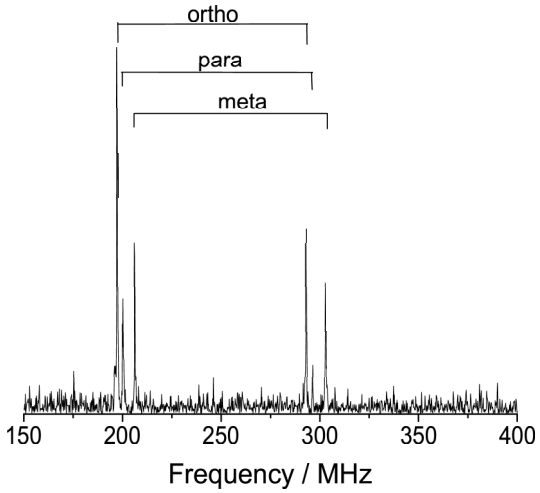

Figure 2.11: TF-μSR spectrum in the frequency domain of PPA-Mu radicals in neat PPA at $T = 322$ K in the field of 3000 G. Ortho, para and meta denote the corresponding PPA-Mu radicals. Peaks denote $\nu_{R_{+/-}}$ frequencies (ν_{R+} - right hand side of the figure; ν_{R-} - left hand side of the figure).

2.2.2 ^{2}H NMR-Spectroscopy

Nuclear Magnetic Resonance (NMR) is the spectroscopic technique used for studying chemical species, containing one or more nuclei with spin different from 0, I>0. The magnetic moment of the nucleus is associated with the presence of the spin and therefore the nucleus may interact with the magnetic field. Nuclei with spin I=1/2, exhibit a spherical distribution of the nuclear charge and the electric field in the environment does not influence the nuclear spin. However, when the nucleus exhibits spin I>1/2, an additional interaction between the nuclear electric quadrupole moment and the electric field gradient in the chemical bond at the position of the nucleus takes place.[51]

The ^{2}H NMR technique is a variant of the NMR that exploits the appearance of the pronounced electric quadrupole moment of deuterium–a heavy hydrogen isotope. The orientation of the magnetic moment in the external magnetic field is influenced by the orientation of the electric quadrupole moment in the electric field. In ^{2}H NMR spectroscopy all Hamiltonians are neglected except the Zeeman term and the quadrupolar term, as shown in eq. 2.15:

$$\hat{H} = \hat{H}_{\mathrm{Z}} + \hat{H}_{\mathrm{Q}} \,. \tag{2.15}$$

The Zeeman hamiltonian, $\hat{H}_{\mathrm{Z}}$, describes the interaction between the nuclear spin and the external magnetic field (γ - gyromagnetic ratio, $\hat{I}_{\mathrm{z}}$ - z-component of the nuclear

spin operator):[52,53]

$$\hat{H}_{\mathrm{Z}} = -\gamma\hbar B_0 \hat{I}_{\mathrm{z}} \ . \tag{2.16}$$

B_0 is defined to be oriented in the z-direction.[52,53]

The quadrupolar interaction Hamiltonian, $\hat{H}_{\mathrm{Q}}$, describes the interaction with the internal electric field gradients in the molecule.[54]

$$\hat{H}_{\mathrm{Q}} = \frac{e^2qQ}{4I(2I-1)}(3\hat{I_{\mathrm{z}}}^2 - \hat{\vec{I}}^2)\cdot\frac{1}{2}[(3\cos^2\theta - 1) + \eta\sin^2\theta\cos 2\phi] \ , \tag{2.17}$$

where Q is the scalar quadrupolar moment of the nucleus ($Q_{^2\mathrm{H}} = 2.875{\times}10^{-31}$ m^2) and η is the asymmetry parameter of the electric field gradient that characterizes the shape of the electric field gradient. θ is the angle that a particular carbon-deuterium bond vector makes with the direction of the external magnetic field B_0 and ϕ represents the equatorial angle. e^2qQ/h is defined as the quadrupolar coupling constant Q_{cc}. The asymmetry parameter, η, is defined by:

$$\eta = \frac{V_{\mathrm{xx}} - V_{\mathrm{yy}}}{V_{\mathrm{zz}}} \ , \tag{2.18}$$

where V_{xx}, V_{yy} and V_{zz} are the electric field gradient components in the x, y and z directions.

In the particular case of deuterated pyridinium cations, the interaction of the quadrupole electric moment is oriented along the axis of the C-^{2}H bond electric field gradient. In this work, the electric field gradient is assumed to be of cylindrical symmetry at the observed nucleus and the asymmetry parameter is therefore set to be 0.

The quadrupolar interaction is treated as the perturbation of the Zeeman interaction, as shown in Figure 2.12. The transition frequencies in the case of an I=1 nucleus with an axially symmetric electric field gradient (η=0) are given by:

$$\nu = \nu_0 \pm \frac{3}{8}\frac{e^2qQ}{h}(3cos^2\theta - 1) \ . \tag{2.19}$$

The theoretical ^{2}H NMR line shapes of deuterated benzene rotating about the C_6 axis in the rigid and fast rotational limit ($\langle\cos^2\theta\rangle$=1/2) are shown in Figure 2.13. The information of interest is extracted by simulating the line shape and relaxation of the experimentally obtained spectrum.[55] The ^{2}H NMR technique is particularly suitable for the investigation of dynamics in molecular solids.[51] Recently this has been applied to study inclusion compounds, liquid crystals, biological membranes, and polymers.[56–58]

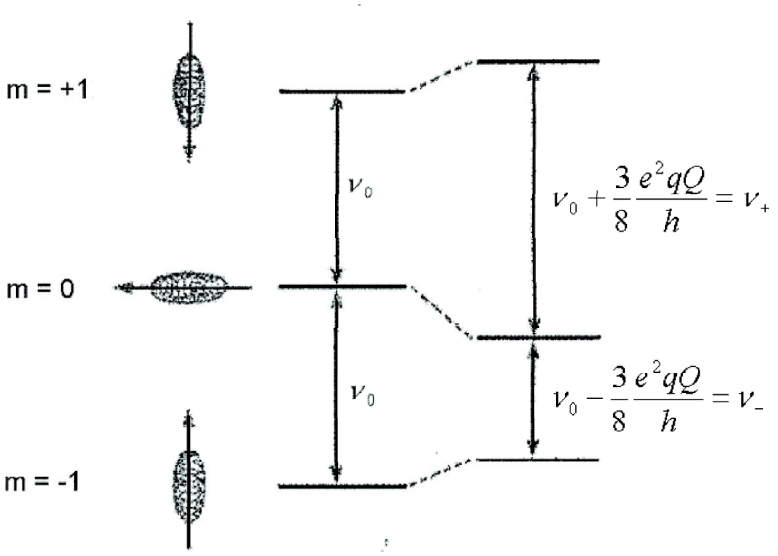

Figure 2.12: Energy diagram of the spin I=1 system.

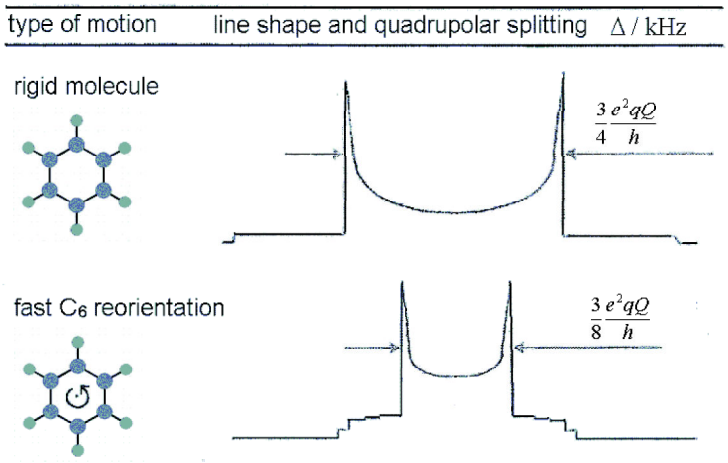

Figure 2.13: Fast (lower) and rigid limit (upper) spectra of the benzene molecule undergoing motion about the C_6 axis. Simulations of the line shapes were done using an appropriate FORTRAN program.[55]

2.2.3 Ab Initio calculations

The properties and structures of molecules may be calculated via force field based, semi-empirical, ab initio and density functional methods. Force field calculations determine the molecular energy in terms of force constants and other parameters. Semi-empirical methods use an incomplete Hamiltonian and parameters which are adjusted to fit experimental or ab initio data.

Ab initio methods (such as Hartree-Fock) aim to calculate the ground state molecular wave function, from which it is possible in principle to determine the energy and

all of the ground state properties of the molecule. They employ the correct Hamiltonian and do not use any experimental data, only the values of physical constants. The energy, E, may be found by

$$\hat{H}\Psi(x_1, x_2, ..., x_{\mathrm{N}}) = E\Psi(x_1, x_2, ..., x_{\mathrm{N}}) \ , \tag{2.20}$$

where $\hat{H}$ is the Hamiltonian and $x_{\mathrm{i}} = r_{\mathrm{i}}, \sigma_{\mathrm{i}}$ are the electronic space and spin coordinates, respectively. The main goal of most quantum molecular calculations is the determination of the molecular wave function Ψ which is an anti-symmetrized product (Slater determinant) of n electron functions ϕ_{i}, where each ϕ_{i} $(i = 1, ..., n)$ is a three-dimensional function which determines the properties of an individual electron in the molecule.[7]

Typically the LCAO (Linear Combination of Atomic Orbitals) approach is used. Here the individual molecular orbitals, ϕ_{i}, are constructed from a finite set of basis functions, which in this case are atomic orbitals, χ_{k}, as[59]

$$\phi_{\mathrm{i}} = \sum_{\mathrm{k}=1}^{N} c_{\mathrm{ik}}\chi_{\mathrm{k}} \ , \tag{2.21}$$

where i is an index labelling the particular molecular orbital. The atomic orbitals may be of hydrogen-like atoms (a Slater type basis set) but other choices such as Gaussians may also be employed. More precisely, a molecular orbital is composed of weighted atomic orbitals which collectively define the shape and spatial density of electrons in a molecular species.[60] Each of the χ_{k} is a function of the form $\chi_{\mathrm{k}} = Const. \times f(r) \times f(\theta, \phi)$ where k is the expansion index. Now the problem of finding the molecular wave function is reduced to finding the particular expansion coefficients, c_{ik}, in eq. 2.21. The set of atomic orbitals is called a basis set and must always be specified before the beginning of the calculation. Many different quantum-chemical methods have been developed in computational chemistry in order to solve the molecular Schrödinger equation associated with the molecular Hamiltonian. Typically ab initio methods are limited to small systems due to the large computational cost involved.

Therefore, the calculations presented in this thesis have been carried out with Density Functional Theory (DFT) methods which are often considered as a type of ab initio calculation. Here the aim is not to calculate the molecular wavefunction, but instead the molecular electron probability density (ρ(r)). ρ(r) is defined as the multiple integral over all spin coordinates and all but one spatial coordinates of the electrons[61]

as

$$\rho(\mathrm{r}_1) = N \int ... \int |\Psi(x_1, x_2, ..., x_\mathrm{N}|^2 \mathrm{d}s_1 \mathrm{d}x_2 ... \mathrm{d}x_\mathrm{N} \ . \tag{2.22}$$

The density, $\rho(\mathrm{r}_1)$, is the probability that any of the N electrons with arbitrary spin finds itself in the volume element r_1. The other $N-1$ electrons have arbitrary positions and the spin state as defined with the wave function Ψ. The number of variables of the electron density is not dependent on the number of electrons contrary to the wave function approach. Hohenberg and Kohn proved that the ground state electronic energy is fully characterized by the electron density.[62] Though it is proven that the ground state electron energy is determined by the electron density, the functional connecting these two variables is not exactly known. This is why some may not consider DFT a true ab initio technique.

DFT methods differ from each other according to the choice of the functional. The best functional for a particular calculation may be determined by comparing known experimental data for a set of similar systems with the results obtained in the experiment.

3 Experimental details and data analysis

3.1 Sample preparation

3.1.1 Samples for the muon spin resonance measurements

Alcohols, benzene, PEA, PPA, and octadecane of highest purity were purchased from Aldrich Chemicals and used without further purification. The triply distilled water used was prepared in our institute. Deuterated water used (99.5% D) was also purchased from Aldrich Chemicals and used without further purification, as well. Samples containing specifically deuterated PEA-d_5 (99.6% D) and PEA-1,1,2,2-d_4 (98.9% D) (as described in the Chapter 6), were bought from CDN Isotopes, Canada, and used without further purification, as well. Samples for the ALC-μSR experiments were prepared by mixing alcohols and water (in different volume ratios as given in the figures and tables in the text) with the probe molecules. The molar concentration of benzene was in all mixtures 20 mM, so that C_6H_7 did not interact with benzene molecules. The benzene concentration was always below the solubility limit for all of the solvents (23 mM in water at $T = 298$ K, where it is the lowest).

The concentrations of PEA and of PPA were 40 mM (only in water the concentration of PPA was 5 mM due to its small solubility). All components were bubbled with N_2 and mixed under oxygen free conditions. By using so small concentrations it was achieved to have an environment of the solute radical unaltered by the presence of other probe molecules. Samples for the TF-μSR experiments were prepared by means of a "freeze-pump-thaw" cycle, since these experiments are more sensitive to the presence of oxygen in the sample.

3.1.2 Samples for the ^{2}H NMR measuerements

Pyridine-d_5 (99 atom% D) and perchloric acid were purchased from Aldrich Chemicals and used without further purification. In preliminary experiments it was noticed that the content of water in the powder influences the inversion recovery spectra, particularly the obtained T_{1Z} and correlation times. This influence is not observed in the experimentally observed splittings in the inversion recovery and in the quadrupole echo spectra. Therefore, samples were prepared by crystallization from mixtures of the perdeuterated pyridine and perchloric acid in water for the quadrupole echo NMR and for the DSC measurements, and in 80% EtOH/20% H_2O solution for the inversion recovery NMR experiments.

3.2 Muon spin resonance

3.2.1 Avoided Level Crossing Muon Spin Resonance

Measurements were performed on the spectrometer at the πE3 port of the Swiss Muon Source, Villigen, Switzerland. The raw experimental data were corrected for the field dependent background by subtracting the spectrum of pure water (which contains no resonances) in the same field range. Afterwards the corrected data were fit with a single Lorentzian using the MINUIT function minimization library.[63]

3.2.2 Transverse Field Muon Spin Resonance

Measurements were performed on the spectrometer at the μE1 port of the Swiss Muon Source, Villigen, Switzerland. The raw experimental data were transformed from the time into the frequency domain and these data were fit using the MINUIT function minimization library.[63]

3.2.3 Muon Spin Resonance data processing and analysis

The ALC Δ_0 resonance field position only provides the difference between A_μ and A_p.[47] A_μ can be measured by TF-μSR, but this is limited to solutions with a benzene concentration of greater than 0.1 M, which is significantly larger than the solubility of benzene in some solvents used in this study. Similar limiting values are expected for PEA and PPA solutions. Both A_μ^met and $A_\mathrm{p}^\mathrm{met}$ have been measured in neat benzene and

Table 3.1: Methylene muon/proton hyperfine coupling constants ratios of PEA-Mu radicals in neat PEA.

	$A_\mu^{\mathrm{met}}/A_{\mathrm{p}}^{\mathrm{met}}$ (T=308 K)	$A_\mu^{\mathrm{met}}/A_{\mathrm{p}}^{\mathrm{met}}$ (T=348 K)
ortho	4.095	4.092
para	4.098	4.093
meta	4.084	4.077

in the gas phase. Yu et al. determined the ratio $S(\mathrm{C_6H_6Mu}) = A_\mu^{\mathrm{met}}/A_{\mathrm{p}}^{\mathrm{met}} = 4.060 \pm 0.001$ in neat benzene,[33] while Fleming et al. found that $S(\mathrm{C_6H_6Mu}) = A_\mu^{\mathrm{met}}/A_{\mathrm{p}}^{\mathrm{met}} = 4.063$ at 313 K and 4.058 at 353 K in the gas phase.[29] S is primarily due to the $\gamma_\mu/\gamma_{\mathrm{p}}$ ratio, which has a value of 3.183, with the remainder arising from the mass dependence of the internal dynamics. Since the vibrational modes of the $\mathrm{C_6H_7}$ and $\mathrm{C_6H_6Mu}$ isotopologues are analogous it was assumed that $S(\mathrm{C_6H_6Mu})$ is independent of solvent and temperature and the value measured by Yu et al. is used to calculate $A_{\mathrm{p}}^{\mathrm{met}}$ of $\mathrm{C_6H_6Mu}$ radical from the ALC Δ_0 resonance field position on the basis of

$$A_{\mathrm{p}}^{\mathrm{met}} = \frac{2B_{\mathrm{r}}}{(S-1)/(\gamma_\mu - \gamma_{\mathrm{p}}) - (S+1)/\gamma_{\mathrm{e}}} \,. \tag{3.1}$$

After substituting the values of S and the other constants eq. 3.1 can be simplified for the case of $A_{\mathrm{p}}^{\mathrm{met}}$ to give

$$A_{\mathrm{p}}^{\mathrm{met}} = \frac{B_{\mathrm{r}}}{163.76}\frac{\mathrm{MHz}}{\mathrm{G}} \,. \tag{3.2}$$

Eq. 3.2 is only valid for $A_{\mathrm{p}}^{\mathrm{met}}$ of $\mathrm{C_6H_6Mu}$ radical as S depends on the structure and the radical vibrational frequencies. Since $\mathrm{C_6H_6Mu}$ is quite a rigid radical,[29,33] this equation is assumed to remain valid in the temperature range studied here.

For PEA-Mu radicals the S ratio is expected to be somewhat temperature dependent because of the non-rigid substituent hydroxyalkyl group. In particular, PEA-Mu radicals are in a dynamical balance between folded and non-folded conformation (defined in section 6.1, Figure 6.1) due to the intramolecular hydrogen bonding interaction. With increased temperature, the balance shifts towards the non-folded conformation and that in return influences S(PEA-Mu).

$A_{\mathrm{p}}^{\mathrm{met}}$ and A_μ^{met} of PEA-Mu radicals in neat PEA were previously reported by Scheuermann et al.[19] S(PEA-Mu)= $A_\mu^{\mathrm{met}}/A_{\mathrm{p}}^{\mathrm{met}}$ ratios were obtained from these measurements and listed in Table 3.1. After introducing these values and other constants

Table 3.2: A and B parameters from the McConnell relation for β-methyl protons of ortho and para PEA-Mu and PPA-Mu radicals.

A, B (ortho) / MHz	1.5 ± 2.2, 92 ± 8
A, B (para) / MHz	-6.7 ± 5.4, 137 ± 18

into eq. 3.1 the following eqs. have been obtained for PEA-Mu radicals:

a) at $T = 308$ K

$$A_{\mathrm{p}}^{\mathrm{met}}(\text{ortho PEA-Mu}) = \frac{B_{\mathrm{r}}}{165.64}\frac{\mathrm{MHz}}{\mathrm{G}} \ , \tag{3.3}$$

$$A_{\mathrm{p}}^{\mathrm{met}}(\text{para PEA-Mu}) = \frac{B_{\mathrm{r}}}{165.78}\frac{\mathrm{MHz}}{\mathrm{G}} \ , \tag{3.4}$$

$$A_{\mathrm{p}}^{\mathrm{met}}(\text{meta PEA-Mu}) = \frac{B_{\mathrm{r}}}{165.02}\frac{\mathrm{MHz}}{\mathrm{G}} \ , \tag{3.5}$$

b) at $T = 348$ K

$$A_{\mathrm{p}}^{\mathrm{met}}(\text{ortho PEA-Mu}) = \frac{B_{\mathrm{r}}}{165.47}\frac{\mathrm{MHz}}{\mathrm{G}} \ , \tag{3.6}$$

$$A_{\mathrm{p}}^{\mathrm{met}}(\text{para PEA-Mu}) = \frac{B_{\mathrm{r}}}{165.51}\frac{\mathrm{MHz}}{\mathrm{G}} \ , \tag{3.7}$$

$$A_{\mathrm{p}}^{\mathrm{met}}(\text{meta PEA-Mu}) = \frac{B_{\mathrm{r}}}{165.64}\frac{\mathrm{MHz}}{\mathrm{G}} \ , \tag{3.8}$$

where $A_{\mathrm{p}}^{\mathrm{met}}$ values are given in MHz and B_{r} in G. For PPA-Mu radicals, additional TF- and ALC-μSR experiments were performed and these results are presented in section 5.2. Hfc values of other in-plane and of β-methylene protons are determined by introducing the A_{μ}^{met} value into the equation for the Δ_0 ALC resonance (eq. 2.10).

In order to analyse β-methylene protons dynamics (Chapter 6) it is necessary to know the parameters A and B in the McConnell relation for the β-methyl protons (eq. 2.6). It is reasonable to assume that these parameters are the same for both PEA-Mu and PPA-Mu radicals since they belong to the same class of radicals. They are determined by fitting the dihedral angles and β-methylene hfcs obtained from ab initio calculations to the McConnell relation for β-methyl protons (eq. 2.6) and afterwards averaging the obtained A and B values. The obtained A and B values are listed in the Table 3.2.

3.3 NMR

3.3.1 Experimental

^{2}H NMR experiments were performed at the frequency of 46.07 MHz on a Bruker CXP 300 spectrometer interfaced to a Tecmag spectrometer control system. ^{2}H NMR spectra were recorded with the quadrupole echo sequence $((\pi/2)_{\mathrm{x}} - \tau_1 - (\pi/2)_{\mathrm{y}} - \tau_2)$ with $\pi/2$ pulses of 2.2 μs and a pulse spacing of $\tau_1 = \tau_2 = 20$ μs. Nonuniform excitation observed in spectra whose width, $\Delta\omega$, is comparable to the pulse frequency, ω_1, sometimes requires the use of composite pulses. In particular, the composite pulses can be very useful in ^{2}H NMR of solids, where the quadrupolar coupling constant is typically of the order of 180 kHz and $\omega_1/2\pi$ no greater than 125 kHz, corresponding to a $\pi/2$ pulse of 2.0 μs.[64] For this reason the composite pulse instead of the ordinary inversion recovery sequence was used. A modified inversion recovery sequence $((\pi/2)_\phi(\pi/2)_{\phi\pm\pi/2}(\pi/2)_\phi - \tau_{\mathrm{r}} - (\pi/2)_{\mathrm{x}} - \tau_1 - (\pi/2)_{\mathrm{y}} - \tau_2$ with $(\phi = 0, \pi/2, \pi, 3\pi/2))$ was applied to determine the spin-lattice relaxation times ($T_{1\mathrm{Z}}$) and to record the corresponding partially relaxed spectra.[64] The recycle delay between successive scans was at least 10 times the spin-lattice relaxation time $T_{1\mathrm{Z}}$. The number of scans was 16 or 32. The temperature of the sample was controlled with a Bruker BVT 1000 control unit, and in general it was stable to within 1 K. Measurements were done starting from room temperature and cooling in increments. After finishing the measurements at lower temperatures, the room temperature measurement was repeated to check the reproducibility. Before each measurement the sample was allowed to thermally equilibrate for 20-30 minutes.

3.3.2 NMR data processing, simulations and analysis

Quantitative analysis of quadrupole echo and inversion recovery experiments provides detailed insight into the pyridinium cation dynamics as a function of temperature. The in-plane six-site jump model described by Beck et al. in the study of pyridinium tetrafluoroborate ($PyBF_4$) was used in this work.[65,66] Based on the symmetry of the pyridinium cation and in agreement with earlier work,[65] a six-site jump model appears as a realistic approximation for the cation reorientational motion. The potential (Figure 3.1) used for the six-site jump model is a superposition of a six-fold potential due to the approximate cation symmetry (V_6^0) and a one-fold potential due to the ferroelectric field and is given by:

$$V = V_1^0 \sin(\Psi - \pi/2) + V_6^0 \sin(6\Psi - \pi/2)\ . \tag{3.9}$$

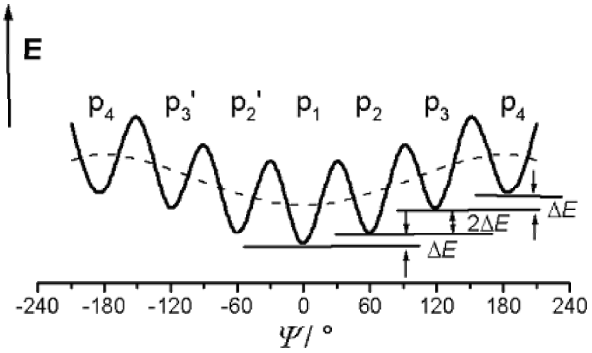

Figure 3.1: Used potential and corresponding angles with respect to the ferroelectric axis.[65]

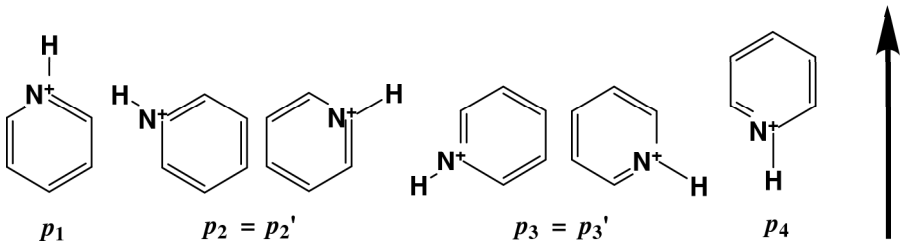

Figure 3.2: Orientations of the pyridinium cation and the corresponding populations with respect to the ferroelectric axis (indicated by the arrow).

Enthalpies obtained from DSC measurements are compared with the data obtained from the NMR data analysis. The latter are calculated from the populations derived from simulations of the quadrupole echo NMR experiments. Orientations with respect to the ferroelectric axis and corresponding populations are defined in Figure 3.2. For each fraction of molecules that changes orientation during incremental heating it is possible to calculate the enthalpy increment employing a formula that relates to the van´t Hoff eq.[65]

$$\Delta H_{\mathrm{n}} = -fR\frac{\Delta(\ln K)}{\Delta(1/T)} \ , \tag{3.10}$$

where ΔH_{n} is the fractional enthalpy change between two successive temperature points, f represents a fraction of molecules that change orientation, and K are individual equilibrium constants for each jump reorientation.

The macroscopic polarization in the model of Beck et al.[65,66] is calculated from the populations using eq. 3.11:

$$pol_{\mathrm{NMR}} = -\frac{Z\mu(p_1 + p_2 - p_3 - p_4)}{V_{\mathrm{cell}}(T)} \ , \tag{3.11}$$

where μ is the dipole moment of the pyridinium cation, Z is the number of cations in the unit cell and $V_{\mathrm{cell}}(T)$ is the unit cell volume which depends slightly on temperature.[67] The pyroeffect measurements proved difficult due to the hygroscopic nature and experimental imperfections in the preparation of the $PyClO_4$ single crystal and in the pyroeffect measurements.[67,68] To circumvent the experimental uncertainties, we introduce the unit "% relative polarization". This is the fractional shift of the macroscopic polarization (NMR-derived and experimentally measured) between its lowest value (0% in the high-temperature phase) and its highest value (100% at the lowest temperature measured). In this way, we compare NMR-derived and experimentally measured macroscopic polarizations and avoid the uncertainty in the exact value of the dipole moment used for the translation of the NMR-derived populations into ferroelectric polarizations.[65,69]

Assuming that the difference between the measured pyroeffect and NMR derived polarizations is due to an anion-cation sublattices displacement it is possible to calculate the relative displacement x from

$$x = \frac{(pol_{\mathrm{NMR}} - pol_{\mathrm{pyro}})V_{\mathrm{cell}}}{q} \frac{1}{3.336 \times 10^{-30}\ \mathrm{Cm}}\ , \tag{3.12}$$

where pol_{NMR} and pol_{pyro} are macroscopic polarizations derived from NMR and pyroeffect data, and q is the unit electric charge.[65] To calculate the sublattice displacement, the NMR derived results were normalized to the absolute value of the highest and of the lowest experimentally measured macroscopic polarization and then used in the calculation.

The simulations of the quadrupole echo spectra were performed on the basis of the six-site jump model in the fast exchange limit and matched with experimental spectra by variation of the p_1 value. The populations p_2, p_3 and p_4 are related to p_1 by the one-fold potential V_1^0. Experimental spin-lattice relaxation times T_{1Z} were determined by analysis of the amplitudes of the experimental free induction decay (FID) from the inversion recovery experiments. Data processing was done on a SUN workstation and a personal computer using the NMR1 and Sybyl/Triad software packages (Tripos, St. Louis, MO). Simulations were done using an appropriate FORTRAN program[55] that describes the theoretical behaviour of an $I = 1$ spin system during quadrupole echo and inversion recovery experiments, under the assumption that no other motion of the ring except rotation about the pseudo C_6 axis takes place. The simulations of experimental data from inversion recovery experiments were done on the basis of the 6-site jump model by varying the motional correlation time t_c, and by using the other parameters (populations p_1, etc.) deduced from the analysis of ^2H NMR quadrupole echo spectra.

Table 3.3: Simulation paramters used in the ^{2}H NMR data analysis. [a]Asymmetry parameter η=0, [b]Euler angles ϕ, θ, Ψ relating the magnetic principal axis system and the molecular axis system (z-axis parallel to motional axis).

Parameter	Value
Quadrupolar coupling constant[a] (e^2qQ/h)	179 kHz
Transformation angles[b]	
ϕ	0°
θ	90°
Ψ	0°, ±60°, ±120°, ±180°
Residual line width ($1/\pi T_2$)	from 2.542 kHz to 3.142 kHz

The constant parameters used during the present data analysis are summarized in Table 3.3. The quadrupolar coupling constant and residual line width parameters were obtained from simulations of ^{2}H NMR quadrupole echo spectra.

3.4 Ab Initio calculations

Ab initio calculations in the studies of C_6H_7, PEA-H and PPA-H radicals (instead of PEA-Mu and PPA-Mu) were performed using the Gaussian 98 software package.[70] The implemented unrestricted B3LYP method was used with the 6-311++G** basis sets, as this combination has been demonstrated to predict hfcs that are in close agreement with experimental values.[71] Calculations for C_6H_7 (Chapter 4) were also performed with other basis sets to determine whether this influences the results, but no qualitative changes were observed, so only the results with 6-311++G** basis set are reported. In order to mimic the polarity range of different solvents and mixtures in this work, the magnitude of the electric field introduced in the ab initio calculations was varied, until the experimentally measured difference in $A_{\mathrm{p}}^{\mathrm{met}}$ between octadecane and water was reproduced (see the Chapter 4). The Mu atom was always treated as H atom.

In the studies of ferro- and nonferroelectric pyridinium salts (Chapter 8) calculations were performed for the anions in vacuum, using the Gaussian 03 software package.[72] The implemented B3LYP functional and a 6-311++G** basis set were used for B, F, P, Cl, O and S atoms again, and the LANL2DZ basis set for Cr. For I and Re atoms the LANL2DZ ECP basis sets and potentials were used as described in other studies.[73,74] Polarizabilities were calculated on the basis of previously optimised

structures.

3.5 DSC measurements

A differential scanning calorimeter Netzsch DSC-204 was used to perform measurements on Py-d_5-ClO_4 from 215 K up to 290 K with a heating rate of 5 K min^{-1}.

4 Solvent effects on the cyclohexadienyl radical

4.1 General remarks

The dipole-dipole reaction field model of RK developed to account for the solvent dependence of the ^{14}N hfc (A_{N}) in DTBN (Figure 4.1) serves as the basis of the present work.[17] Using a modified Hückel molecular orbital treatment RK demonstrated, that the A_{N} depends linearly on the difference of the electrostatic potential (ΔU) between the oxygen and the nitrogen atoms,

$$A_{\mathrm{N}} = A_{\mathrm{N}}^{0} + C r_{\mathrm{NO}} \Delta U \ , \tag{4.1}$$

where C is a constant typical for the given radical and r_{NO} is the distance between the nitrogen and oxygen atoms. The bulky tert-butyl substituents of DTBN protect the NO group from all sides except one, and the reaction field is dominated by a single solvent molecule on the axis of the NO bond. RK calculated the additional electric field at the center of the NO group that is due to the dipole moment of the nearest solvent molecule and concluded that the A_{N} depends linearly on the product of concentration of the solvent dipole moments and their magnitude, abbreviated as $[\mu_{\mathrm{S}}]$,

$$A_{\mathrm{N}} = A + B\mu_{\mathrm{S}} \frac{\rho_{\mathrm{S}}}{M_{\mathrm{S}}} = A + B[\mu_{\mathrm{S}}] \ , \tag{4.2}$$

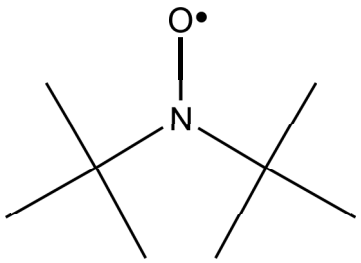

Figure 4.1: Di-tert-butyl-nitroxide radical.

where A and B are empirical constants that depend on the type of radical, μ_S the dipole moment of the solvent molecule and ρ_S and M_S are the density and the molecular weight of the solvent, respectively.

The $[\mu_S] = \mu_S\rho_S/M_S$ values for the mixtures depend on the volume fractions of the constituents in the following manner:

$$[\mu_S] = \frac{[\mu_S^{(1)}]V_1 + [\mu_S^{(2)}]V_2}{V_1 + V_2} \ , \tag{4.3}$$

where V_1 and V_2 are the volumes of solvents in the mixtures and $[\mu_1]$ and $[\mu_2]$ are the corresponding dipole moment concentrations multiplied with the corresponding dipole value of the pure solvents. The $[\mu_S]$ values of the solvents and the mixtures studied here are reported in tables and figures throughout this chapter. The overall dipole moment of aliphatic alcohols is very dependent on their conformation, and this may vary in various mixtures and liquids. In order to overcome this uncertainty the OH group dipole moment value in the analysis will be used, since the dipole moment of the alcohols in this study is mainly located on the OH group. Its gas phase value is μ_{OH}=1.78 D,[75] and this is the value that is used in the analysis. In order to be consistent, the gas phase value for water is used as well (μ_{H_2O}=1.855 D).[76]

RK suggested that their model could be valid for other radicals, but that the constants in the derived equations would be different for each particular radical.[17]

An objective in this chapter is to further develop the dipole-dipole reaction field model of RK and to apply it to describe the solute-solvent interactions for the C_6H_7 radical.[17] First the DTBN and C_6H_7 were compared to see what the differences and similarities are between them. Afterwards, the significance of the hydrogen bonding in the case of C_6H_7 is discussed.

One of the main points of the dipole-dipole reaction field theory of RK is that the ^{14}N hfc is directly proportional to the potential difference along the NO group electric dipole moment axis. For symmetry reasons there are no other components which could play a role. The RK model assumes that the primary dipole moment of the radical induces some degree of preferential alignment in the orientation of the surrounding solvent dipoles, which then produce an electric field that alters the hfcs. In order to test to what extent this affects the hfcs of the C_6H_7 radical ab initio calculations were performed with different applied electric fields along the C_6H_7 dipole moment axis, as shown in Figure 4.2. It is expected that the electric field influences the structure, which in turn alters the hfcs. In order to distinguish the contribution of the geometric differences in environments of different polarity, two series of ab initio calculations were

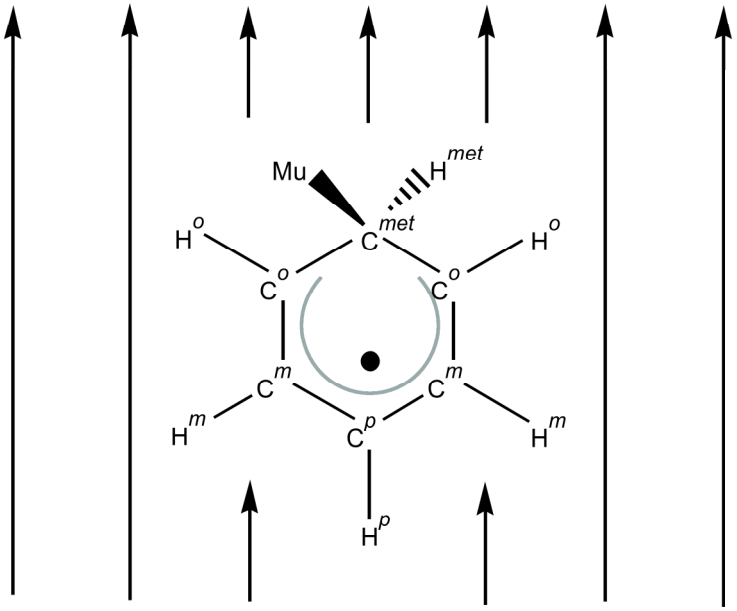

Figure 4.2: Cyclohexadienyl radical in an electric field with a direction shown by the arrows. One methylene proton, H^{met}, is replaced by the lightest hydrogen isotope atom muonium (Mu).

performed. In one series, the structure of C_6H_7 was optimised in the applied electric field. In the second series, the optimised structures for the given values of the electric field were used, but with the electric field turned off and A_p^{met} obtained in the two series were compared. One major shortcoming of the dipole-dipole reaction field model is that it is valid only for dipolar liquids and cannot account for the variation of the hfc in non-dipolar solvents like benzene and octadecane.

The major difference between these two non-dipolar solvents is that benzene has a large molecular electric quadrupole moment while octadecane does not. The effect of solvent quadrupole moment on the hfcs of the C_6H_7 was investigated, and a dipole-dipole reaction field model of RK was extended to include *dipole-quadrupole* interactions. The corresponding equations will be coupled with the predictions of ab initio calculations and the results will be compared with the experiment.

It has been suggested that the temperature coefficient of the ^{14}N hfc of DTBN depends only on the variation of the solvent density with temperature.[77] One of the intentions in this chapter is to distinguish the factors that influence the A_p^{met} temperature behaviour of the C_6H_7, by comparing the temperature dependence of the A_p^{met} in the gas phase and the temperature dependence of the solvent density with the temperature dependence of the A_p^{met} in the solvent.

Table 4.1: Numerically extrapolated Δ_0 ALC resonance field positions of cyclohexadienyl radical methylene proton at 308 K and at 348 K in various solvents and mixtures. Abbreviations as in List of abbreviations and symbols.

solvent	$[\mu_S]$ / D mol dm^{-3}	B_r / G ($T = 308$ K)	B_r / G ($T = 348$ K)	$\Delta B_r/\Delta T$ / G K^{-1}	$\Delta A_p^{met}/\Delta T$ / MHz K^{-1}
Octadecane	0	20635	20507	-3.15	-0.0192
1/2 EtOH / 1/2 Octanol	21.0	20704	20577	-3.17(4)	-0.0193(2)
EtOH	30.6	20725	20591	-3.25(4)	-0.0199(3)
MeOH	44.0	20750	20615	-3.30(1)	-0.0202(7)
1/3 H_2O / 2/3 MeOH	63.7	20815	20686	-3.16(7)	-0.0193(4)
2/3 H_2O / 1/3 MeOH	83.4	20880	20749	-3.20(7)	-0.0195(4)
H_2O	103.1	20931	20807	-3.00(7)	-0.0183(4)
Benzene	0	20716	20569	-3.60(7)	-0.0219(5)

4.2 Results

4.2.1 Muon spin resonance experiments

Δ_0 ALC-μSR resonance peak positions of C_6H_7 methylene protons are listed in Table 4.1 and corresponding A_p^{met} were extracted using eq. 3.2.

Their accuracy depends mainly on the validity of the approximation that $S = (A_\mu/A_p)^{met}$ remains the same in all solvents and mixtures. The methylene proton Δ_0 ALC-μSR resonance in water is shown for three temperatures in Figure 4.3. The resonance field decreases linearly with increasing temperature, and the same behaviour was observed in all of the other solvents and mixtures studied here, but the slopes are somewhat different, as seen in Table 4.1. The resonance fields were linearly extrapolated to 308 K and 348 K and afterwards used in the calculation of the hfcs. At constant temperature the ALC Δ_0 resonance shifts towards lower magnetic fields with decreasing solvent polarity. Selected ALC-μSR spectra in different solvents are displayed in Figure 4.4 and the shift of the resonance field is linearly dependent on the $[\mu_S]$ value as presented in Table 4.1. In the water, neat alcohols and in the mixtures, A_p^{met} depends linearly on $[\mu_S]$, as shown in Figure 4.5. It is given by:

$$A_p^{met}(T = 308\ \text{K}) = 126.01(3)\ \text{MHz} + 0.0176(5)\frac{\text{MHz} \cdot \text{dm}^3}{\text{D} \cdot \text{mol}}[\mu_S]\ , \qquad (4.4)$$

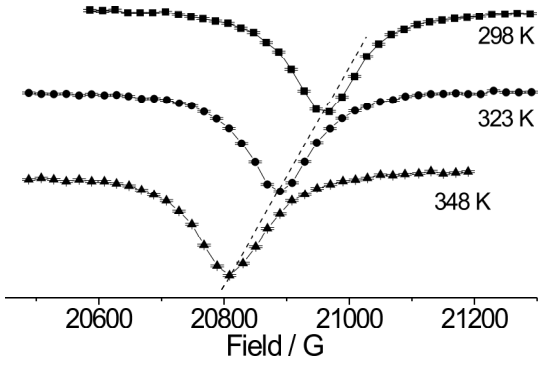

Figure 4.3: Temperature dependence of the cyclohexadienyl radical methylene proton Δ_0 ALC resonance in the water.

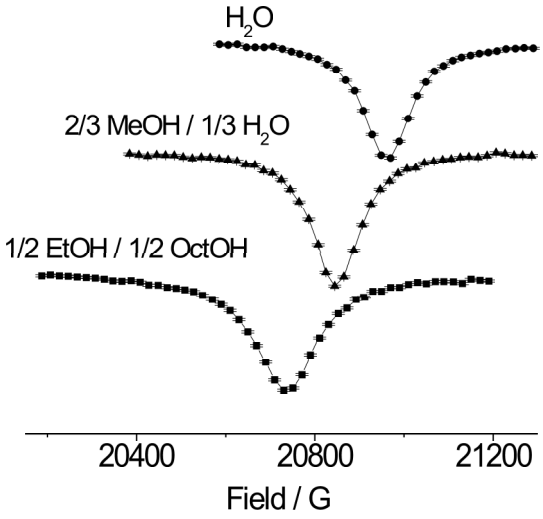

Figure 4.4: Selected ALC-μSR spectra of methylene proton Δ_0 resonances at 298 K. Abbreviations as in List of abbreviations and symbols.

$$A_{\mathrm{p}}^{\mathrm{met}}(T = 348\ \mathrm{K}) = 125.22(4)\ \mathrm{MHz} + 0.0176(7)\frac{\mathrm{MHz}\cdot\mathrm{dm}^3}{\mathrm{D}\cdot\mathrm{mol}}[\mu_{\mathrm{S}}]\ , \qquad (4.5)$$

where the units of $[\mu_{\mathrm{S}}]$ are Debye mol dm^{-3}. The R factors representing the quality of fit were 0.998 and 0.996, respectively, which clearly confirms that hfcs depend linearly on $[\mu_{\mathrm{S}}]$ in water and alcohols in this study. The intercepts with the ordinate and the slopes of eqs. 4.4 and 4.5 correspond to the factors A and B of the RK theory (eq. 4.2). It should be noted that B in this case is very sensitive to the values of the used dipole moments.

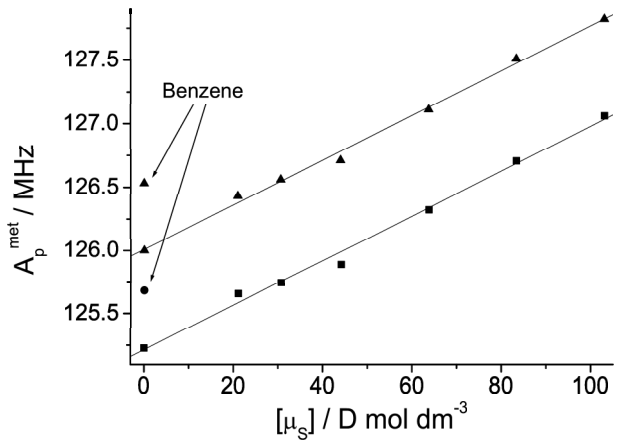

Figure 4.5: The cyclohexadienyl radical methylene proton hyperfine coupling constants as a function of the [μ_S] value at 308 K (▲) and 348 K (■). The experimental points are for the entries in Table 4.1.

A_p^{met} of the C_6H_7 radical in benzene does not match the trend observed for the other solvents and mixtures, since A_p^{met} is almost the same as for EtOH, even though benzene has the same [μ_S] value as octadecane.

A_μ^{met} hfcs can be obtained by multiplication of the A_p^{met} values with the S (C_6H_7) ratio measured by Yu et al.[33] as described in Section 3.2.3.

4.2.2 Ab Initio calculations

A_p^{met} depends linearly on the potential difference between the methylene and para carbon atoms with a slope C' of 3.94 MHz V^{-1} (Figure 4.6). Absolute values of the hfcs obtained with the 6-311++G** basis set are closer to the experimentally observed values than those obtained using EPR-II, but in both cases A_p^{met} depends linearly on the potential difference, and the slopes are approximately the same. The following discussion is based on calculations using 6-311++G**.

The structure of the C_6H_7 radical depends on the strength of the external electric field. This structure was optimised in various applied electric fields. Then the field was set to zero and A_p^{met} was calculated for these field-optimised structures. In this case the slope of potential difference versus external field was ca. 6.6 times smaller than when optimisation and hfc calculations were performed in the same electric field. This demonstrates that the effect of the electric field on the hfcs is much larger than the effect of the structural change induced by the applied field.

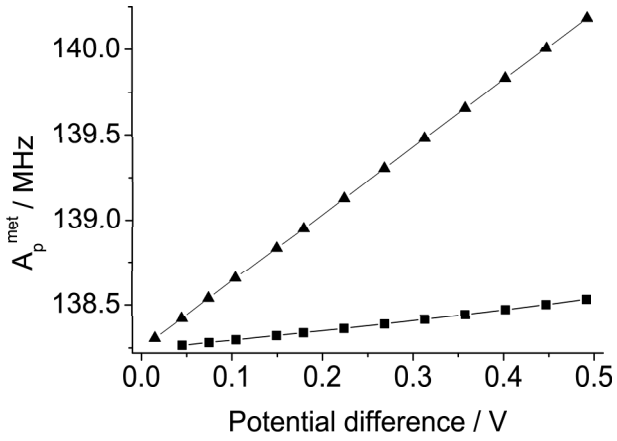

Figure 4.6: Dependence of the methylene proton hyperfine coupling constant on the potential difference $\Delta U_{\mathrm{C^{met}\_C^p}}$ between the methylene and para carbon atoms according to eq. 4.10: (▲) in an electric field, $C' = 3.94$ MHz V^{-1} (structure allowed to optimise), (■) electric field off (with structure optimized in field), $C' = 0.59$ MHz V^{-1}.

The charge distribution, structure, and dipole moment of the C_6H_7 radical are perturbed by an applied electric field. The ab initio calculations with an applied electric field show that the dipole moments and A_p^{met} of C_6H_7 depend linearly on the electric field. The dependence of the A_p^{met} on the C_6H_7 dipole moment, $\mu_{C_6H_7}$ (in Debye), is given by

$$A_p^{met} = 136.8 \text{ MHz} + 2.69405 \frac{\text{MHz}}{\text{D}} \mu_{C_6H_7}. \tag{4.6}$$

In the range of electric fields introduced in these calculations the C_6H_7 dipole moment changes from 0.54 D (applied electric field 0 V m^{-1}) to 1.26 D (applied dipole electric field 1.7×10^{-9} V m^{-1} which is the necessary field to reproduce the full experimental A_p^{met} solvent shift). In the following text the electric potential difference between the methylene and para carbon atoms will be quoted, which is related to the electric field via $\Delta U_{\mathrm{C^{met}\_C^p}} = C \cdot d_{\mathrm{C^{met}\_C^p}}$, where $d_{\mathrm{C^{met}\_C^p}} \approx 2.9 \times 10^{-10}$ m is the distance between the two carbon atoms.

In order to check the reliability of the ab initio calculations, the polarizability volume, α', of C_6H_7 along the axis of the dipole moment is calculated from the dependence of the C_6H_7 dipole moment on the electric field. It is determined to be $\alpha'(C_6H_7)_{\text{ab initio}}$ $= 1.27\times10^{-29}$ m^3, which is close to the experimentally measured isotropic polarizability of benzene, $\alpha'(C_6H_6)_{\text{exp}} = 1.03\times10^{-29}$ m^3. For comparison using the same approach in these ab initio calculations, the polarizability of benzene is calculated and it is found

to be $\alpha'(C_6H_6)_{\text{ab initio}} = 1.17\times10^{-29}$ m^3. These similar values for the polarizability volumes allow the conclusion that the results obtained from ab initio calculations can be considered reliable.

4.3 Discussion

Comparing the experimental data for A_p^{met} to the results of the *ab initio* calculations (Figures 4.5 and 4.6) reveals that the calculated values are too high by ca. 9%. There are several reasons for this: (i) Hfcs represent the difference between the populations of electron spin α and β at the nucleus, a difference between two large numbers which has always been difficult to evaluate, in particular as the basis sets are better representations of the tails of the atomic wave functions than of the cusps at the nuclei. (ii) Due to its delocalised nature and the importance of spin polarization, quantum chemical calculations of the hfcs of C_6H_7 radical proved to be particularly difficult, and the predicted values for the methylene protons fluctuated by more than a factor 3 between different methods.[78] (iii) Calculations relate to rigid equilibrium geometry and a temperature of 0 K. While vibrational averaging and thermal population of vibrationally excited states is in principle possible, it is computationally demanding for the 33 internal degrees of freedom of C_6H_7, and it leads to contributions of both positive and negative sign. In the present case the negative temperature dependence of the experimental A_p^{met} increases the discrepancy. Since the aim of the present study is an interpretation of changes on solvation rather than of absolute values of A_p^{met} the mismatch of absolute values does not present a real problem.

In the continuum model the hfcs only depend on the dielectric constants of the solvent,[15] so A_p^{met} in benzene and octadecane, which have similar dielectric constants are expected to be approximately the same. This is not the case, as A_p^{met} is 0.45 MHz larger in benzene than in octadecane but similar to the value in the polar EtOH, as seen in Figure 4.5. Abe et al.[79] proposed that the reaction field of the induced dipole moment on the solvent molecule influences the radicals' hfcs so that it increases with increasing *polarizability*. This hypothesis seems reasonable and will be further considered here, but it is also proposed that there are further solvent properties that are not included in the RK model but can alter the hfcs of a radical.

4.3.1 Comparison between the di-tert-butyl-nitroxide and the cyclohexadienyl radical

There are several differences between the DTBN and C_6H_7 radical that have to be considered. The charges responsible for C_6H_7 dipole moment are spread over the whole molecule, while in the DTBN they are mostly localized on the NO group. Solvent molecules may approach C_6H_7 more closely than to DTBN which is protected by the bulky tert-butyl groups. Nevertheless, DTBN can form strong hydrogen bonds along the axis of the NO group.

4.3.2 Hydrogen bonding

Hydrogen bonding with the π-electron system is of great importance in both chemical and biological recognition.[80,81] In the course of hydrogen bonding interaction between the benzene and water molecules, water molecules approach benzene from both sides of the aromatic ring.[81] Fluctuations of the hydrogen bonds[82] occur on a time scale of $\sim 10^{-12}$ s whereas the timescale of the μSR experiment is on the order of 10^{-6} s, given by the muon lifetime. This means that experiments with C_6H_7 (in this case represented by C_6H_6Mu) monitor a time average which sees hydrogen bonding with equal probability on both sides of the ring plane. The components of the water dipole moment vector perpendicular to the C_6H_7 plane therefore cancel each other out, whereas the component parallel to the C_6H_7 long axis does not, due to symmetry reasons. A recent theoretical study of C_6H_7-H_2O_n (n=1,2) clusters in gas phase and in continuum has shown an increase of the mean A_p^{met} for certain geometries, which is in qualitative agreement with these experiments.[46]

With respect to the RK theory,[17] hydrogen bonding affects the hfcs of C_6H_7 if it produces a net electric field along the C_6H_7 dipole moment axis. Therefore, the orientation of the second oxygen-hydrogen bond of H_2O, i.e. the one that is not hydrogen bonded to the C_6H_7 ring, is relevant. Straka et al.[46] also reported small changes in bond lengths between the methylene carbon and hydrogen atoms, which also affects A_p^{met}. Furthermore, the dynamics of the system plays a paramount role.

Hydrogen bonding of the C_6H_7 radical is of significant importance in situations where it does not occur symmetrically with respect to the C_6H_7 ring plane, for example when the radical resides on a hydroxylated silica gel surface.[83,84] In this case, the electric field due to the surface OH groups is to a first approximation perpendicular to the C_6H_7 radical ring plane. Therefore, the methylene protons are no longer equivalent,

and it is expected that methylene bond lengths and angles differ from those in the gas and in the liquid phase. Experimentally, in a monolayer of benzene an increase of A_μ^{met} of C_6H_6Mu amounting to 0.4% (0.5 MHz relative to neat benzene) is observed.[84] This corresponds to about one-third of the difference between neat benzene and bulk water.

4.3.3 The dipole-dipole reaction field model

The benzene molecule is centrosymmetric, whereas C_6H_7 has a dipole moment between the 0.54 D (in vacuum, no electric field) and 1.26 D (at 1.7×10^{-9} V m^{-1}, the highest electric field in this work). C_6H_7 is thus a moderately polar molecule and can polarize its environment via the dipole-ion, dipole-dipole, dipole-induced dipole and dipole-quadrupole interactions. Water has a pK_{a} value of 14, which means that the concentration of dissociated molecules is 10^{-7} M. The fraction of dissociated molecules in alcohols is even smaller. Therefore, dipole-ion interactions will not be taken into account. C_6H_6 and C_6H_7 are of similar shape. The mean distance in the first solvent shell of neat benzene, 5.6×10^{-10} m, is chosen as an approximate distance between the dipole moments of the C_6H_7 radical and of the solvents.[85] The dipole-dipole electrostatic interaction ($E_{\mathrm{d-d}} \sim 1/r^3$) of the two dipole moments ($\mu_{C_6H_7} = 1.26$ D and $\mu_{H_2O} = 1.855$ D) varies between the $E_{\mathrm{d-d}} = 0$ and $E_{\mathrm{d-d}} = 1.6$ kJ mol^{-1} depending on the relative orientation. This is significant compared to the thermal energy in the range of temperatures in the present study ($RT = 2.56$ kJ mol^{-1} at 308 K and $RT = 2.89$ kJ mol^{-1} at 348 K).

The dipole-induced dipole interaction energy ($E_{\mathrm{d-id}} \sim 1/r^6$) is several orders of magnitude smaller than $E_{\mathrm{d-d}}$ for the C_6H_7 radical in water ($E_{\mathrm{d-id}} \approx 0.01$ kJ mol^{-1} at $r = 5.6 \times 10^{-10}$ m) and is therefore negligible. In alcohols this interaction may be larger since the alkyl part of the solvent molecules becomes bigger (polarizability increased), but it remains insignificant compared to the dipole-dipole interaction. The dipole-quadrupole interaction ($E_{\mathrm{d-q}} \sim 1/r^4$) is of importance in solvents of significant quadrupole moments, as discussed further in section 4.3.4. The dipole moment of the C_6H_7 radical will induce an alignment of neighbouring solvent dipoles, and thermal energy works against this alignment. The liquid system represents a dynamical equilibrium on the time scale of the μSR experiment ($\approx 10^{-6}$ s). The interaction between C_6H_7 and water or the alcohols is comparable to thermal energy at room temperature, so the neighbouring solvent molecules do exhibit preferred but incomplete orientations, which results in a net electric field along the direction of the dipole moment of C_6H_7.

The effect of the solvent molecules´ dipole moments arranged in selected geome-

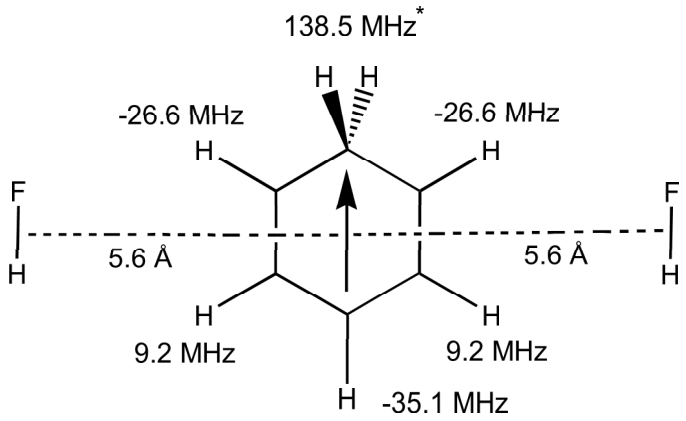

Figure 4.7: Results of ab initio calculations when the dipole moments are placed either side and antiparallel with respect to the dipole moment of the cyclohexadienyl radical. The hfcs are written next to the corresponding atoms for the given configuration. The arrow represents the dipole moment direction of the cyclohexadienyl radical. *gas phase (field=0): $A_{\mathrm{p}}^{\mathrm{met}} = 138.2$ MHz (structures of the molecules in the figure were previously optimized in the gas phase).

tries (as in Figures 4.7 and 4.8) is investigated. Within the point dipole approximation, the effective contribution of this arrangement to the potential (and corresponding potential difference) may be calculated using

$$U = \frac{1}{4\pi\varepsilon_0}\frac{\mu_{\mathrm{S}}}{r^2}\cos\theta \ , \tag{4.7}$$

where μ_{S} is the molecular dipole moment of the solvent and θ is the angle between its direction and the axis that connects the solvent dipole moment and the C_6H_7 center.[86] In the arrangement as in Figure 4.7, the angle θ is 90° and the contribution to the potential is zero.

More accurate calculations require including the molecular shape and a realistic charge distribution in the molecule, and this was done with ab initio calculations for the C_6H_7 radical with several neighbouring polar molecules, as shown in the Figures 4.7 and 4.8. Hydrofluoric acid (HF) was used because it has a dipole moment of similar magnitude as that of water, and its simple structure and charge distribution gives a straightforward picture of the electric field direction. The structures of the molecules in Figure 4.7 were first optimised in vacuum. The arrangement shown in Figure 4.7 has a negligible effect on $A_{\mathrm{p}}^{\mathrm{met}}$. Another arrangement of the C_6H_7 radical and neighbouring molecules where two dipole moments were placed either side antiparallel and two were placed parallel on the axis of the C_6H_7 dipole moment was also explored, as shown in

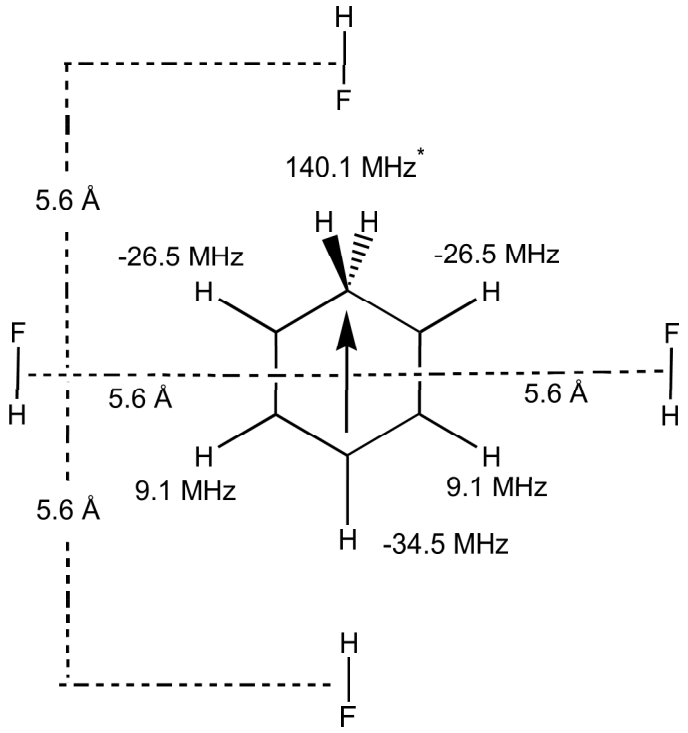

Figure 4.8: Results of ab initio calculations when the dipole moments are placed parallel along and either side antiparallel with respect to the cyclohexadienyl radical dipole moment axis. The hfcs are written next to the corresponding atoms for the given configuration. The arrow represents the dipole moment direction of the cyclohexadienyl radical. *gas phase (field=0): $A_{\mathrm{p}}^{\mathrm{met}}$=138.2 MHz (structures of the molecules in the figure were previously optimized in the gas phase).

Figure 4.8. The molecules on the dipole moment axis have a much larger effect on the $A_{\mathrm{p}}^{\mathrm{met}}$ than the off-axis molecules. This was one of the results of the RK dipole-dipole reaction field model. It is due to the cosine in eq. 4.7 that equals unity along the dipole moment axis but is zero for the off-axis solvent molecules.

Now the RK model for the case of the C_6H_7 radical in the liquids was tested. The in-plane ring protons reside in the nodal plane of the π system at zero nominal spin density from the semi-occupied molecular orbital. They acquire their non-zero hfc via spin polarization of the remaining π and the σ system, and the value of the hfc is proportional to the spin population at the adjacent carbon atom. In contrast, the two methylene hydrogen atoms are one above and one below the ring plane. A negative linear combination of their 1s wave functions has π symmetry and conjugates into the carbon π system. C_6H_7 is thus properly regarded as a 7-electron rather than a 5-electron π system.[47] Much of the methylene proton hfc arises from direct spin density in the semi-occupied molecular orbital. Nevertheless, the *ab initio* calculations

show that $A_{\mathrm{p}}^{\mathrm{met}}$ is directly proportional to the spin population $\rho_{\mathrm{C}}^{\mathrm{met}}$ at the methylene carbon atom:

$$A_{\mathrm{p}}^{\mathrm{met}} = A_{\mathrm{p}}^{0\prime} + c\rho_{\mathrm{C^{met}}} \ , \tag{4.8}$$

where $A_{\mathrm{p}}^{0\prime} = 197.77$ MHz and $c = 569$ MHz are constants typical for the radical and derived from ab initio calculations. $\rho_{\mathrm{C}}^{\mathrm{met}}$ is of the order of -0.103. When the RK model is applied, both $A_{\mathrm{p}}^{\mathrm{met}}$ and $\rho_{\mathrm{C^{met}}}$ should depend linearly on the electric potential difference between the methylene and the para carbon atom, $\Delta U_{\mathrm{C^{met}-C^{p}}}$:

$$\rho_{\mathrm{C^{met}}} = a + b\Delta U_{\mathrm{C^{met}-C^{p}}} \ , \tag{4.9}$$

and this is exactly what is derived from the ab initio calculations. a and b are constants typical for the system. By introducing eq. 4.9 into the eq. 4.8 the following is obtained:

$$A_{\mathrm{p}}^{\mathrm{met}} = A_{\mathrm{p}}^{0} + C'\Delta U_{\mathrm{C^{met}-C^{p}}} \ , \tag{4.10}$$

where $A_{\mathrm{p}}^{0} = A_{\mathrm{p}}^{0\prime} + a \cdot c$ and $C' = c \cdot b$. This linear dependence of $A_{\mathrm{p}}^{\mathrm{met}}$ on ΔU was confirmed from the ab initio calculations as shown in Figure 4.6, and the values of A_{p}^{0} and C' were determined to be 138.25 MHz and 3.94 MHz V^{-1}, respectively.

Using the same mathematical treatment as RK results in an equation of the same form as eq. 4.2 but with different constants. Thus, it may be concluded that the RK dipole-dipole reaction field model is appropriate to describe solute-solvent interactions in dipolar liquids for the C_6H_7 radical since $A_{\mathrm{p}}^{\mathrm{met}}$ depends linearly on the concentration of the dipole moments multiplied with the magnitude of the dipole moment (Figure 4.5, and eqs. 4.4 and 4.5) and $A_{\mathrm{p}}^{\mathrm{met}}$ is linearly dependent on the potential difference along the radicals´ dipole moment axis (Figure 4.6).

4.3.4 The dipole-quadrupole reaction field model

$A_{\mathrm{p}}^{\mathrm{met}}$ of C_6H_7 in benzene is 0.45 MHz larger than the corresponding value in octadecane and 0.7 MHz larger than the value in the gas phase (124.9 MHz at T=308 K).[34] This indicates that the potential difference in benzene is 0.18 V larger than in the gas phase and 0.13 V larger than in octadecane (assuming octadecane as an environment with zero reaction field, which disregards the effect of the weaker van der Waals forces).

In Figure 4.9, two preferential orientations of C_6H_7 and C_6H_6 are shown. In the upper one, the negative sector of the benzene quadrupole moment is oriented towards the positive end of the C_6H_7 dipole moment. In the second case, the positive sector of the quadrupole moment is oriented towards the negative end of the dipole moment.

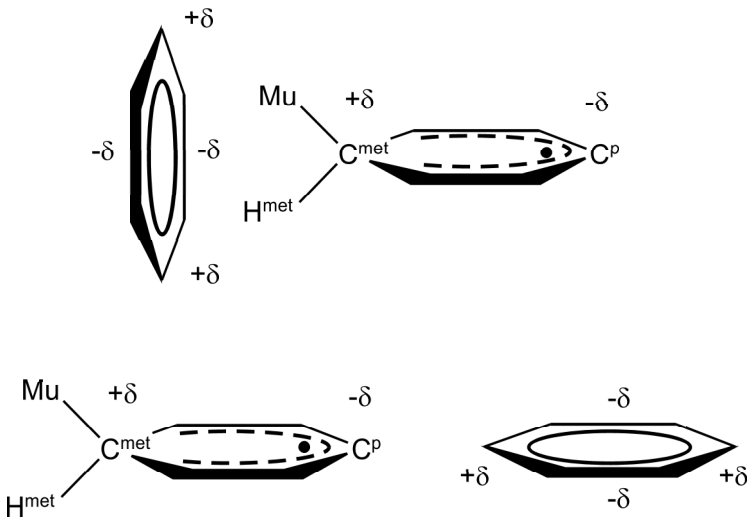

Figure 4.9: Arrangements of the benzene and the cyclohexadienyl radical (partial charge distribution simplified as in the figure).

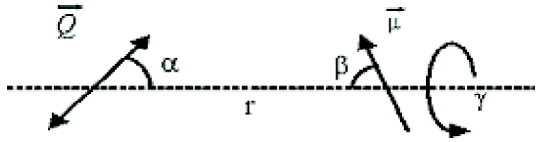

Figure 4.10: Orientation of the dipole moment vector and quadrupole moment tensor and definition of corresponding angles.

These two arrangements correspond to energy minima, however the treatment below takes into account all relative orientations. The analysis is based on the formalism introduced by Buckingham.[86] The average reaction field and the corresponding electric potential difference due to the solvent molecule electric quadrupole moment (in this case benzene) on the solutes dipole moment (in this case C_6H_7 radical) is calculated from the Boltzmann distribution.

The energy of the dipole-quadrupole interaction can be described by:[86]

$$E_{\mathrm{d-q}} = \frac{1}{4\pi\varepsilon_0}\frac{3}{2r^4} Q_{\mathrm{S}}\mu_{\mathrm{Solute}}(\cos\alpha(3\cos^2\beta - 1) + 2\sin\alpha\sin\beta\cos\beta\cos\gamma) \ , \qquad (4.11)$$

where Q_{S} and μ_{Solute} are the molecular electric quadrupole and electric dipole moments of solvent and solute molecules, respectively, r is the distance between their centers, and ε_0 is the vacuum dielectric constant. α, β and γ are the angles between the quadrupole moment and the dipole moment symmetry axes as defined in Figure 4.10. The relative orientation of the solvent electric quadrupole and of the solutes' electric dipole moment axes is given by the probability dW:

$$\mathrm{d}W_{\mathrm{Quad-Dip}} = \frac{\exp(\frac{E_{\mathrm{d-q}}(\alpha,\beta,\gamma)}{k_{\mathrm{B}}T})\mathrm{d}\alpha\mathrm{d}\beta\mathrm{d}\gamma}{\int_0^{2\pi}\int_0^{2\pi}\int_0^{2\pi}\exp(\frac{E_{\mathrm{d-q}}(\alpha,\beta,\gamma)}{k_{\mathrm{B}}T})\mathrm{d}\alpha\mathrm{d}\beta\mathrm{d}\gamma}\ , \tag{4.12}$$

where k_{B} is the Boltzmann constant. The electric (reaction) field, $R^{\mathrm{Field}}_{\mathrm{Quad}}$, produced by the quadrupole moment at the distance r is:[86]

$$R^{\mathrm{Field}}_{\mathrm{Quad}} = \frac{|Q_{\mathrm{S}}|}{4\pi\varepsilon_0 r^4}\frac{3\cos^2\alpha - 1}{2}\ . \tag{4.13}$$

The Boltzmann averaged reaction field that is due to the quadrupole moment of a single solvent molecule, $\overline{R^{\mathrm{Field}}_{\mathrm{Quad-Dip}}}$, on the solute dipole can therefore be written as:

$$\overline{R^{\mathrm{Field}}_{\mathrm{Quad-Dip}}} = \int_0^{2\pi}\int_0^{2\pi}\int_0^{2\pi} R^{\mathrm{Field}}_{\mathrm{Quad}}(\alpha)\frac{\exp(\frac{E_{\mathrm{d-q}}(\alpha,\beta,\gamma)}{k_{\mathrm{B}}T})\mathrm{d}\alpha\mathrm{d}\beta\mathrm{d}\gamma}{\int_0^{2\pi}\int_0^{2\pi}\int_0^{2\pi}\exp(\frac{E_{\mathrm{d-q}}(\alpha,\beta,\gamma)}{k_{\mathrm{B}}T})\mathrm{d}\alpha\mathrm{d}\beta\mathrm{d}\gamma}\ . \tag{4.14}$$

For the contribution of two solvent molecules located on the solute molecule dipole moment axis eq. 4.14 can be expressed for numerical treatment as:

$$\overline{R^{\mathrm{Field}}_{\mathrm{Quad-Dip}}} = 2\sum_0^{2\pi}\sum_0^{2\pi}\sum_0^{2\pi} R^{\mathrm{Field}}_{\mathrm{Quad}}(\alpha)\frac{\exp(\frac{E_{\mathrm{d-q}}(\alpha,\beta,\gamma)}{k_{\mathrm{B}}T})\mathrm{d}\alpha\mathrm{d}\beta\mathrm{d}\gamma}{\sum_0^{2\pi}\sum_0^{2\pi}\sum_0^{2\pi}\exp(\frac{E_{\mathrm{d-q}}(\alpha,\beta,\gamma)}{k_{\mathrm{B}}T})\mathrm{d}\alpha\mathrm{d}\beta\mathrm{d}\gamma}\ . \tag{4.15}$$

The potential difference is approximated with the electric field at the center of the C_6H_7 radical and the distance between the methylene and para carbons of the C_6H_7 radical (as previously done for the case of DTBN by RK):[17]

$$\Delta U = \overline{R^{\mathrm{Field}}_{\mathrm{Quad-Dip}}} d_{\mathrm{C^{met}-C^p}}\ . \tag{4.16}$$

$\overline{R^{\mathrm{Field}}_{\mathrm{Quad-Dip}}}$ is calculated using the mean distance from the radial distribution function (RDF) of liquid benzene for an estimate of the distance r between the C_6H_7 solute and the benzene solvent molecule. Several dynamics studies have been reported, and there is a good agreement among these studies on the observed values.[85,87] The first peak of the RDF, from which the distance is deduced, does not change significantly with temperature. Though benzene is an anisotropic molecule, a significant dependence of the RDF on the relative orientation is not observed. A shortcoming of this approach is that it neglects the significant dipole moment of C_6H_7. Therefore, there should be a larger angular dependence of the RDF in this system and the molecules would be closer to each other, due to the additional dipole-quadrupole interaction between the C_6H_7 radical and benzene. Using the value of $r \approx 5.6$ Å recommended by Chelli et al.,[85] $Q_{\mathrm{benzene}} = -2.9\times10^{-39}$ C m^2,[88] $d_{\mathrm{C^{met}-C^p}} \approx 2.9\times10^{-10}$ m, and $\mu_{\mathrm{C_6H_7}} \approx 1$ D with help

of adequate numerical routines[89] a potential difference of $\Delta U \approx 0.04$ V is obtained. This is 23% of what is required to give the necessary increase of the hfc of 0.45 MHz (compared to A_{μ}^{met} value in octadecane), but the calculation depends critically on the solute-solvent distance, as it scales inversely with its 4th power (eq. 4.14). Therefore, calculating the potential difference with a fixed value of r may not lead to a fully correct absolute value, but it may be used for estimating the relative differences among the quadrupolar liquids.

Furthermore, it is noted that r generaly scales with the cube root of the inverse concentration. Inserted into eq. 4.15 this means that the reaction field in quadrupolar solvents is proportional to the concentration of quadrupolar solvent molecules to the 4/3 power.

A further origin of the discrepancy between calculation and experimental results is that the electric point dipole and the electric point quadrupole moment approximations are not entirely valid on such a small distance between molecules. The agreement between the calculated (with the help of eq. 4.16) and the necessary potential difference values (obtained from the results of ab initio calculations, Figure 4.6) may still be considered as remarkably good, having in mind the uncertainty in the parameters used and the assumptions made in the calculations.

This study further suggests that other molecular properties of non-dipolar liquids should be used in the evaluation of the solvent-solute interactions such as higher multipoles, unusually large polarizability and preferred solute-solvent arrangements as well.

4.3.5 The influence of structure

The presence of electric field from the solvent molecule in the vicinity of C_6H_7 is expected to induce small changes in the structure of this relatively rigid radical, which in return influences the hfcs. There are three main variables in the system that can influence the $A_{\mathrm{p}}^{\mathrm{met}}$: (i) the distance between the methylene and the para carbon, (ii) the methylene C-H bond length and (iii) the bond angle between the methylene C-H bonds. It is very difficult to distinguish between these contributions, since the electronic structure of this radical is a function of numerous bond angles and bond lengths, some of which increase and some decrease the hfcs.[46] It can be seen in Figure 4.6 that the contribution due to electric field induced changes of the radical structure amounts to $\approx$ 15% of the overall $A_{\mathrm{p}}^{\mathrm{met}}$ change. The change of the C^{met}-C^{p} distance with electric field is very small, as seen in Figure 4.11. The change of the C^{met}-H^{met} bond length and of

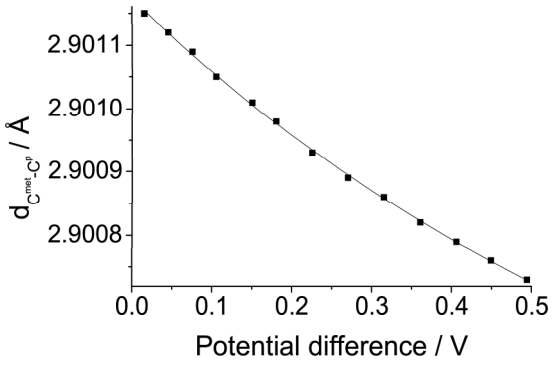

Figure 4.11: Ab initio calculations of the dependence of the methylene and para carbon atom distance (C^{met} and C^p in Figure 4.2) on the potential difference between the two atoms.

the angle between methylene C-H bonds is also small (not shown here; also noticed by Straka et al. for the C_6H_7-H_2O complexes[46]) but as can be seen from Figure 4.6, even small structural changes can have a considerable effect on A_p^{met}.

4.3.6 Temperature effects

The observed hfc of a radical represents a vibrational average over all internal degrees of freedom, and increased temperature leads to more extensive vibrational motion. The A_p^{met} of C_6H_7 increases linearly with temperature primarily due to the increased amplitude of the methylene scissor motion.[33] The contribution to the temperature dependence of the A_p^{met} due to vibrational effects is denoted as $(\Delta A_p^{met}/\Delta T)_{VIB}$. Furthermore, increased energy leads to greater disorder in a liquid and this will result in a decrease in the external electric field and a lower A_p^{met}. This contribution is denoted as $(\Delta A_p^{met}/\Delta T)_{HT}$. The A_p^{met} is also sensitive to the distance between the radical and the neighbouring solvent molecules. The density of a liquid generally decreases with increasing temperature and this leads to a larger radical-solvent distance, decreased $[\mu_S]$ value, and a lower A_p^{met}. The densities of the liquids studied in this experiment decrease to a first approximation linearly with temperature. The contribution due to the decreased density is denoted as $(\Delta A_p^{met}/\Delta T)_{DEN}$.

The change in the A_p^{met} due to vibrational averaging $(\Delta A_p^{met}/\Delta T)_{VIB}$ will be approximately the same in all solvents, assuming that rigidness of the cavity does not influence the structure. $(\Delta A_p^{met}/\Delta T)_{HT}$ and $(\Delta A_p^{met}/\Delta T)_{DEN}$ are unique for each solute-solvent mixture. It is reasonable to assume that all of these effects contribute

independently to the temperature dependence of the $A_{\mathrm{p}}^{\mathrm{met}}$, as shown in the following eq.:

$$\frac{\Delta A_{\mathrm{p}}^{\mathrm{met}}}{\Delta T} = (\frac{\Delta A_{\mathrm{p}}^{\mathrm{met}}}{\Delta T})_{\mathrm{VIB}} + (\frac{\Delta A_{\mathrm{p}}^{\mathrm{met}}}{\Delta T})_{\mathrm{HT}} + (\frac{\Delta A_{\mathrm{p}}^{\mathrm{met}}}{\Delta T})_{\mathrm{DEN}} \ . \tag{4.17}$$

The temperature dependence of $A_{\mathrm{p}}^{\mathrm{met}}$ in water will be discussed as a typical example where $(\Delta A_{\mathrm{p}}^{\mathrm{met}}/\Delta T)_{\mathrm{H_2O}}$ = -0.0183 MHz K^{-1} (Table 4.1). The absence of any intermolecular interactions in the gas phase means that the $A_{\mathrm{p}}^{\mathrm{met}}$ temperature dependence is entirely due to vibrational excitation, $(\Delta A_{\mathrm{p}}^{\mathrm{met}}/\Delta T)_{\mathrm{VIB}}$. Assuming that the intramolecular vibrations remain the same in the gas and in the liquid, it is possible to estimate the influence of these effects by comparing the results of studies of $A_{\mathrm{p}}^{\mathrm{met}}$ in the gas phase with this study. Fleming et al. determined that the temperature dependence of the $A_{\mathrm{p}}^{\mathrm{met}}$ in the gas phase was -0.0125 MHz K^{-1} or $\approx 68\%$ of the effect in water when compared with this experiments.[34]

By differentiating eq. 4.2 it is possible to determine the contribution of the density change:

$$(\frac{\Delta A_{\mathrm{p}}^{\mathrm{met}}}{\Delta T})_{\mathrm{DEN}} = B\frac{\mu_{\mathrm{S}}}{M_{\mathrm{S}}}\frac{\Delta \rho_{\mathrm{S}}}{\Delta T} \ . \tag{4.18}$$

Eq. 4.18 for the case of experimentally obtained dependence of $A_{\mathrm{p}}^{\mathrm{met}}$ on $[\mu_{\mathrm{S}}]$ at T = 308 K (eq. 4.4) is now used. This coefficient remains almost exactly the same at T = 348 K (eq. 4.5).

In the temperature range studied here the water density is approximately proportional to temperature. After introducing this coefficient and other constants ($\Delta\rho_{\mathrm{S}}/\Delta T(\mathrm{H_2O})$ = -0.44261 g K^{-1} dm^{-3}, $\mu_{\mathrm{S}}(\mathrm{H_2O})$ = 1.85 D, $M_{\mathrm{S}}(\mathrm{H_2O})$ = 18 g mol^{-1}) into eq. 4.18 it is found that $(\Delta A_{\mathrm{p}}^{\mathrm{met}}/\Delta T)_{\mathrm{DEN}}$ = -0.0008 MHz K^{-1}, which accounts for $\approx$4% of the effect (questioning significantly the conclusion reached by Griller[77]). The remaining temperature effect then has to be attributed to the increased solvent disorder, $(\Delta A_{\mathrm{p}}^{\mathrm{met}}/\Delta T)_{\mathrm{HT}}$, and it amounts to approximately 28% of the total effect. The factors influencing the hfcs´ temperature dependence can be resolved in a similar way for every solvent and mixture.

4.4 Conclusions

The methylene proton and muon hyperfine coupling constants of the cyclohexadienyl radical were measured in neat solvents and mixtures of various polarities between

octadecane, and water, and were found to be directly proportional to the concentration of the dipole moments multiplied with the magnitude of the dipole moment.

The hfcs of the cyclohexadienyl radical methylene protons are directly proportional to the potential difference between the methylene and para carbon atoms (defined in Figure 4.2), which is caused by the electric field that results from partial ordering of the dipole moments of the neighboring solvent molecules. The solvent molecules on the long axis of the cyclohexadienyl radical dominate the interaction in this solute-solvent system. Approximately 15% of the change of the methylene proton hfc is due to changes in the radical structure in the applied electric field.

The quadrupole moment of a solvent can have a large effect on the hfcs of the cyclohexadienyl radical and can be the dominant cause of interaction in non-dipolar solvents such as benzene. A dipole-quadrupole reaction field model has been developed to account for the variation of the hfcs of dipolar radicals in non-dipolar quadrupolar solvents. This model suggests that the reaction field scales with the product of the magnitude of the quadrupole moment and its concentration, $[Q_S]^{4/3}$, while in the case of the dipole moment scaling with $[\mu_S]$ is linear.

The temperature behaviour of the methylene proton hfc is mainly influenced by the thermal population of the vibrational modes ($\approx 68\%$ of the effect) and increased disorder of the neighboring solvent molecules due to the increased temperature ($\approx 28\%$ of the effect). The influence of the temperature dependence of the solvent density is almost negligible ($\approx 4\%$ of the effect).

The approach of the present study has several advantages in comparison with typically used continuum models.[15,30] It takes into account the fact that the radical hfc in liquids of similar dielectric constant may be very different, and it is in better agreement with the experimental results. The advantage in comparison with the study where the polarized continuum model with explicitly introduced water molecule is used,[46] is that it takes into account the behaviour not just in hydrogen bonding liquids.

This approach is general, since it describes the role of the electric field originating from the solvent molecules in the radical-solvent interaction. The influence of electric fields on radicals may be of importance not only in liquid-like environments. The present study emphasises the use of individual physical properties of the solvent molecules, such as the electric dipole and quadrupole moments (or exceptionally large polarizability), in describing solute-solvent interactions. Furthermore, it was shown that the interaction of one class of solvents may be approximated by that of the dominating solvent property.

It is sometimes necessary in chemical synthesis to have large reaction fields, which is usually achieved by using dipolar liquids. This study clearly shows how it is possible to achieve these fields in non-dipolar solvents by using the molecules with large electric multipole moments. This can be significant in cases where the solubility of reactants in dipolar liquids is the limiting factor.[8]

It is suggested here, that the dipole-dipole and its extension to include the dipole-quadrupole interactions is valid for other molecules and radicals as well. The potential radical for which these models should be valid must be rigid, because conformational changes can induce much larger differences of hyperfine coupling constants.[23] This radical should posses a dipole moment of considerable magnitude as well, to be able to cause some ordering in its vicinity.

5 Solvent effects on hydrogen adducts to 2-phenylethanol and 5-phenylpentanol

5.1 General remarks

Most molecules of biological as well as industrial relevance consist of functional groups with different characteristics. The overall behaviour of the molecule in different environments is a complex balance of all possible interactions. In this chapter the solvent effects on substituted cyclohexadienyl radicals were monitored, because they contain different functional groups and their influence on the hfcs was examined.

The hydrogen atom (in this study its light isotope muonium) adds itself to the phenyl ring of PEA and PPA molecules on three different positions with respect to the substituent group and as a result three different radicals are formed. They are named para, ortho and meta PEA-Mu and PPA-Mu radicals. Ortho, para and meta PEA-Mu radicals are shown in Figure 5.1. The corresponding PPA-Mu radicals are very similar, only the substituent hydroxyalkyl group is longer.

The absolute values $A_{\mathrm{p}}^{\mathrm{met}}$ of PEA-Mu radicals were measured using a method outlined in the section 3.2.3, as they are intended for use in Chapter 6. In order to perform this for the case of PPA-Mu radicals, it was necessary to know the corresponding $S = (A_{\mu}^{\mathrm{met}}/A_{\mathrm{p}}^{\mathrm{met}})$ ratios. To calculate the S ratios of PPA-Mu radicals, the A_{μ}^{met} and $A_{\mathrm{p}}^{\mathrm{met}}$ values in neat PPA were measured using the ALC- and TF-μSR techniques. The assignment of Δ_0 ALC- (shown in Figure 5.1) and TF-μSR resonances of PEA-Mu radicals' methylene protons and muons was performed by Scheuermann et al.[19,90] The same assignment remains valid for the PPA-Mu radicals due to the similar structure.

The aim in this chapter is to study the effects arising from the presence of the hydroxyalkyl substituent group in solvents of different polarities. The unpaired electron of the muoniated adduct radical is located in the π-electron system of the cyclohexa-

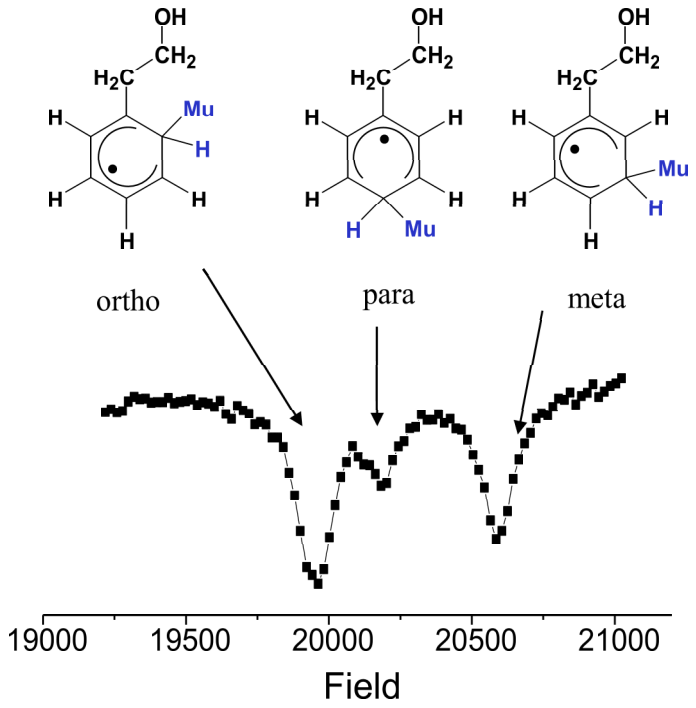

Figure 5.1: Ortho, para and meta PEA-Mu radicals and the assignment of the corresponding methylene protons to Δ_0 ALC resonances.

dienyl ring. Any variation in the relative behaviour of the hfcs with solvent polarity, defined by the $[\mu_S]$ value (as suggested by the RK theory), between the C_6H_7, PEA-Mu and PPA-Mu radicals will be attributed to an effect of the hydroxyalkyl substituent group.

In order to study the relative behaviour of the C_6H_7, PEA-Mu and PPA-Mu radicals a polarity diagram is used. A polarity diagram serves as a tool for monitoring the microenvironment of the muoniated radicals and is defined as a fractional shift of the methylene proton Δ_0 ALC resonance positions between the water as a most polar solvent (100% aqueous character (*aq.char.*)) and the octadecane as a nonpolar solvent (0% *aq.char.*) (eq. 5.1), plotted versus the $[\mu_S]$ value.[17] The % *aq.char.* unit in the environment X is given by:[90]

$$\%\ aq.char. = \frac{B_X - B_{\text{Octadecane}}}{B_{H_2O} - B_{\text{Octadecane}}}\ , \tag{5.1}$$

where B_X, $B_{\text{Octadecane}}$ and B_{H_2O} are the Δ_0 ALC resonance peak positions in the environment X, octadecane and water respectively. $[\mu_S]$ values were calculated using eq. 4.3.

In the case of ideal mixing of solvent molecules, the composition of the radicals

first solvent shell equals the macroscopic composition of the solution, and the trend of the % *aq.char.* is ideally linear. The polarity diagram serves, as well, for comparing the relative behaviour of $A_{\mathrm{p}}^{\mathrm{met}}$ of different radicals without knowing their absolute values.

The absolute value $A_{\mathrm{p}}^{\mathrm{met}}$ of the given radical in the environment X may be extracted from the % *aq.char.* using eq. 5.2:

$$A_{\mathrm{p}}^{\mathrm{met}}(\mathrm{X}) = A_{\mathrm{p}}^{\mathrm{met}}(\mathrm{Octadecane}) + \Delta A_{\mathrm{p}}^{\mathrm{met}}{}_{(\mathrm{H_2O-Octadecane})} \frac{\%aq.char.(\mathrm{X})}{100} , \qquad (5.2)$$

where % *aq.char.*(X) is the % aqueous character value in the environment X and $\Delta A_{\mathrm{p}}^{\mathrm{met}}{}_{(\mathrm{H_2O-Octadecane})}$ is the difference of $A_{\mathrm{p}}^{\mathrm{met}}$ between the H_2O and octadecane.

5.2 Results

5.2.1 Muon spin resonance experiments

Selected ALC-μSR spectra of PEA-Mu and PPA-Mu radicals in various environments and at different temperatures are presented in Figures 5.2 and 5.3. At constant temperature the ALC Δ_0 resonance shifts towards higher magnetic fields with increasing solvent polarity. The resonances shift towards lower fields linearly with increasing temperature, as seen in Figures 5.2 and 5.3. A similar behaviour was observed in all of the other solvents and mixtures studied in this chapter (not shown here).

A selected TF-μSR spectrum in the frequency domain of PPA-Mu radicals in neat PPA is presented in Figure 2.11. The transverse field resonances shift towards lower frequencies with increasing temperature.

5.2.2 Hyperfine coupling constants

5.2.2.1 Hydrogen adducts to 2-phenylethanol

The $A_{\mathrm{p}}^{\mathrm{met}}$ values of the PEA-Mu radicals in H_2O and octadecane were extracted from the Δ_0 ALC resonance peak positions using eqs. 3.3, 3.4 and 3.5 and listed in Table 5.1. The accuracy depends mainly on the validity of the approximation that S(ortho, para and meta PEA-Mu) = $A_{\mu}^{\mathrm{met}}/A_{\mathrm{p}}^{\mathrm{met}}$ remains the same in all solvents and mixtures. Due to the possible differences in the conformer ratios in different environments, in this case the accuracy of the $A_{\mathrm{p}}^{\mathrm{met}}$ calculations is expected to be smaller than for the case of the C_6H_7 radical. The absolute values of $A_{\mathrm{p}}^{\mathrm{met}}$ in other environments may be extracted

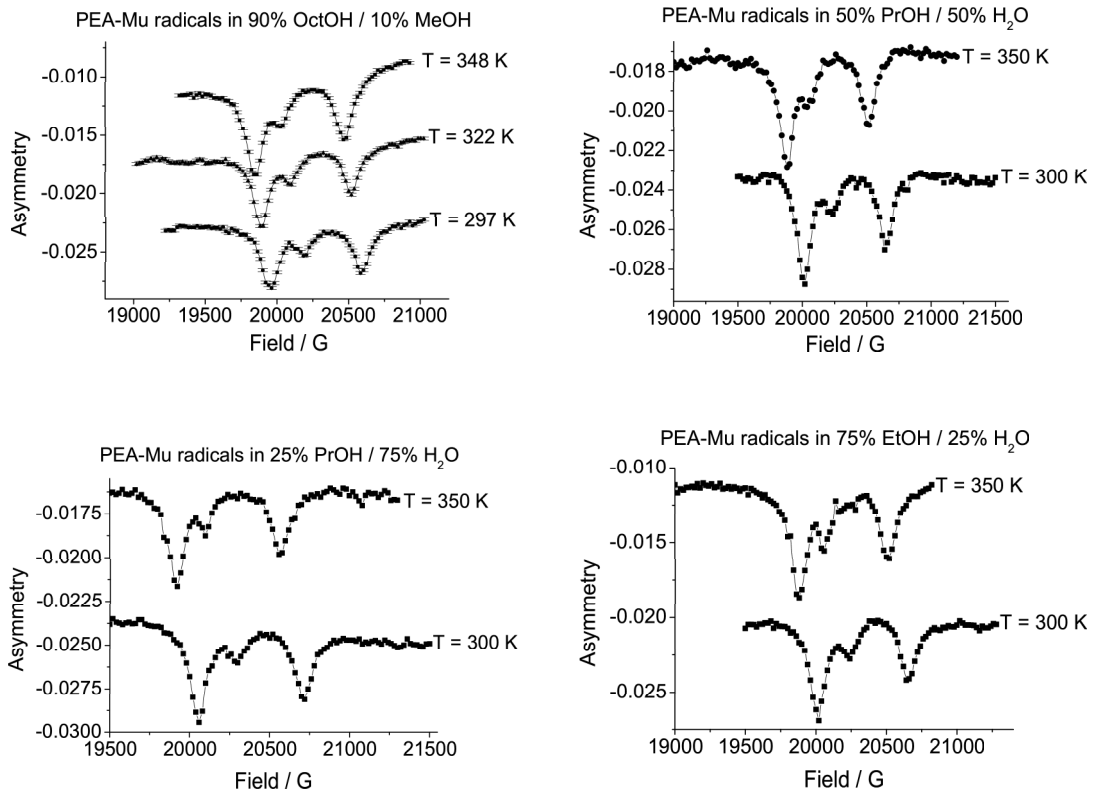

Figure 5.2: Selected ALC-μSR spectra of PEA-Mu radicals. Temperatures and environments are written next and above the corresponding spectra. Abbreviations as in List of abbreviations and symbols.

Table 5.1: $A_{\mathrm{p}}^{\mathrm{met}}$ of PEA-Mu radicals in octadecane and water at $T = 308$ K. Ortho, para and meta denote the corresponding PEA-Mu radical.

Environment	$[\mu_{\mathrm{S}}]$	$A_{\mathrm{p}}^{\mathrm{met}}$(ortho) / MHz	$A_{\mathrm{p}}^{\mathrm{met}}$(para) / MHz	$A_{\mathrm{p}}^{\mathrm{met}}$(meta) / MHz
Octadecane	0	120.5(2)	122.0(1)	124.7(2)
H_2O	103.1	122.1(2)	123.5(1)	126.7(8)

by using eq. 5.2. The % *aq.char.* values (and corresponding $A_{\mathrm{p}}^{\mathrm{met}}$) of all three PEA-Mu radicals depend approximately linearly on the $[\mu_{\mathrm{S}}]$ value, as displayed in Figure 5.5. The $A_{\mathrm{p}}^{\mathrm{met}}$ values decrease linearly with increasing temperature (temperature coefficients not shown here).

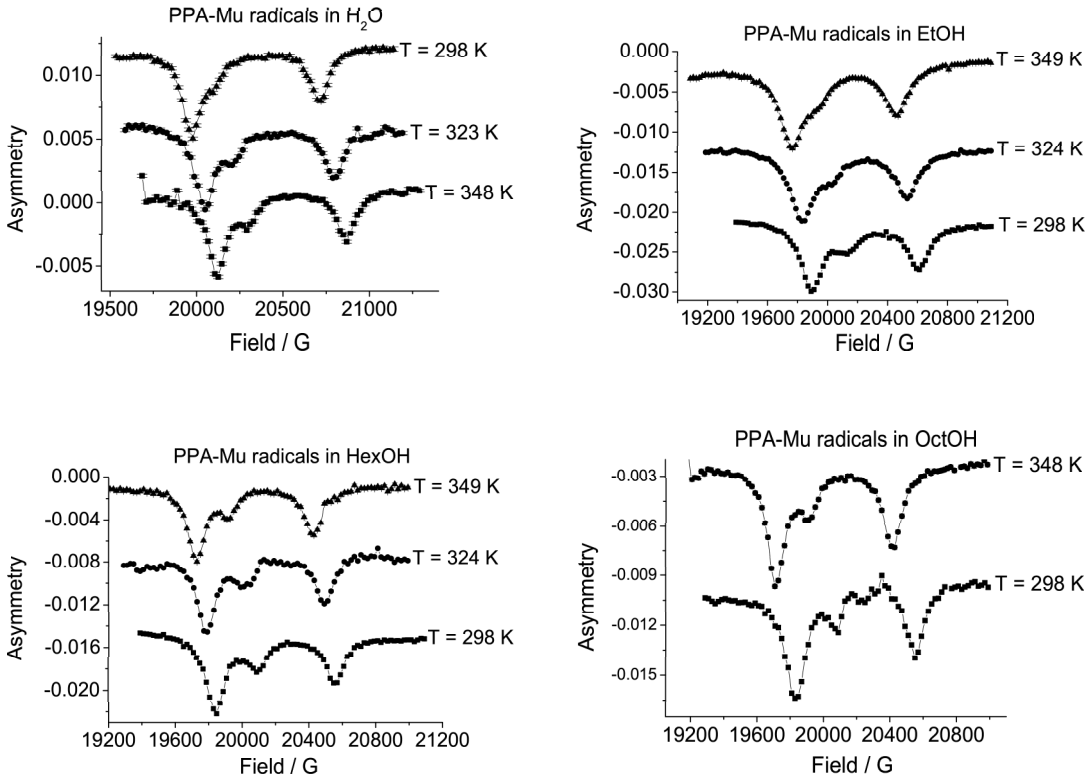

Figure 5.3: Selected ALC-μSR spectra of PPA-Mu radicals. Temperatures and environments are written next and above the corresponding spectra. Abbreviations as in List of abbreviations and symbols.

5.2.2.2 Hydrogen adducts to 5-phenylpentanol

The A_{μ}^{met} and $A_{\mathrm{p}}^{\mathrm{met}}$ values of the PPA-Mu radicals in neat PPA are listed in the Table 5.2. After the S(ortho, para and meta PPA-Mu) $= {A_{\mu}}^{\mathrm{met}}/A_{\mathrm{p}}^{\mathrm{met}}$ ratios were introduced into eq. 2.10, the $A_{\mathrm{p}}^{\mathrm{met}}$ value of the PPA-Mu radicals may be extracted using the following eqs.:

a) at $T = 308$ K

$$A_{\mathrm{p}}^{\mathrm{met}}(\text{ortho PPA-Mu}) = \frac{B_{\mathrm{r}}}{165.08}\frac{\mathrm{MHz}}{\mathrm{G}}\ , \tag{5.3}$$

$$A_{\mathrm{p}}^{\mathrm{met}}(\text{para PPA-Mu}) = \frac{B_{\mathrm{r}}}{168.99}\frac{\mathrm{MHz}}{\mathrm{G}}\ , \tag{5.4}$$

$$A_{\mathrm{p}}^{\mathrm{met}}(\text{meta PPA-Mu}) = \frac{B_{\mathrm{r}}}{164.07}\frac{\mathrm{MHz}}{\mathrm{G}}\ , \tag{5.5}$$

Table 5.2: Hyperfine coupling constants and $A_\mu^{\mathrm{met}}/A_\mathrm{p}^{\mathrm{met}}$ ratios of PPA-Mu radicals in neat PPA.

Ortho PPA-Mu				
Temperature / K	Resonance position / G	A_μ^{met} / MHz	$A_\mathrm{p}^{\mathrm{met}}$ / MHz	$A_\mu^{\mathrm{met}}/A_\mathrm{p}^{\mathrm{met}}$
300	19888.9	491.87	120.23	4.09
324	19829.5	490.53	119.99	4.09
349	19764.0	489.10	119.79	4.08
Para PPA-Mu				
Temperature / K	Resonance position / G	A_μ^{met} / MHz	$A_\mathrm{p}^{\mathrm{met}}$ / MHz	$A_\mu^{\mathrm{met}}/A_\mathrm{p}^{\mathrm{met}}$
300	20159.6	498.73	122.03	4.09
324	20068.3	496.74	121.74	4.08
349	19979.0	495.25	121.91	4.06
Meta PPA-Mu				
Temperature / K	Resonance position / G	A_μ^{met} / MHz	$A_\mathrm{p}^{\mathrm{met}}$ / MHz	$A_\mu^{\mathrm{met}}/A_\mathrm{p}^{\mathrm{met}}$
300	20626.2	510.85	125.42	4.07
324	20557.1	509.22	125.08	4.07
349	20484.0	507.61	124.84	4.07

b) at $T = 349$ K

$$A_\mathrm{p}^{\mathrm{met}}(\text{ortho PPA-Mu}) = \frac{B_\mathrm{r}}{164.99}\frac{\mathrm{MHz}}{\mathrm{G}} \ , \tag{5.6}$$

$$A_\mathrm{p}^{\mathrm{met}}(\text{para PPA-Mu}) = \frac{B_\mathrm{r}}{164.42}\frac{\mathrm{MHz}}{\mathrm{G}} \ , \tag{5.7}$$

$$A_\mathrm{p}^{\mathrm{met}}(\text{meta PPA-Mu}) = \frac{B_\mathrm{r}}{164.07}\frac{\mathrm{MHz}}{\mathrm{G}} \ , \tag{5.8}$$

where A_p values are given in MHz and B_r in G. By using these eqs. $A_\mathrm{p}^{\mathrm{met}}$ values of the PPA-Mu radicals in octadecane and H_2O were extracted from the corresponding Δ_0 resonance peak positions at $T = 308$ K and listed in Table 5.3. In the same manner as for PEA-Mu radicals, the absolute values of $A_\mathrm{p}^{\mathrm{met}}$ in other environments may be extracted by using eq. 5.2. The % *aq.char.* values (and corresponding $A_\mathrm{p}^{\mathrm{met}}$) of all PPA-Mu radicals depend linearly on the $[\mu_\mathrm{S}]$ value, as shown in Figure 5.6.

Table 5.3: $A_{\mathrm{p}}^{\mathrm{met}}$ of PPA-Mu radicals in octadecane and water at $T = 308$ K. Ortho, para and meta denotes the corresponding PPA-Mu radical.

Environment	$[\mu_{\mathrm{S}}]$	$A_{\mathrm{p}}^{\mathrm{met}}$(ortho) / MHz	$A_{\mathrm{p}}^{\mathrm{met}}$(para) / MHz	$A_{\mathrm{p}}^{\mathrm{met}}$(meta) / MHz
Octadecane	0	119.59	121.27	124.58
H_2O	103.1	121.04	122.71	126.72

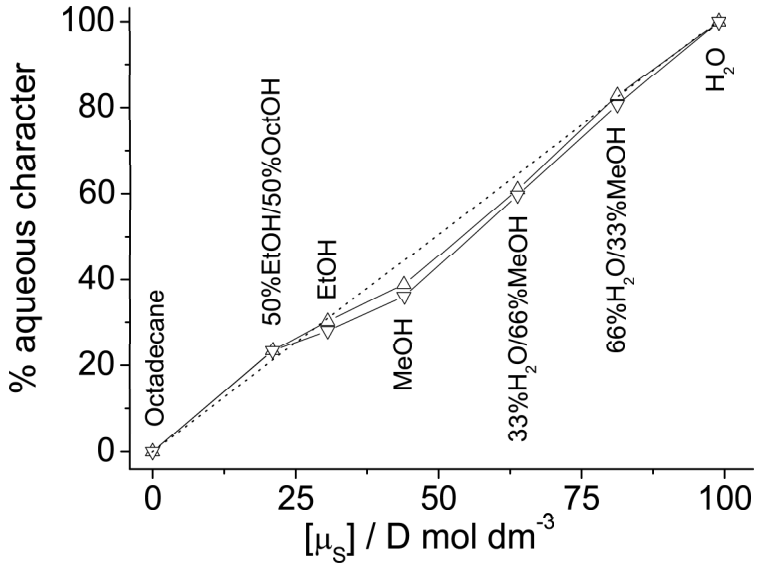

Figure 5.4: C_6H_7 radical: % aqueous character vs. $[\mu_{\mathrm{S}}]$ at 308 K ($\triangle$) and at 348 K (∇). Abbreviations as in List of abbreviations and symbols.

5.3 Discussion

In the following text, the relative behaviour of $A_{\mathrm{p}}^{\mathrm{met}}$ and the differences and similarities between the C_6H_7, PEA-Mu and PPA-Mu radicals are discussed. In order to better understand the solvent effects on the C_6H_7, the methylene proton Δ_0 ALC resonance peak positions (and corresponding $A_{\mathrm{p}}^{\mathrm{met}}$) on two different temperatures were plotted in % *aq.char.* units. As it can be seen in Figure 5.4, the % *aq.char.* values of the C_6H_7 radical are linearly dependent on the $[\mu_{\mathrm{S}}]$. Deviations from linearity (dotted line) are generally small. The largest deviation is for the C_6H_7 radical in neat MeOH. In the measurement in MeOH at $T = 308$ K the boiling point (T_{bp}(MeOH) = 338 K) is approached more closely than in any other environment investigated and therefore the intermolecular interactions are weaker than in other mixtures. Due to this fact

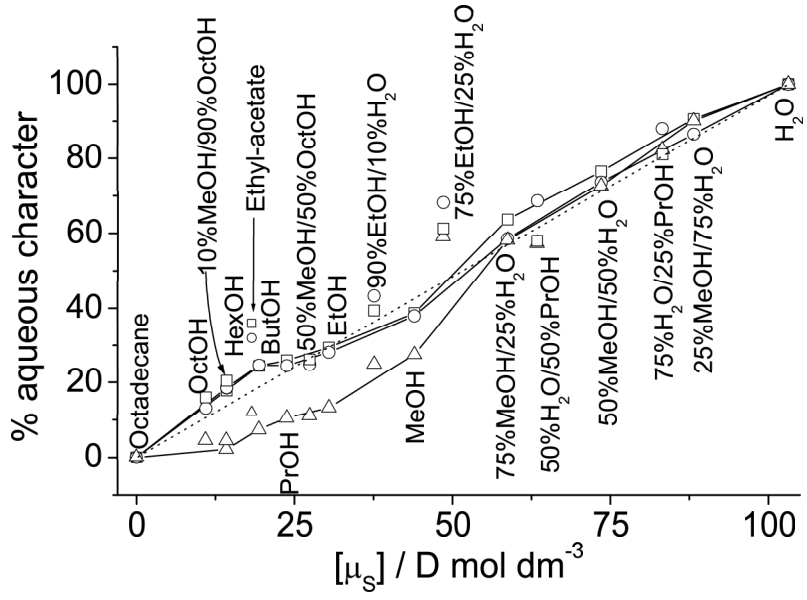

Figure 5.5: PEA-Mu radicals: % aqueous character vs. [μ_S] at 308 K: ortho PEA-Mu (□), para PEA-Mu (△), meta PEA-Mu (○). % aqueous character values in HexOH, ethyl-acetate, ButOH, PrOH, EtOH, MeOH, 75% MeOH/25% H_2O, 50% MeOH/50% H_2O and 25% MeOH/75% H_2O measured by Scheuermann et al.[19] Abbreviations as in List of abbreviations and symbols.

the ordering in the first solvent shell is smaller and it leads to a smaller value of the time averaged (on the time scale of muon life time) electric dipole moment of the first solvation shell. At $T = 348$ K, this effect is even more pronounced. At this temperature the liquid is already above the boiling point at atmospheric pressure. When MeOH molecules are mixed with water, the boiling temperature of the mixture is higher, and the Δ_0 resonance fields and corresponding % *aq.char.* values are back very close to the ideal behaviour.

As seen in Figure 5.5 the % *aq.char.* values of PEA-Mu radicals behave in general linearly with certain differences observed among them. The electric dipole moments of PEA-Mu and of PPA-Mu radicals are the vector sums of the electric dipole moment of the muoniated phenyl ring and the OH group. Addition of Mu to the PEA and PPA in ortho, meta and para position therefore results in their adduct radicals having slightly different dipole moments, both with respect to the magnitude and the direction, and therefore they behave differently. Ortho and meta PEA-Mu radicals behave similarly to the C_6H_7 radical, thus showing that the substituent group on these positions has no

significant influence. The para radical, however, in the environments where no water is present, feels a much smaller polarity than in the ideal case. This is attributed to the difference in intramolecular hydrogen bonding between the OH group from the substituent hydroxyalkyl group and the π-electrons from the cyclohexadienyl ring in water and in alcohols. This will be examined in more details in Chapter 6.

The largest deviation from ideal behaviour (far more than any experimental error) is for the 75% EtOH/25% H_2O mixture. This means that the first solvation shell around the cyclohexadienyl ring contains more water molecules than given by the macroscopic composition of the mixture. The same effect is observed for the 90% EtOH/10% H_2O mixture as well. One possible explanation is that a very pronounced effect of preferential solvation takes place here. Preferential solvation was observed in the past with several techniques: conductance measurements,[91] NMR measurements of the chemical shift of a nucleus in the solute,[92,93] measurements of the solvatochromism in the IR region,[94] measurements of the solvatochromism in the UV region[95,96] and in other cases.[97–99] In the recent neutron scattering study of 70% MeOH/30% H_2O mixture it was noticed that MeOH and H_2O molecules do not mix microscopically.[99] This effect is expected to be more pronounced in the case of EtOH/H_2O mixtures, since the hydrophobicity of EtOH is larger. On the other hand the radical is larger than the solvent molecules and it significantly interferes with the structure of the solvent. What is measured here is the environment around the cyclohexadienyl ring, whereas the OH group of the hydroxyalkyl chain contributes to the preferential solvation by attracting the more polar molecules. In this case these are H_2O molecules, and what is observed from the polarity graph is that they have pushed out EtOH molecules from the first solvent shell. In other similar cases (50% PrOH/50% H_2O and 25% PrOH/75% H_2O) this is not observed since the mixture is already in the $[\mu_S]$ region where water is the dominating component of the solvent. The $[\mu_S]$ values of the 10% MeOH/90% OctOH mixture and of HexOH are the same. The corresponding % *aq.char.* is the same as well, thus showing that MeOH and OctOH do not expell each other from the first solvation shell.

In the previous studies, instead of $[\mu_S]$ values the C_{OH} (concentration of OH groups in the given solvent) or ε value was used.[19,90] In both cases the A_p^{met} value of PEA-Mu radicals in ethyl-acetate did not follow the proportionality to dielectric constant ($\varepsilon = 6.0$) or to the concentration of OH groups (which is zero in case of ethyl-acetate). Using $[\mu_S]$ has the advantage in the case of PEA-Mu radicals in ethyl-acetate. The % *aq.char.* value in ethyl-acetate is now very close to the linear behaviour as in other solvents, as seen in Figure 5.5.

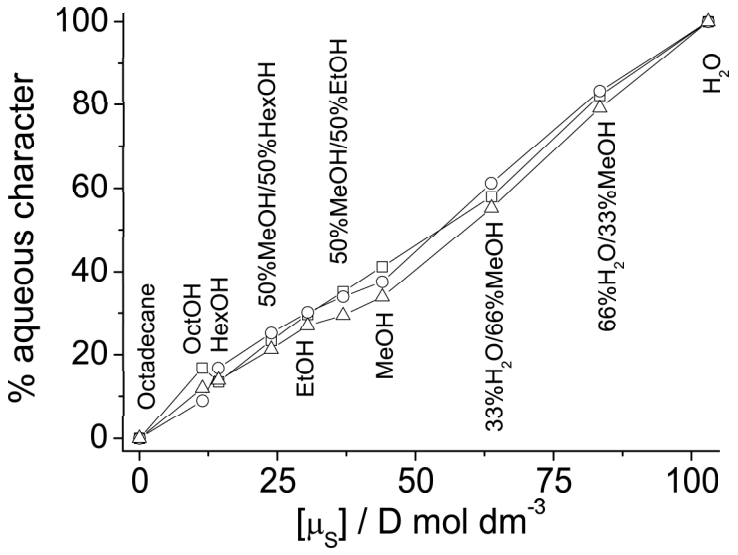

Figure 5.6: PPA-Mu radicals: % aqueous character vs. $[\mu_S]$ at 308 K: ortho PPA-Mu (□), para PPA-Mu (○) and meta PPA-Mu (△). Abbreviations as in List of abbreviations and symbols.

In the measurements performed on the PPA-Mu radicals it is observed that all radicals behave linearly, more "normal" than in the case of PEA-Mu radicals. When the substituent group is longer, the perturbation on the cyclohexadienyl ring due to the OH group is much smaller than in the case of PEA-Mu radicals. Therefore the behaviour of the % *aq.char.* value and the corresponding hyperfine coupling constants approach the behaviour of that of the C_6H_7 radical.

As seen, the % *aq.char.* values (and corresponding A_p^{met} values) of PEA-Mu and PPA-Mu radicals in general depend linearly on the $[\mu_S]$ value with some deviations originating in the presence of the substituent group. Therefore, the validity of the RK dipole-dipole reaction field model is confirmed for the case of substituted cyclohexadienyl radicals.

5.4 Conclusions

The % aqueous character values (and corresponding Δ_0 resonance fields and A_p^{met}) of hydrogen adducts to 2-phenylethanol and 5-phenylpentanol were monitored in neat solvents and mixtures of various polarities, and were found to be in overall linear dependence on the $[\mu_S]$ value. This corresponds to the behaviour predicted by the

dipole-dipole reaction field model of Reddoch and Konishi.[17]

The deviations from linearity are explained with the differences in the microscopical solvent properties, preferential solvation and different hydrogen bonding effects. To understand more precisely the behaviour of substituted cyclohexadienyl type radicals, the hydrogen bonding effects should be examined in more details. Even small differences in the magnitude and the direction of the electric dipole moment of the radical have an observable impact on the first solvent shell of the solute radical. The perturbation on the π-electrons, due to the OH group is smaller as the hydroxyalkyl substituent group is longer.

These effects are important to understand in view of the work where these radicals are used to probe ordered surfactant dispersions, where the % aqueous character value is used to determine the probe molecule location in bilayer structures and the partitioning of these molecules between the aqueous and the lipid bilayer phases.[19,20,100]

6 Conformational studies of hydrogen adducts to 2-phenylethanol and 5-phenylpentanol

6.1 General remarks

The hydrogen adducts to PEA and PPA contain both hydrophobic and hydrophilic groups and thus their microenvironment is not homogeneous, as previously shown in Chapter 5. In the region close to the hydrophilic -OH group a stronger interaction with the polar solvent molecules is expected. Due to this interaction, depending on the environment, the conformation may vary and this is particularly studied here.

In the folded conformation the substituent hydroxyalkyl group bands back and interacts with the π-electrons of the phenyl ring, as shown in Figure 6.1, left-hand side. The non-folded one is where no folding of the hydroxyalkyl group takes place and the OH group is in a position that does not allow its interaction with π-electrons (Figure 6.1, right-hand side).

The folding of the PEA molecule caused by the nonclassical hydrogen bonding interaction between the H atom from the hydroxyalkyl substituent group and π-electrons from the phenyl ring in the PEA molecule (as in Figure 6.1) was suggested to play an important role in stabilising its structure and in its activity.[101] Barnard et al. first sug-

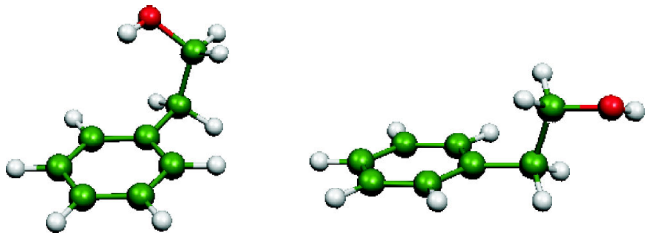

Figure 6.1: Folded (left) and non-folded (right) conformation of 2-phenylethanol.

gested this kind of intramolecular hydrogen bonding.[102] Schleyer et al. and references mentioned in their study agreed,[103] but Mateo and Cram opposed this idea.[104] A more quantitative approach to the problem demanded a study of molecules in the gas phase. Kirchner and Richter found in the gas phase IR study intramolecular bonding energy to be 11 kJ mol^{-1}.[105] Spassov et al. in their ^{1}H NMR and the IR study in CCl_4 solution concluded that it is 6.7 kJ mol^{-1}.[106] More recently Godfrey et al. and Dickinson et al. also confirmed the presence of both folded and non-folded conformations in the gas phase.[101,107] Both studies concluded that the folded conformation is the most stable one. The preferential conformation of PEA may be modified by complexation with water or other protic solvents.[21,22] Qualitatively the same is expected for PEA-Mu radicals. The main shortcoming of these studies from the practical point of view is that they were performed in environments (the gas phase, clusters with water molecules in the gas phase and CCl_4 solvent) very different from the realistic situation.

The relative behaviour of A_p^{met} values of PEA-Mu and of PPA-Mu radicals in isotropic environments of different polarities was monitored in Chapter 5 and they showed, in general, a linear dependence on the increased solvent polarity with certain differences among the radicals. It is noticed that A_p^{met} values show the largest deviation from the ideal linearity in the solvents and mixtures where no water molecules were present (Figure 5.5). The largest deviation of A_p^{met} was observed for the para PEA-Mu radical, as displayed in Figure 6.2. The most interesting feature in Figure 6.2 is the discontinuous increase of A_p^{met} at low water concentrations (between zero and 25% in MeOH, and between 10% and 25% in EtOH).

Understanding these deviations inspired the present conformational studies of PEA-Mu and PPA-Mu radicals, and in particular, the main aim is to understand the significant deviation of the para PEA-Mu % *aq.char.* value (and corresponding A_p^{met}). PPA-Mu radicals are studied here for comparison, since they reflect the influence of non-folded conformation.

In the present study interest focuses on the situation in the cell-like environments, highly polar water, polar MeOH and nonpolar octadecane.

The present study aims to develop a method for examining the conformational changes of cyclohexadienyl type radicals in the isotropic liquids of different polarity in order to allow the future monitoring of the conformations of these radicals inside the cell membrane-like environments such as surfactants and micelles using the μSR technique. Information about the preferred orientation of substituent hydroxyalkyl groups was extracted from β-methylene proton hfcs (A_p^{β}) of PEA-Mu and PPA-Mu radicals using the McConnell relations (section 2.1).[45]

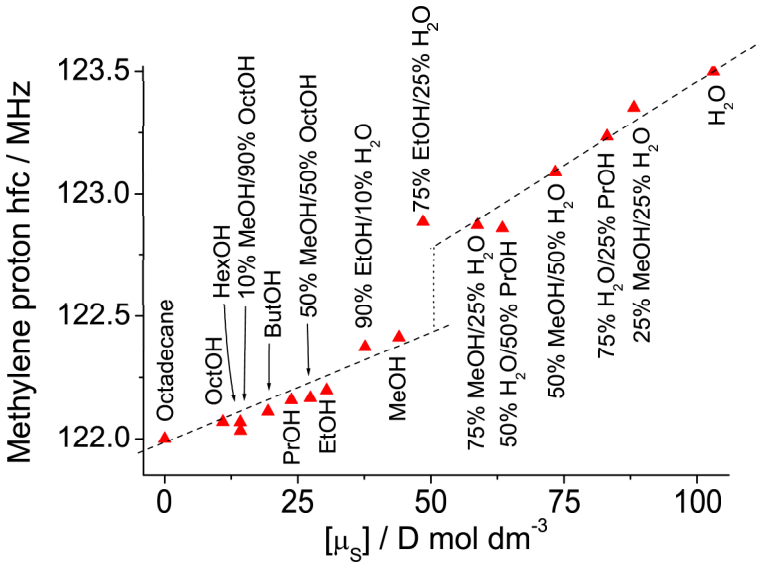

Figure 6.2: $A_{\mathrm{p}}^{\mathrm{met}}$ of the para PEA-Mu radical as a function of the $[\mu_{\mathrm{S}}]$ value at T=308 K. The discontinuous increase of $A_{\mathrm{p}}^{\mathrm{met}}$ is noted with the doted line. Abbreviations as in List of abbreviations and symbols.

The hfcs of in-plane ring protons of the PEA-Mu and PPA-Mu radicals were reported here as well, and compared with the values measured for the C_6H_7 radical. β-methylene and in-plane proton Δ_0 ALC resonances were observed here for the first time and a new strategy for the assignment of these resonances was developed and applied for PEA-Mu radicals. The assignment remains the same for PPA-Mu radicals, since they have a similar structure.

Ab initio calculations of the PEA-H and PPA-H radicals, and of PEA-H-H_2O clusters in the gas phase were also performed. Limited by available computational resources, PEA-Mu and PPA-Mu radicals are modelled by PEA-H and PPA-H, respectively. The aim was further to contribute to the understanding of the effects of real water molecules on the conformational balance of PEA-Mu and PPA-Mu radicals.

6.2 Strategy for the assignment of resonances

The strategy for the assignment of Δ_0 ALC resonances is based on the following principles. This strategy is applicable to the assignment of ALC Δ_0 resonances in the case of other radicals, not just to cyclohexadienyl type radicals.

1) The assignment may be carried out by comparing the expected theoretically

calculated (for the given hfc values) ratio of the resonance amplitudes (methylene vs. other protons' resonances) with the ratio of resonance amplitudes observed in the experiment.

The amplitude of a given Δ_0 ALC resonance is first theoretically calculated for the given A_μ^{met} and A_p values of each radical (according to eqs. 2.12 and 2.13). The same is obtained using the experimentally observed resonance amplitudes. The ratio of theoretically and experimentally obtained Δ_0 ALC resonance amplitude ratios, the parameter R, is then:

$$R = \frac{(\frac{I_{\mathrm{met}}}{I_{\mathrm{other}}})_{\mathrm{Theor.}}}{(\frac{I_{\mathrm{met}}}{I_{\mathrm{other}}})_{\mathrm{Exp.}}} \ . \tag{6.1}$$

By dividing the experimentally and theoretically calculated resonance ratios the R parameter is obtained and it should be as close as possible to 1 ($R \approx 1$). Due to experimental imperfections it is not always so. There are always the three possibilities that the resonance belongs to the ortho, para or meta PEA-Mu radical and the R parameter is calculated for each of them.

2) The resonance belonging to the proton whose A_p is higher is more likely to appear.

As shown in eq. 2.12 the amplitude of the resonance is non-linearly related to the A_p, but the resonance of the higher A_p is always of larger amplitude. Since the resonances obtained here are expected to have small amplitudes, the resonance with a larger hfc value is more likely to be observed.[50]

3) The resonance of the radical present in a larger yield in the system is more likely to appear.

Ortho and meta PEA-Mu radicals are formed in approximately two times larger yield than the para PEA-Mu radicals. Therefore, the Δ_0 ALC resonances of ortho and meta PEA-Mu radicals should be more intensive than that of the para PEA-Mu radical.

4) The hfc values obtained from ab initio calculations and other experiments on similar radicals should be compared to the results of the present study.

In particular, it is expected that the in-plane ring proton hfc values of PEA-Mu do not differ significantly from that of C_6H_7 at the same position.

5) A comparison of the ALC spectra of non-deuterated and selectively deuterated radicals should be performed if necessary.

In some cases it may still remain uncertain whether the observed resonance be-

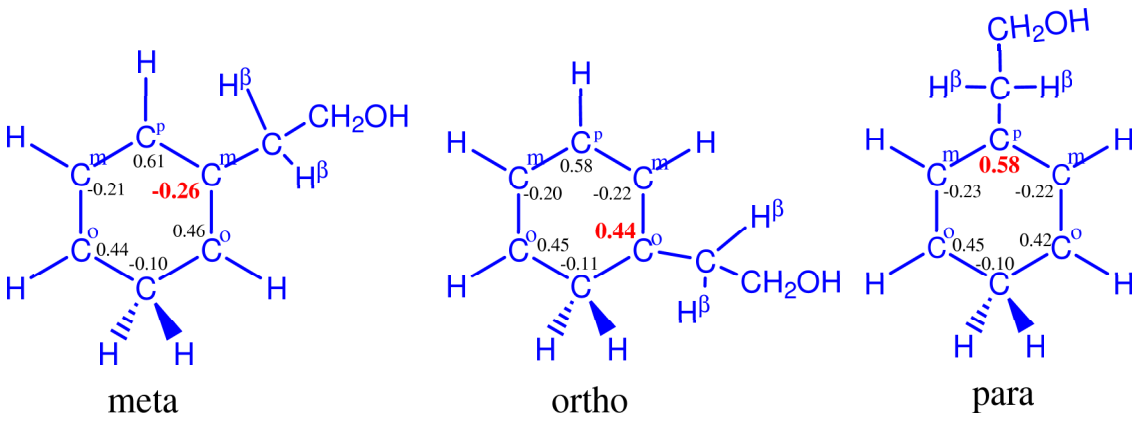

Figure 6.3: Spin population distribution (numbers next to the corresponding carbon atoms) on the rings of PEA-H radicals in the gas phase, folded conformation, according to the results of ab initio calculations. Meta denotes the meta PEA-H radical, para denotes the para PEA-H radical and ortho denotes the ortho PEA-H radical. The spin population distribution is very similar for PPA-H radicals (not shown here).

longs to the in-plane ring protons or to the β-methylene protons. Therefore, the comparison with the spectra of hydrogen adducts to PEA selectively deuterated at the ring position (in-plane protons' ALC resonances diminish) and at the substituent group position (β-methylene protons' ALC resonance diminishes) were measured. These spectra also serve as a check for the assignment of lines.

6) The spin population distribution of the radicals has to be taken into account.

The spin population distribution on the phenyl ring of cyclohexadienyl type radicals is determined by the hydrogen atom addition site. The molecular orbital of the cyclohexadienyl radicals, that mainly determines the spin population distribution on the ring has its node on the meta ring carbon atom (C^m in Figure 6.3).[47] In the case when the substituent group is bonded to the phenyl ring at the C^m position as for the meta PEA-Mu radical (Figure 6.3), the spin population (bold in Figure 6.3) at this position is the smallest and not much of the spin density remains to be transferred to the substituent group and in particular to the β-methylene protons. On the other hand this orbital has its maxima at the ortho and para ring carbon atoms (C^o and C^p in Figure 6.3),[47] thus resulting in a large amount of spin density being transferred to the substituent group and in particular to the β-methylene protons. The main consequence of these facts is that it is not expected to observe the ALC Δ_0 resonances of the meta PEA-Mu β-methylene protons.

6.3 Results

6.3.1 The assignment of resonances

A representative spectrum of the in-plane ring and β-methylene proton PEA-Mu radical resonances is shown in Figure 6.4. In addition to this, the field ranges of 24000-25000 G and 30000-31000 G were also examined, but no additional resonances were observed. All resonances are of relatively weak amplitude, due to the low A_{p} of these protons. A_{p} values were extracted from the Δ_0 ALC resonance peak position using the procedure outlined in section 3.2.3. It must be noted that the accuracy depends mainly on the correct $S(\text{PEA-Mu}) = A_{\mathrm{p}}^{\mathrm{met}}/A_{\mu}^{\mathrm{met}}$ ratio used for the determination of the A_{μ}^{met} of PEA-Mu radicals.

Dashed lines in Figure 6.4 denote the field positions where A_{p} of PEA-Mu radicals would equal zero and divide the ALC spectrum into two parts. One where resonances with positive A_{p} appear ($A_{\mathrm{p}}>0$ in Figure 6.4) and the other where negative A_{p} appear ($A_{\mathrm{p}}<0$ in Figure 6.4). The spectrum consists of four resonances with positive A_{p} and of six resonances with negative A_{p} values. Each resonance may belong to any of the PEA-Mu radical protons (denoted in Figure 6.4 with o, p and m for the corresponding otho, para and meta PEA-Mu radicals respectively) with the corresponding hfc value (underlined numbers). In order to assess which radical the resonance belongs to, the R parameters (*italic* numbers in Figure 6.4) were calculated for each possibility. As can be seen in Figure 6.4 using this methodology in the assignment of resonances gives very straightforward results for most of the resonances.

Using the R parameter allows a certain assignment in the higher magnetic fields ($A_{\mathrm{p}}<0$) part of the spectrum. It is immediately clear that these resonances belong to the in-plane ring protons of the PEA-Mu radicals. The splitting into two resonances at ≈29000 G (right hand side in Figure 6.4) is due to the fact that none of the in-plane ring protons are magnetically equivalent. All results were compared in Table 6.1 with the hfc values of the in-plane protons of the C_6H_7 radicals measured by Fleming et al.,[34] and they show a very good agreement. The final assignment of these resonances is shown in Figure 6.5. The assignment of the resonances belonging to protons with positive $A_{\mathrm{p}}^{\mathrm{met}}$ was not so straightforward. The major surprise in this part of the spectrum were the appearance of a resonance at ≈26400 G and the splitting into two resonances at ≈25900 (Figure 6.4).

The resonance at ≈26400 G shows approximately the same R values for the cases when it belongs both to the ortho PEA-Mu and para PEA-Mu radicals. Taking into

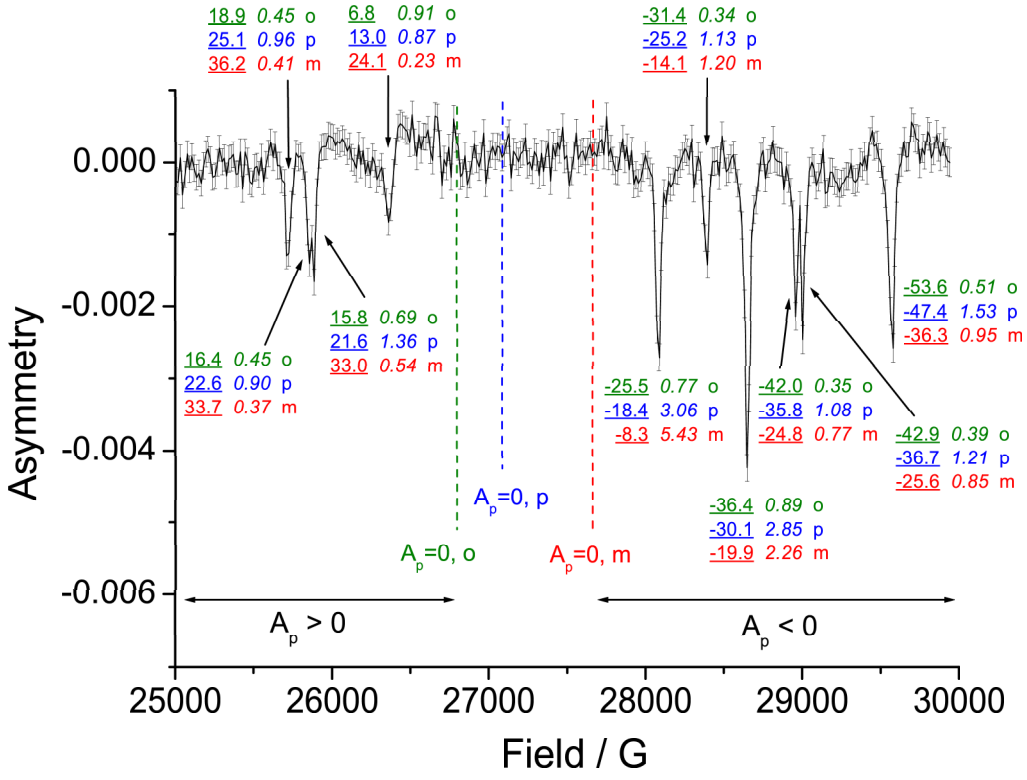

Figure 6.4: ALC spectrum of PEA-Mu radicals in H_2O at T=298 K. Hyperfine coupling constants in MHz (underlined), R parameter of the given resonance (in *italic*) for the ortho (denoted with o), para (p) and meta (m) PEA-Mu radical. Magnetic field positions where the hyperfine coupling constant values of PEA-Mu radicals equal to zero are denoted with dashed lines.

Table 6.1: Comparison of PEA-Mu hfcs (in D_2O, T=298 K) with the hfcs of C_6H_7 radical. A_p^o, A_p^m and A_p^p denote the ortho, meta and para in-plane ring protons' hfcs with respect to the substituent group as defined in Figure 4.2. Values given in MHz units. Abbreviations as in List of abbreviations and symbols.

	A_μ^{met}	A_p^o	A_p^m	A_p^p	A_p^β
C_6H_7[34]	504.9	-24.8	8.2	-36.2	
ortho PEA-Mu	498.3	-25.5	6.9	-36.4	+16.6/+15.9
para PEA-Mu	504.5	-25.1			+25.2
meta PEA-Mu	515.7	-24.6/-25.5		-36.3	

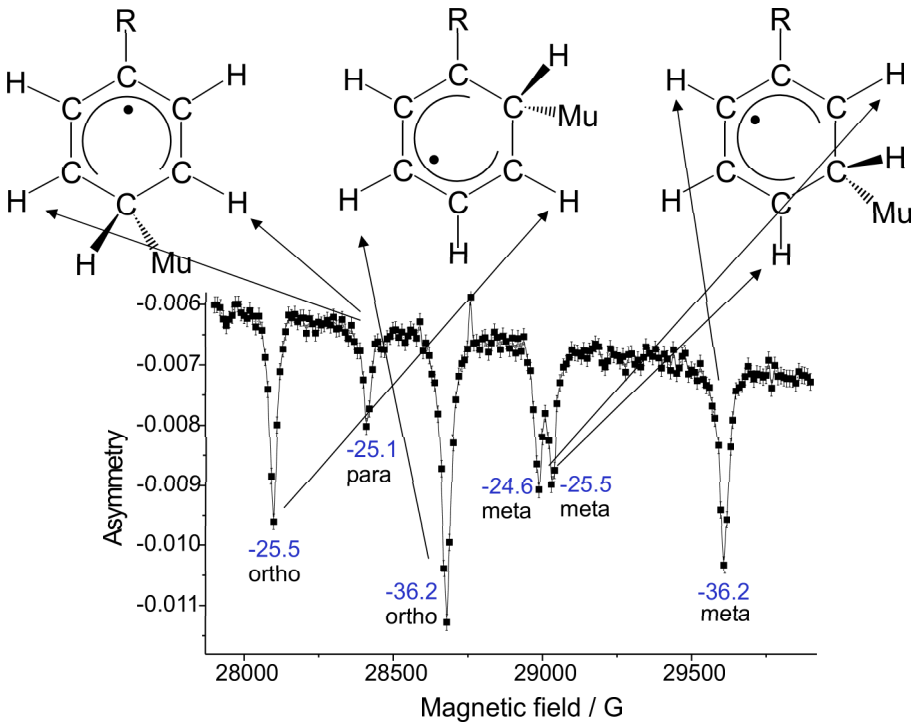

Figure 6.5: ALC spectrum of PEA-Mu radicals in D_2O at T=298 K and the assignment of corresponding resonances, higher fields. The belonging of the resonance to the PEA-Mu radical is denoted below the corresponding hfc value. Ortho, para and meta denotes to which PEA-Mu radical a resonance is assigned. R denotes the -CH_2-CH_2-OH group.

account the spin population distribution on the phenyl ring (Figure 6.3) the resonances of the β-methylene protons of the meta PEA-Mu radical were not expected to be observable. Taking this into account, it may be concluded that this resonance may belong either to the in-plane ring proton of the ortho PEA-Mu radical or to the in-plane ring or β-methylene protons of the para PEA-Mu radical. Therefore, it was necessary to perform an additional experiment on selectively deuterated PEA-Mu radicals.

Representative spectra of the corresponding radicals (deuteration at the hydroxyalkyl group denoted PEA-d1,d1,d2,d2-Mu; deuteration at the phenyl ring denoted PEA-d5-Mu) were compared to the spectra of the nondeuterated PEA-Mu radicals and presented in Figure 6.6. These spectra once again confirm the previous conclusion that the resonances with negative A_p belong to the in-plane ring protons. As can be seen in Figure 6.6 the resonance at ≈26400 G (marked with the dashed line) disappears when the radical was deuterated at the ring position and it is immediately clear that this resonance belongs to the in-plane ring proton. Now it is only left to discern whether the resonance at ≈26400 G belongs to the in-plane ring proton of the para or of the ortho PEA-Mu radical. Again this was done by comparing it to

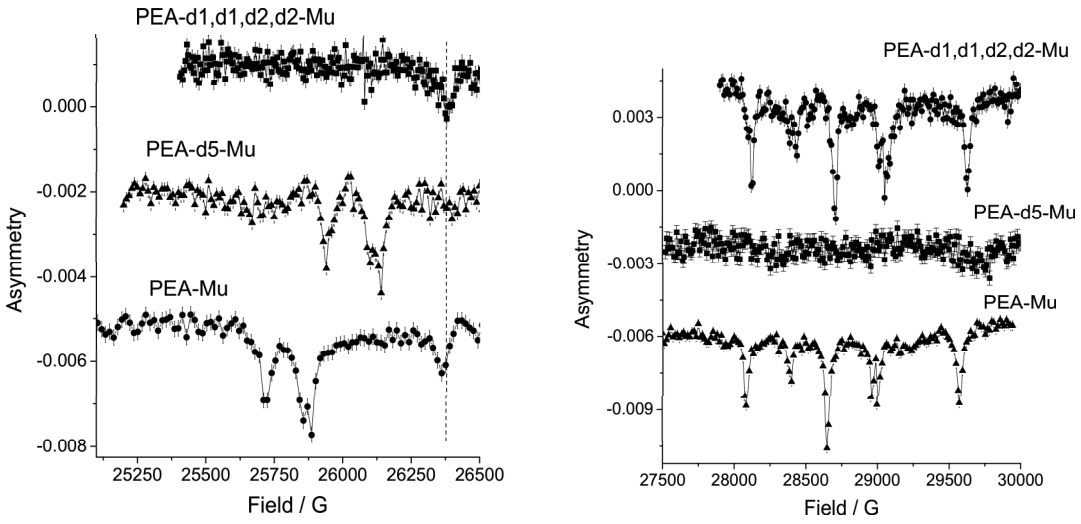

Figure 6.6: Comparison of ALC-μSR spectra of selectively deuterated PEA-Mu radicals with the one of nondeuterated PEA-Mu radicals. Deuteration at the ring position (denoted above the corresponding spectra as PEA-d5-Mu), at the hydroxyalkyl chain position (PEA-d1,d1,d2,d2-Mu). Nondeuterated denoted as PEA-Mu.

the hfcs of in-plane ring protons of C_6H_7 measured by Fleming et al.[34] The greatest similarity of A_p was observed for the in-plane meta ring proton of ortho PEA-Mu radical (A_p^m(ortho PEA-Mu) = 6.9 MHz, Table 6.1) and of the same proton of the C_6H_7 radical ($A_p^m(C_6H_7) = 8.2$ MHz, Table 6.1).

As an additional check the spin populations, ρ_i (i=o, m, p, met), at ring carbon atoms were calculated using the McConnell relations (eq. 2.5) for the case of the ortho PEA-Mu radical. The ρ_{met} value of the ortho PEA-Mu radical was taken from the ab initio calculations (Figure 6.3):

$$\sum \rho_i \text{ (ortho PEA-Mu)} = 2\rho_o + 2\rho_m + \rho_p + \rho_{met} = \frac{(-2 * 25.5 \text{ MHz} + 2 * 6.8 \text{ MHz} - 36.2 \text{ MHz})}{Q_H^\alpha} - 0.11 = 1.03 \approx 1.0 \ , \quad (6.2)$$

where the proportionality factor value of $Q_H^\alpha = -64.46$ MHz is used, as recommended by Fischer.[108] The $\sum \rho_i$(ortho PEA-Mu) (i = o, p, m, met) is very close to 1 which again confirms the previous findings. The remaining resonances were assigned using the R parameter to the para PEA-Mu and ortho PEA-Mu β-methylene protons as in Figure 6.7. The splitting of the ortho PEA-Mu radical β-methylene proton resonance is caused by the presence of the chiral center at the position of its methylene carbon

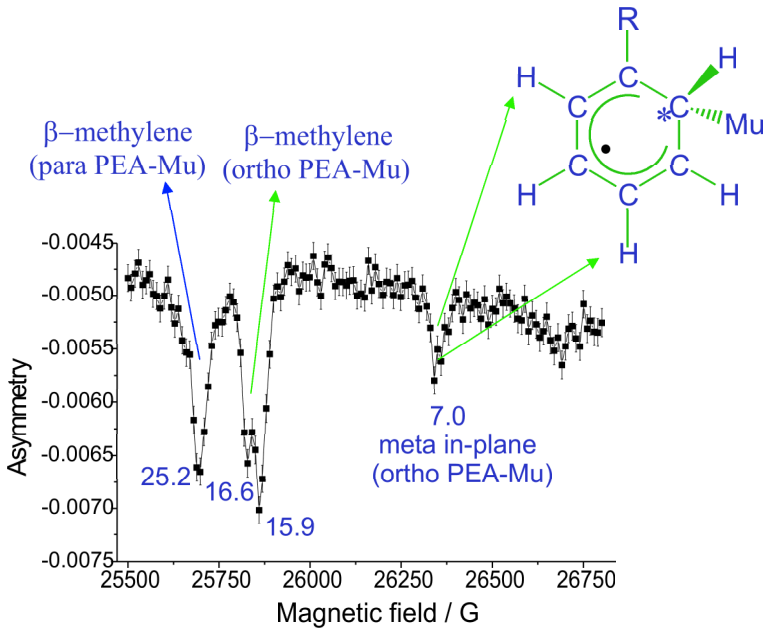

Figure 6.7: ALC spectrum of PEA-Mu radicals in D_2O at T=298 K and the assignment of corresponding resonances, lower fields. Hfcs values are denoted next and below the corresponding resonance. The belonging of the resonance to the PEA-Mu radical is denoted below the corresponding hfc value. The chiral methylene carbon center is marked with *. R denotes the -CH_2-CH_2-OH group.

atom (marked with * in Figure 6.7). The same effect was observed in other studies.[32]

It must be noted that the appearance of the meta PEA-Mu radicals' in-plane meta ring proton ALC resonance with small positive hfc (A_p^m(meta PEA-Mu) = 7.0 MHz, Figure 6.7), was somewhat surprising in view of its small value. This demonstrates the sensitivity of the ALC-μSR method for the purpose of these studies. Very similar spectra were also observed for PPA-Mu radicals (not shown here) and the assignment of resonances remains valid for these radicals since they have a similar structure.

One of the aims in this chapter was to try to detect the proton (from the hydroxyalkyl substituent group) hydrogen bonded to the π-electrons of the ring. The Δ_0 ALC resonance of this proton should disappear in the D_2O (in comparison to the spectrum in H_2O) because of the proton exchange on the OH group. As presented in Figures 6.7 and 6.5 the field range of 25000-30000 G was examined in D_2O, as well, but no differences with the measurements in H_2O were observed. This means that there is not enough of spin population at the position of this nuclues to be detected using the ALC-μSR technique under these conditions.

Table 6.2: A_{p}^{β} values of the PEA-Mu radicals in H_2O, D_2O and octadecane. Abbreviations as in List of abbreviations and symbols.

Environment, temperature	Ortho β-methylene A_{p}^{β} (mean) / MHz	Para β-methylene A_{p}^{β} / MHz
H_2O, $T = 298$ K	16.1	25.1
H_2O, $T = 349$ K	16.2	25.8
D_2O, $T = 298$ K	16.0	25.2
D_2O, $T = 349$ K	16.2	25.7
Octadecane, $T = 308$ K	15.9	24.3

Table 6.3: A_{p}^{β} values of the PPA-Mu radicals in octadecane and MeOH. Abbreviations as in List of abbreviations and symbols.

Environment, temperature	Ortho β-methylene A_{p}^{β} (mean) / MHz	Para β-methylene A_{p}^{β} / MHz
Octadecane, $T = 308$ K	16.9	26.2
Octadecane, $T = 349$ K	16.9	26.7
MeOH, $T = 312$ K	16.8	24.3

6.3.2 β-methylene proton hyperfine coupling constants

Representative ALC spectra of β-methylene protons of ortho and para PEA-Mu radicals are presented in Figures 6.4, 6.6 (left hand side) and 6.7. Summarised A_{p}^{β} for ortho and para PEA-Mu radicals in H_2O, D_2O and octadecane are listed in Table 6.2. They show overall very similar behaviour in H_2O and D_2O. The values in octadecane are slightly smaller. In general, A_{p}^{β} *increases with the temperature.* This is crucial information as it demonstrates that the preferred position of the substituent group is *eclipsed* to the p_z orbital at the C_α atom of the phenyl ring (Figure 2.2). In the case of the para PEA-Mu radical this effect is more pronounced than in the case of the ortho PEA-Mu radical.

A representative ALC spectrum of β-methylene protons belonging to ortho and para PPA-Mu radicals is presented in Figure 6.8. The summarised A_{p}^{β} of ortho and para PPA-Mu in octadecane and MeOH are listed in Table 6.3. A_{p}^{β} values are similar in both environments. The A_{p}^{β} of the para PPA-Mu radical increases with the temperature. But the situation is somewhat different for the ortho PPA-Mu radical. The A_{p}^{β} of the ortho PPA-Mu radical remains almost constant.

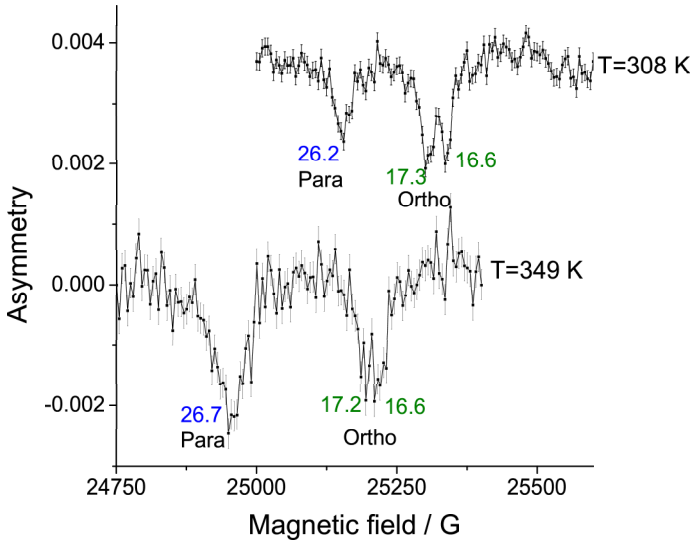

Figure 6.8: β-methylene proton ALC Δ_0 resonances of PPA-Mu radicals in octadecane. Para and ortho denote to which PPA-Mu radical the corresponding resonance belongs. The hfc value is given next to the corresponding resonance. Temperatures are denoted next to the corresponding spectrum. Abbreviations as in List of abbreviations and symbols.

Table 6.4: The energy difference between the conformations ($\Delta E = E_{\text{non-folded}} - E_{\text{folded}}$) of PEA-H radicals in the gas phase. Abbreviations as in List of abbreviations and symbols.

radical	ΔE / kJ mol^{-1}
Ortho PEA-H	4.8
Meta PEA-H	2.2
Para PEA-H	3.0

6.3.3 Ab initio calculations

6.3.3.1 Hydrogen adducts to 2-phenylethanol

The energy differences between the conformations (non-folded minus folded) of PEA-H radicals (instead of PEA-Mu) in the gas phase are listed in Table 6.4. It was found that the folded conformation of all PEA-Mu radicals is energetically favoured, with certain differences. The energy difference (non-folded minus folded) is the largest in the case of the ortho PEA-Mu radical and the smallest for the meta PEA-Mu radical.

The results of ab initio calculations (Figure 6.9) show that the mean $A_{\text{p}}^{\text{met}}$ value

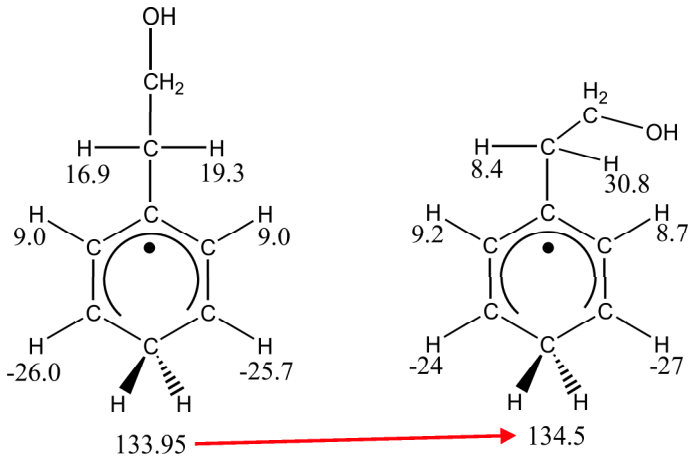

Figure 6.9: Hfcs of para PEA-H radical conformations (left - folded, right - non-folded) obtained from ab initio calculations. Note the increase of the mean $A_{\mathrm{p}}^{\mathrm{met}}$ value (marked with an arrow) when the conformation changes into folded. Abbreviations as in List of abbreviations and symbols.

increases for the folded conformation. This is very important information, since it corresponds to the discontinuous increase of $A_{\mathrm{p}}^{\mathrm{met}}$ observed in water containing solvents (Figure 6.2). In Figure 6.9 the mean $A_{\mathrm{p}}^{\mathrm{met}}$ values are displayed, since the methylene protons of the para PEA-Mu radical are inequivalent in the absence of the averaging motions (intramolecular vibrations, etc.).

In the case of hydrogen bonding with water molecules there are always two possible arrangements of interacting PEA-H and H_2O molecules, one where hydrogen bonding takes place between the oxygen from the hydroxyalkyl group of the PEA-H radicals (marked as $O_{\text{PEA-H}}$ in Table 6.5) and hydrogen from the water molecule (marked as H_{H_2O} in Table 6.5). The second possibility is when hydrogen bonding takes place between the hydrogen from the hydroxyalkyl group of the PEA-H radicals (marked as $H_{\text{PEA-H}}$ in Table 6.5) and the oxygen from the water (marked as O_{H_2O} in Table 6.5).

Both cases are specially examined for the para PEA-H-H_2O cluster, as shown in Figure 6.10. As can be seen from the energy differences (listed in Table 6.5) the hydrogen bonding is stronger in the case where hydrogen bonding takes place between the $H_{\text{PEA-H}}$ and O_{H_2O} (marked as $H_{\text{PEA-H}}$-O_{H_2O}in Table 6.5). Therefore this arrangement of molecules was examined for ortho, para and meta PEA-H-H_2O clusters, as well. The energy differences between the conformations (non-folded minus folded) of the PEA-H-H_2O cluster are listed in Table 6.5. As was the case with single molecules in the gas phase the energy difference between conformations (non-folded minus folded) is largest for the ortho PEA-H-H_2O cluster followed by a para PEA-H-H_2O cluster. The energy difference between the conformations (non-folded minus folded) increases when

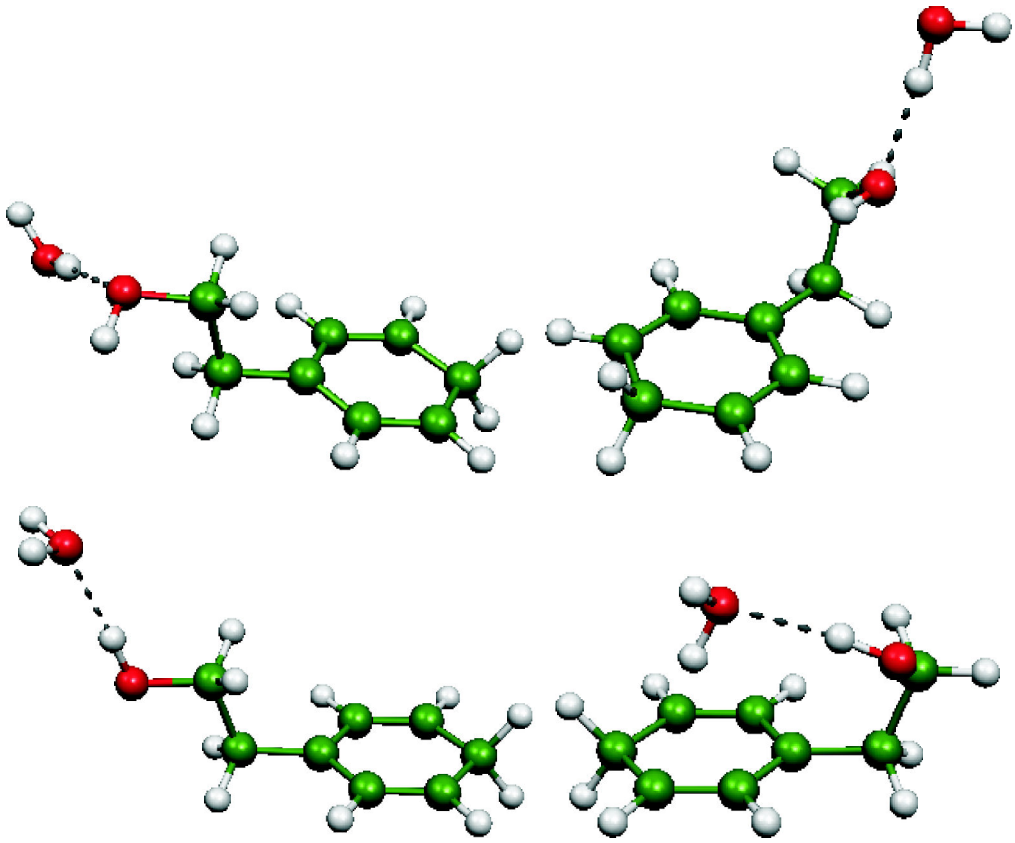

Figure 6.10: The folded and non-folded conformations of the para PEA-H-H_2O cluster, when hydrogen bonding is between the $O_{PEA\text{-}H}$ and H_{H_2O} (upper part of figure) and between the $H_{PEA\text{-}H}$ and O_{H_2O} (lower part of figure).

Table 6.5: The energy difference ($\Delta E = E_{\text{non-folded}} - E_{\text{folded}}$) between the conformations of PEA-H-H_2O clusters.

radical	ΔE / kJ mol^{-1}	hydrogen bonding between
Ortho	9.1	$H_{PEA\text{-}H}$-O_{H_2O}
Meta	5.3	$H_{PEA\text{-}H}$-O_{H_2O}
Para	3.1	$O_{PEA\text{-}H}$-H_{H_2O}
Para	6.6	$H_{PEA\text{-}H}$-O_{H_2O}

the H_2O molecule is introduced. The increase is largest for ortho and para PEA-H-H_2O clusters.

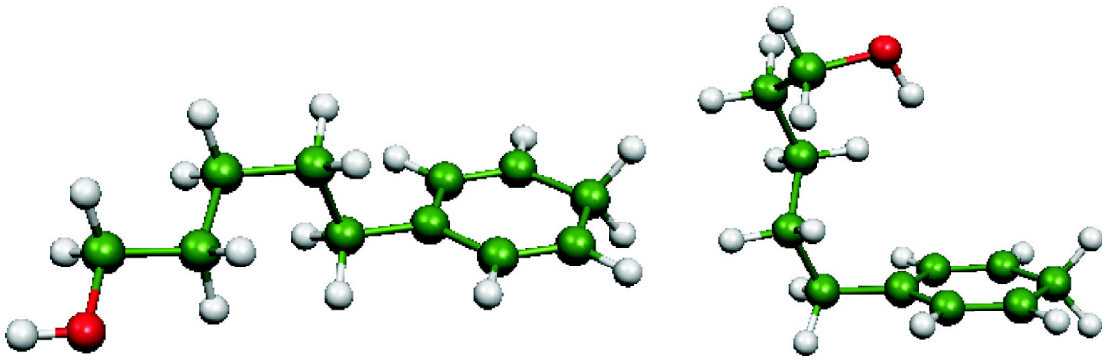

Figure 6.11: The folded and non-folded conformations of the para-PPA-H radical.

Table 6.6: The energy difference (non-folded minus folded) between the conformations of PPA-H radicals in the gas phase.

radical	ΔE / kJ mol^{-1}
Ortho PPA-H	-5.6
Meta PPA-H	-3.6
Para PPA-H	-1.5

6.3.3.2 Hydrogen adducts to 5-phenylpentanol

The energies of folded and non-folded conformations were examined for the case of PPA-H radicals (instead of PPA-Mu) in the gas phase (shown in Figure 6.11 for para PPA-H) and listed in Table 6.6. As can be seen in the case of PPA-H radicals energy needs to be invested in the process of hydrogen bonding between the H atom from the hydroxyalkyl group and the π-electron system from the phenyl ring. The energy difference is largest for the ortho PPA-H radical and smallest for the para PPA-H radical.

6.4 Discussion

6.4.1 β-methylene proton dynamics

The positive A_{p}^{β} temperature behaviour of all PEA-Mu radicals corresponds to the situation where the substituent group is *eclipsed* to the $\mathrm{p_z}$ orbital at the phenyl ring (at C_{α} atom in Figure 2.1). This position of the substituent group is a necessary condition for the intramolecular hydrogen bonding interaction.

Table 6.7: $\langle\cos^2\theta\rangle$ values of PEA-Mu radicals β-methylene protons in H_2O, D_2O and octadecane.

Environment, temperature	Ortho β-methylene $\langle\cos^2\theta\rangle$ *	Para β-methylene $\langle\cos^2\theta\rangle$
H_2O, $T = 298$ K	0.430	0.377
H_2O, $T = 349$ K	0.433	0.386
D_2O, $T = 298$ K	0.426	0.381
D_2O, $T = 349$ K	0.429	0.384
Octadecane, $T = 308$ K	0.421	0.371

* - $\langle\cos^2\theta\rangle$ value calculated from mean A_{p}^{β} (Table 6.2)

Table 6.8: $\langle\cos^2\theta\rangle$ values of the PPA-Mu radicals β-methylene protons in octadecane and MeOH.

Environment, temperature	Ortho β-methylene $\langle\cos^2\theta\rangle$ *	Para β-methylene $\langle\cos^2\theta\rangle$
Octadecane, $T = 308$ K	0.454	0.392
Octadecane, $T = 349$ K	0.452	0.398
MeOH, $T = 312$ K	0.448	0.389

* - $\langle\cos^2\theta\rangle$ value calculated from mean A_{p}^{β} (Table 6.3)

The averaged $\langle\cos^2\theta\rangle$ values of PEA-Mu radicals (listed in Table 6.7; θ defined in Figure 2.1) were obtained using the McConnell relation for β-methylene protons, and they are in all cases below the free rotation limit ($\langle\cos^2\theta\rangle_{(\text{free rot. limit})} = 1/2$). $\langle\cos^2\theta\rangle$ values are somewhat different for para and ortho PEA-Mu radicals. The most important reason why A_{p}^{β} (and corresponding $\langle\cos^2\theta\rangle$) of ortho PEA-Mu is less sensitive to the temperature change (dynamics of substituent group) than that of para PEA-Mu originates from the fact that the spin population at the ortho ring carbon atom (C^{o} in Figure 6.3) is smaller than that of the para ring carbon atom (C^{p} in Figure 6.3). The second reason is the difference in intramolecular hydrogen bonding energies between the ortho and para PEA-Mu radicals, as shown in Table 6.5. The same argumentation remains valid for the PPA-Mu radicals.

For ortho and para PPA-Mu radicals slightly increased $\langle\cos^2\theta\rangle$ values (compared to PEA-Mu radicals) were observed. In particular the A_{p}^{β} value of the ortho PPA-Mu remains almost constant at both temperatures in octadecane. However, the calculated $\langle\cos^2\theta\rangle$ values are in both cases below 1/2, thus suggesting that the motion of the β-methylene group is not at the free rotation limit. This indicates that the substituent

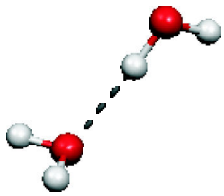

Figure 6.12: Hydrogen bonding of two H_2O molecules.

group of the PPA-Mu radicals spends more time *eclipsed* to the p_z orbital at the phenyl ring (at C_α atom in Figure 2.1).

6.4.2 Hydrogen bonding

For the sake of comparison, using the same method and basis set the hydrogen bonding energy of two water molecules (Figure 6.12) was calculated to be 24.4 kJ mol^{-1}. This is in agreement with results of other studies.[109] When compared with the H_2O-H_2O hydrogen bonding energy, the intramolecular hydrogen bonding energy of PEA-H radicals is much weaker, but not negligible.

It is found that the intramolecular hydrogen bonding contributes to the stabilisation of the folded conformation of all PEA-H radicals in the gas phase. This effect is even more pronounced after the explicit introduction of H_2O molecules. As seen from ab initio calculations of PEA-H-H_2O clusters, the presence of water stabilises the intramolecular hydrogen bonding interaction. This corresponds qualitatively to the results of PEA molecule conformational studies.[105,106]

As shown in Figure 6.9 the folding caused by the intramolecular hydrogen bonding increases the A_p^{met} and it corresponds to the discontinuous increase of A_p^{met} observed in water containing solvents (Figure 6.2).

The presence of the explicitly introduced H_2O molecule affects the Single Occupied Molecular Orbital (SOMO) according to the results of ab initio calculations, as well. The SOMO orbital of the para PEA-H radical has an eigenvalue of $E_{SOMO}^{non-folded} = -4.59$ eV and $E_{SOMO}^{folded} = -4.67$ eV in the gas phase for the non-folded and folded conformation respectively, which may be considered similar. But the eigenvalue of this orbital in the para PEA-Mu-H_2O cluster is significantly changed for the non-folded conformation. In the case of the non-folded conformation the SOMO eigenvalue is increased to $E_{SOMO}^{non-folded} = -4.33$ eV (increase of 5%), whereas it remains very similar for folded conformation ($E_{SOMO}^{folded} = -4.71$ eV).

The SOMO orbital is the key orbital in free radical reactions. This demonstrates

how different conformations of cyclohexadienyl type radicals in various solvents may play a role in a chemical reaction through the influence on the SOMO orbital. This result may be of interest in chemical reactions where cyclohexadienyl type radicals are involved.[110,111]

In the case of PPA-Mu radicals the preferred position of the substituent group is *eclipsed* to the p_z orbital of the ring, which is a necessary condition for the intramolecular hydrogen bonding. However the intramolecular hydrogen bonding interaction may be considered to be of negligible importance as shown by the results of ab initio calculations. This is in agreement with the previous finding that the influence of the substituent group on the π-electron system decreases with its increased length (Chapter 5).

6.4.3 Comparison between the cyclohexadienyl type radicals

Most of the spin density of the cyclohexadienyl type radicals is in the SOMO orbital, with a small amount being in other orbitals.[46] The spin population on the para ring carbon atom to which the substituent group is bonded (C_p carbon atom in Figure 6.3) is largest in the case of the para PEA-Mu radical, as shown in Figure 6.3. Due to this reason the conformational change caused by the hydrogen bonding has the largest influence on the A_p^{met} of the para PEA-Mu radical indirectly via the influence on the SOMO orbital.

This effect does not play a significant role in the case of the para PPA-Mu radical because it has a much larger substituent group thus making the intramolecular hydrogen bonding interaction not very probable.

6.5 Conclusions

ALC-μSR resonances of in-plane and of β-methylene protons of PEA-Mu and PPA-Mu radicals were identified and assigned here for the first time. The same assignment remains valid for every structurally similar type of radical.

In this chapter, it was demonstrated that ALC-μSR may be used as a tool for monitoring the conformational differences of cyclohexadienyl type radicals in environments of different polarities. The experimental analysis shows whether the preferred conformation of the substituent group is eclipsed or staggered with the p_z orbital at the phenyl ring. But to obtain an information whether the hydroxyalkyl substituent

group interacts with the π-electrons of the phenyl ring the experimental analysis was not sufficient, and therefore the ab initio calculations were employed.

Special attention was on the A_{p}^{β} of PEA-Mu radicals. From the positive temperature behaviour of their A_{p}^{β} the preferred conformation is found to be, when the substituent group is eclipsed with the $\mathrm{p_z}$ orbital at the phenyl ring, both in water and in octadecane. Ab initio calculations of ortho, para and meta PEA-H radicals (instead of PEA-Mu) in the gas phase show that the folded conformation is more stable. Ab initio calculations of ortho, para and meta PEA-H-$\mathrm{H_2O}$ clusters show the same result as well. From these results, it may be concluded that water stabilises the folded conformation in the case of all PEA-Mu radicals.

The influence of the conformation on the SOMO orbital and therefore on the radicals' hfcs is the largest in the case of the para PEA-Mu radical. It is shown here, that the discontinuous increase of % *aq.char.* (and corresponding $A_{\mathrm{p}}^{\mathrm{met}}$) of the para PEA-Mu radical in the water containing solvents (observed in Chapter 5) originates in the folding of the substituent group caused by the increased intramolecular hydrogen bonding.

The behaviour of PPA-Mu radicals' A_{p}^{β} in MeOH and octadecane shows that the substituent group spends more time eclipsed with the $\mathrm{p_z}$ orbital at the phenyl ring. Ab initio calculations in the case of ortho, para and meta PPA-H radicals in the gas phase show that the non-folded conformation is more stable. This means that intramolecular hydrogen bonding is of less significance in the case of PPA-Mu radicals.

7 Ferroelectricity of pyridinium perchlorate

7.1 General remarks

The majority of pyridinium salts are not ferroelectric and they undergo a single order-disorder phase transition.[112,113] Ferroelectric salts in this family undergo a sequence of two phase transitions, as shown in Figure 7.1. The first phase transition is of order-disorder type and the salt changes from para- to ferroelectric. The second phase transition takes place in the ferroelectric phase and is also of order-disorder type. Some of pyridinium salts undergo an additional third phase transition within the ferroelectric phase. In this sequence of phase transitions they start from the disordered high temperature phase (Figure 7.2, left hand side) and end up in fully orientationally ordered low temperature phase (Figure 7.2, right hand side). $PyClO_4$ is a multidirectional ferroelectric salt with a first order paraelectric-ferroelectric phase transition at 248 K. A further phase transition that takes place at 233 K is also of first order. The compound remains ferroelectric on further cooling. The detailed structure is available only for the high temperature phase and was described by Czarnecki et al.[114] The symmetry of the high temperature phase is R3m. The elementary cell is near cubic with coplanar pyridinium molecules at each corner and a perchlorate anion in the center as shown in Figure 7.3. The body diagonal perpendicular to the cation plane is a three-fold axis. In the intermediate phase the crystal structure undergoes a subtle change, and the symmetry reduces to Cm. The low temperature phase is believed to either remain Cm or to change to Pm.[114] $PyClO_4$ is isostructural at room temperature with pyridinium iodide which does not show ferroelectric properties.[112] The pyridinium ion is of C_{2v}

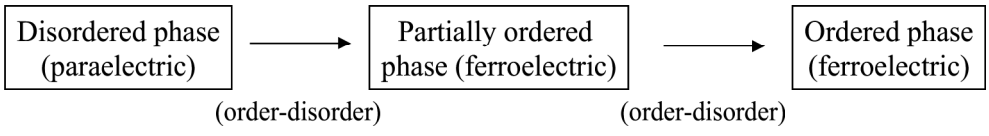

Figure 7.1: Phase transition sequence of ferroelectric pyridinium salts.

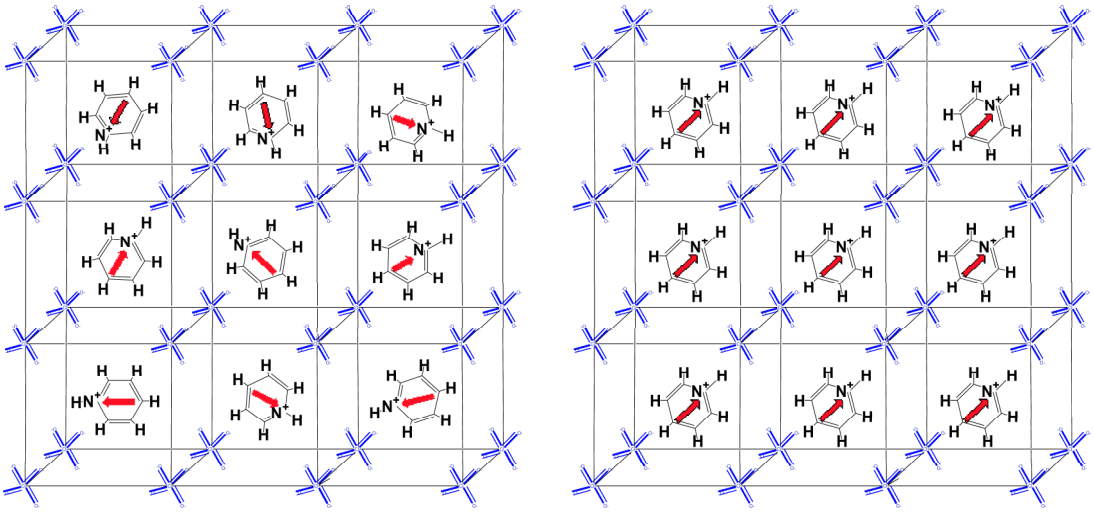

Figure 7.2: Left: completely disordered pyridinium cations, situation in the high temperature nonferroelectric phase, right: completely ordered cations, situation in the low ferroelectric temperature phase. The arrow points in the direction of the pyridinium cation dipole moment.

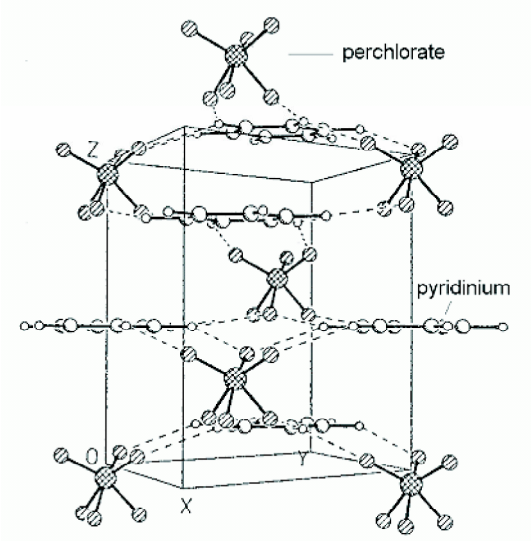

Figure 7.3: Crystal structure of the $PyClO_4$ high temperature phase.[114]

symmetry, but due to the fact that carbon and nitrogen positions are not resolvable in X-ray analysis and that the C-N and C-C bond lengths are as well the same within experimental error,[114] its structure is akin to that of benzene, and a pseudo-C_6 axis can be assumed. The perchlorate anion is strongly disordered at room temperature, and the positions of the oxygen atoms are not resolvable.[114] Its structure in this crystal is therefore not exactly known, however it is tetrahedral in vacuum and most likely also in the high temperature phase. The possibility of distortion from tetrahedral symmetry

in the intermediate and low temperature phase will be discussed further as one of the possible reasons for the appearance of ferroelectricity. In this chapter it is verified that pyridinium cations rotate about the pseudo C_6 axis of the pyridinium cation ring. The intention in this chapter is to correlate the alignment of the cation permanent dipole moments with the observed macroscopic ferroelectricity and to discuss possible reasons for the appearance of ferroelectric polarization.

The normalized NMR derived results are compared by using the "% relative polarization" (as described in section 3.3.2) with the normalized data from pyroeffect measurements in the direction *parallel* to the threefold axis of the high temperature phase.[67] The appearance of a polarization in this direction is explained with flipping of the cations by 90° when a single crystal is pulled into the single ferroelectric domain during the course of the experiment. The flipping of cations would not change the symmetry group of the crystal.

7.2 Results

7.2.1 Calorimetric measurements

From the DSC measurements shown in Figure 7.4, the phase transition enthalpies at 248 K and 233 K are determined to be $\Delta H_1 = 4.3$ kJ mol^{-1}, $\Delta H_2 = 0.8$ kJ mol^{-1}, respectively. The very small peak between the phase transitions was not studied particularly since it showed a near-negligible heat effect (also noticed previously)[67] and did not lead to any observable effects in the NMR spectra.

7.2.2 NMR experiments

7.2.2.1 Quadrupole echo experiments

In Figure 7.5, representative quadrupole echo ^{2}H NMR spectra of deuterated pyridinium cation are given along with the corresponding simulations. The phase transitions at 248 K and 233 K have a great influence on the ^{2}H NMR line shapes. In the high temperature phase, axially symmetric line shapes are detected. The splittings between the inner singularities in the low, intermediate and high temperature phase, here denoted as Δ_1, Δ_2 and Δ_3, respectively, are given in Table 7.1. In the high-temperature phase the observed splitting is compatible with a highly symmetric, fast uniaxial rotational jump process about an axis perpendicular to the molecular plane, and the

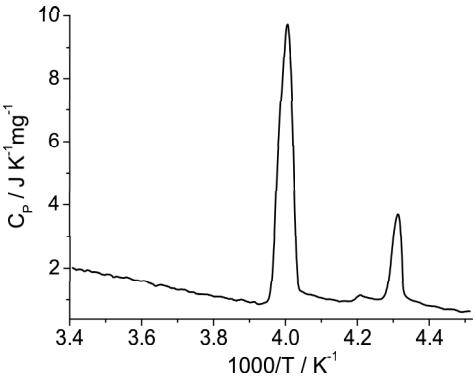

Figure 7.4: DSC measurements for $PyClO_4$-d_5 at a heating rate of 5 K min^{-1}. $\Delta H_1 = 4.3$ kJ mol^{-1} and $\Delta H_2 = 0.8$ kJ mol^{-1} for the paraelectric-ferroelectric and the other solid-solid phase transition, respectively.

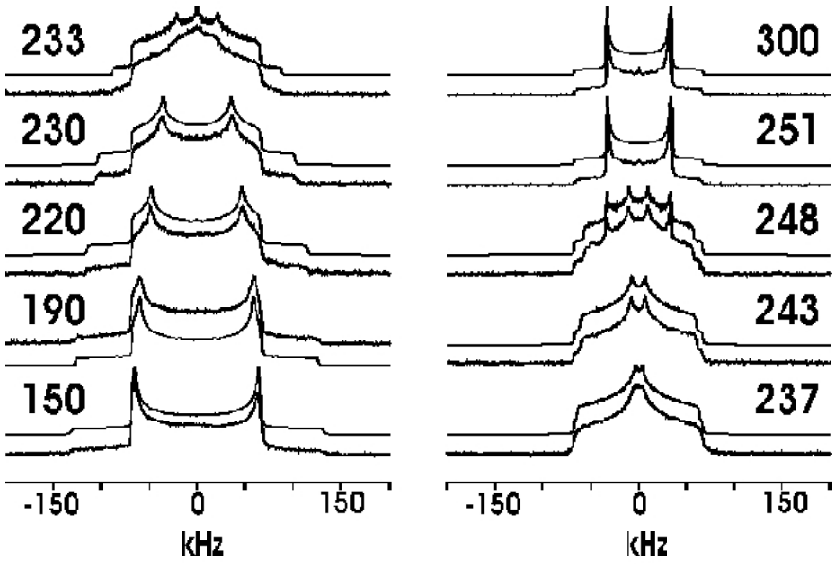

Figure 7.5: Experimental (lower) and simulated (upper, vertically displaced) ^{2}H NMR quadrupole echo spectra at selected temperatures. Temperatures in K are given above the corresponding spectra. Note the spectral superposition at the phase transition temperatures of 248 K and 233 K.

splitting does not depend significantly on temperature. However, in the intermediate- and low-temperature phases the splitting varies considerably with temperature. Here, typical non-axially symmetric ^{2}H NMR spectra are observed reflecting the presence of hindered overall motions of lower symmetry. At the lowest temperature, again, an almost axially symmetric ^{2}H NMR spectrum with a splitting characteristic for the

Table 7.1: Experimental splittings between singularities obtained both from quadrupole echo and partial recovery spectra with longest delay.

T / K	$\Delta 1$ / Hz	$\Delta 2$ / Hz	$\Delta 3$ / Hz
140	128688		
150	128508		
160	125890		
170	124299		
180	122881		
190	118736		
200	112653		
210	107574		
220	95351		
230	71377		
233	42508	0	
237		7184	
239		10206	
241		14195	
243		14753	
245		15982	
245		18149	
248		20409	66552
251			66226
260			66030
270			65981
290			65710
300			66030

rigid limit case is observed. Variable-temperature ^{2}H NMR spectra recorded for the N-deuterated pyridinium perchlorate (spectra not shown here) gave identical spectra, confirming that there is no other motion except the one about the pseudo C_6 axis. A coexistence of two phases is clearly observed in the spectra at both phase transition temperatures, as expected for first order transitions. The temperature dependence of the p_1, p_2, p_3 and p_4 values (defined in Figures 3.1 and 3.2) is given in Figure 7.6. In the high-temperature phase, the p_1 population amounts to 0.1667, demonstrating six equally populated orientations, while in the intermediate- and low-temperature phase p_1 increases at the cost of p_2, p_3, and p_4, indicating that the degeneracy of the six orientations is lifted. At both phase transitions, a discontinuous change of p_1 is observed, indicating again that they are of first order.

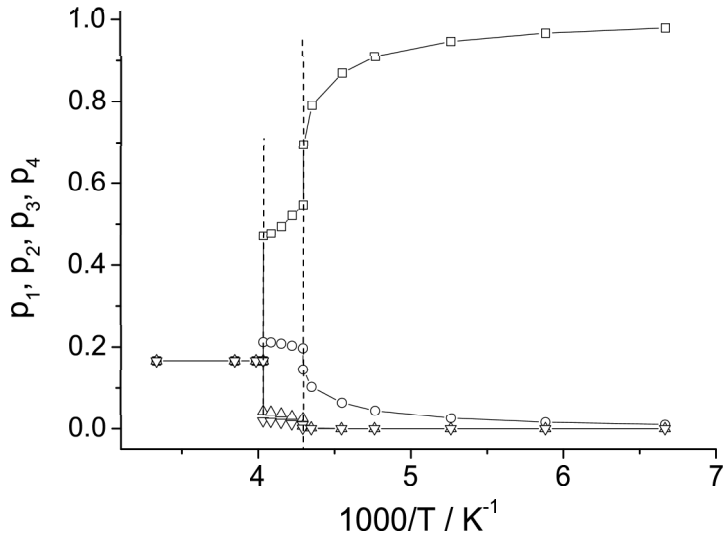

Figure 7.6: Temperature dependence of the populations p_1 (□), p_2 (○), p_3 (△) and p_4 (▽). Vertical lines represent the phase transition temperatures.

7.2.2.2 Inversion recovery experiments

Selected experimental partially relaxed ^{2}H NMR spectra from the inversion recovery experiment along with the corresponding simulations are given in Figure 7.7. Simulations on the basis of the six-site jump model match the experimental spectra quite well at 255 K with small differences at intermediate delay times at the lowest temperatures. The corresponding experimental and simulation-based T_{1Z} values are displayed in Figure 7.8. The two sets of data mostly agree within error.

7.2.3 Ferroelectric polarization

The macroscopic ferroelectricity is calculated based on eq. 3.11 and then presented in % *relative polarization* unit (Figure 7.9). The populations are derived from the ^{2}H NMR data analysis, and the unit cell volume as a function of temperature was determined in dilatometric measurements by Szafraniak et al.[67] The number of ion pairs in the unit cell remains three in all phases. In the low-temperature phase range, the agreement between the results obtained on the basis of the NMR data analysis and those from pyroeffect measurements is nearly perfect because of the intentional matching of the low-temperature end of curves. Small deviations may be attributed to experimental imperfections. In contrast, in the *intermediate-temperature* phase, the deviations are

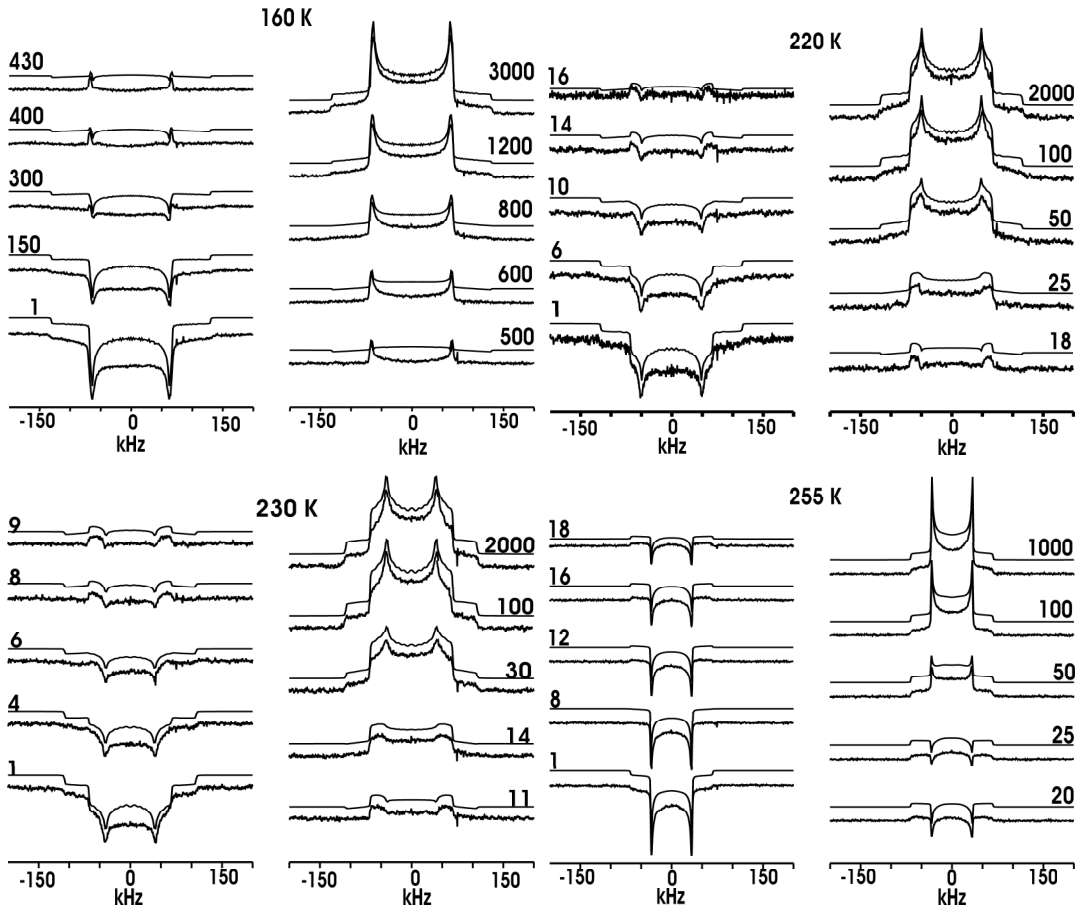

Figure 7.7: Experimental (lower) and simulated (upper, vertically displaced) partially relaxed ^{2}H NMR spectra (inversion recovery experiment) at selected temperatures with relaxation delays τ_r in milliseconds.

too high to be explained by experimental errors. Obviously, there must be an additional mechanism that contributes to ferroelectricity.

7.3 Discussion

7.3.1 Ferroelectric polarization and sublattice displacement

Possible candidates for the difference between the macroscopic ferroelectric polarizations and the ones derived from NMR (Figure 7.9), which will be discussed in the following, are: (i) the cation-anion sublattice displacement, as suggested earlier for $PyBF_4$,[65] (ii) a displacement of the cation center of charge out of the cation center of mass when the cation rotation slows down, and (iii) the presence of a dipole moment of the anion when it is distorted from tetrahedral symmetry.

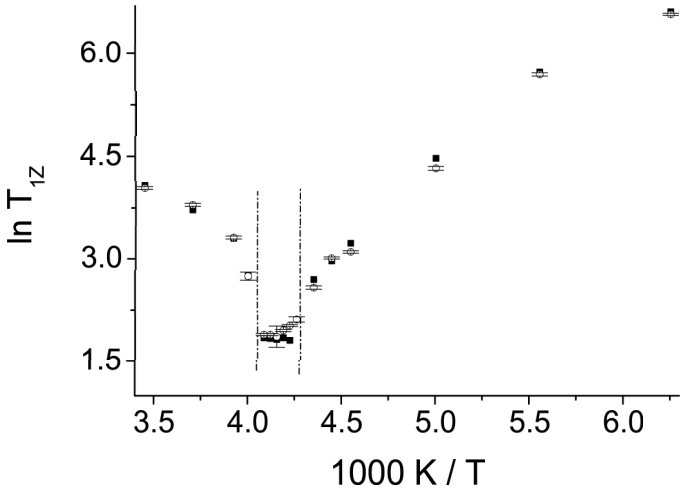

Figure 7.8: Experimental (open circles with error bars) and simulation based (solid squares) T_{1Z} relaxation times. The vertical lines represent the phase transition temperatures.

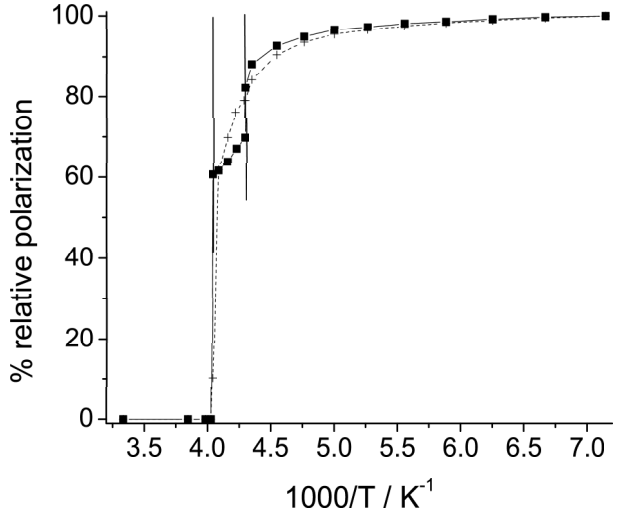

Figure 7.9: Relative polarization from pyroeffect measurements in the direction parallel to the threefold axis (crosses) and derived from NMR populations (squares). Vertical lines represent the phase transition temperatures.

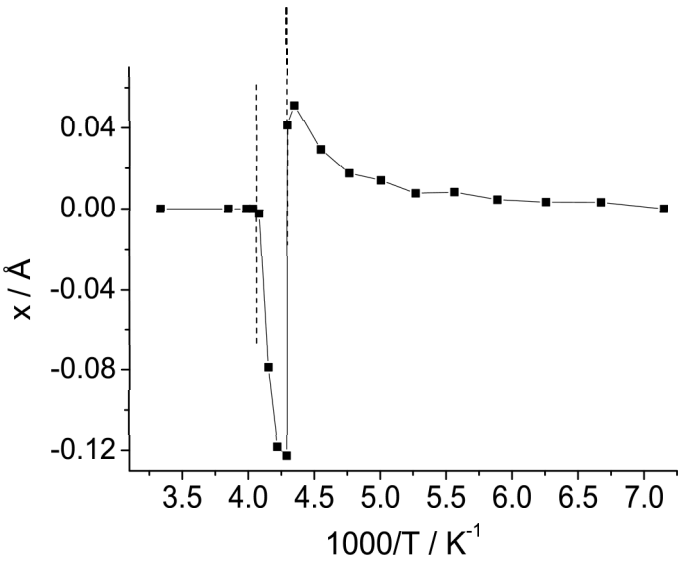

Figure 7.10: Sublattices displacement calculated from the difference of NMR (using a dipole moment value of 1.97 D) and pyroeffect data. Vertical lines represent the phase transition temperatures.

(i) If sublattice displacement takes place, then values of up to -0.12 Å in the intermediate-temperature (positive contribution to the macroscopic polarization) and of up to +0.04 Å in the low-temperature phase, as displayed in Figure 7.10 are required to explain the difference between macroscopic and NMR-derived ferroelectric polarization (as described in section 3.3.2, eq. 3.12).

(ii) Another possible contribution to the ferroelectric polarization in the intermediate-temperature phase may arise from the fact that the center of charge of the pyridinium ion is at a slightly different position than the center of mass. This effect may be important when the rotational jump process is slowed down in the intermediate and especially in the low-temperature phase. In this respect, $PyClO_4$ should be similar to $PyBF_4$, where this contribution to the ferroelectric polarization was found to be less than 2%.[65]

(iii) The comparison between all pyridinium salts reveals that the ferroelectric ones have anions with tetrahedral structure in vacuum ($PyClO_4$,[114] $PyBF_4$,[65] $PyIO_4$,[69,115] $PyReO_4$[116]) or are of pseudo-tetrahedral symmetry ($PyFCrO_3$,[38] $PyFSO_3$[117]), while others - like PyI,[113] PyBr,[113] $PyPF_6$[118] - are not ferroelectric. In the crystal the tetrahedral symmetry of the free anion can be lowered towards C_{3v} or D_{2d}. Lowering towards C_{3v} would create a dipole moment. Distortion from tetrahe-

dral symmetry in the crystal lattice has been observed in a neutron diffraction study of $PyIO_4$ resulting in a dipole moment of 0.27 D,[115] and for guanidinium perchlorate where one of the bonds was found to be stretched by 0.05 Å.[119] If the same distortion would take place for $PyClO_4$, then the dipole moment of the anion would contribute significantly to the polarization both in the intermediate- and in the low-temperature phases. Unfortunately, it is not known whether there is such a distortion in the ferroelectric phases. Furthermore, the X-ray structure studies in the high temperature phase have shown no significant deviation from tetrahedral symmetry and rotational disorder.[114]

It is therefore concluded that the cation-anion sublattices´ relative displacement is the most likely explanation for the difference, shown in Figure 7.9, between the macroscopic and the NMR data sets in the intermediate temperature phase. In contrast to the case of $PyBF_4$[65] this displacement gives a positive contribution to the macroscopically observed polarization and builds up crystal strain as well. Figure 7.10 shows that this strain is released again at the second phase transition at 233 K.

The ratios of the NMR-derived results at the para-to-ferroelectric phase transition temperature and at the lowest temperature match almost quantitatively the ratio of the experimentally measured results, once again confirming that ferroelectricity in this ferroelectric salt is of order-disorder type.

For a test, eq. 3.11 can also be used for the calculation of the absolute values of the experimentally measured polarization for the case of $PyIO_4$, assuming full ordering of all cations ($p_1 = 1$), neglecting the fact that they are tilted with respect to the ferroelectric axis. After introducing the other constants ($Z = 4$, $V = 751$ Å^3, $\mu = 1.97$ D)[69] into eq. 3.11, a spontaneous polarization of 3.45 μC cm^{-2} is obtained, somewhat less than reported experimental value at the lowest temperature $T = 120$ K of 3.95 μC cm^{-2},[69] despite the neglected tilt. While this confirms that the present model can predict *absolute* polarizations, it also means that an additional mechanism contributes to the polarization of $PyIO_4$. Values of the spontaneous polarization in cases of other types of ferroelectric salts similar to the value calculated with the help of eq. 3.11 may be understood as indication of the of the order-disorder type of ferroelectricism.

7.3.2 Heat effects

Comparison of the enthalpies derived from the NMR measurements (eq. 3.10) with those measured by DSC shows a difference of approximately 10%, depending on the actual sample temperature as shown in Figure 7.11. The integrated enthalpy changes

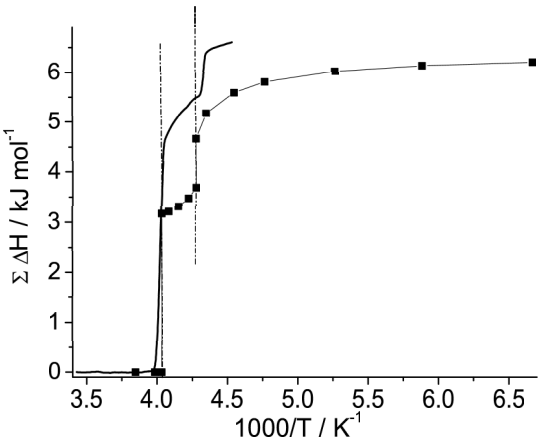

Figure 7.11: Total change of enthalpy from NMR data (■) and DSC measurements (full line). The two data sets are matched in the high-temperature phase. Vertical lines represent the phase transition temperatures.

measured by DSC depend somewhat on the choice of baseline and the range of measurements. However, even here, exactly the same trend in the change of the calorimetric and the NMR-derived integrated enthalpy is observed, implying that the model used here is appropriate. This means that most of the energy released during cooling originates from the ordering of pyridinium cations. The difference between the two curves corresponds to the heat released by other possible processes (ordering of anions, structural change, etc.). The enthalpy change of the higher temperature phase transition measured by DSC is higher by about 44% than the one calculated from the NMR measurements, suggesting that a significant portion of the energy is released in other processes, probably during spring loading the lattice as in $PyBF_4$.[65] At the low temperature phase transition, the difference is approximately 9%. In this case, the structural change is of minor importance, and the released energy arises almost completely from the ordering of the pyridinium cations.

7.3.3 Dynamic properties

The motional correlation time τ_c for the pyridinium rotations derived from inversion recovery experiments is plotted against the inverse temperature in Figure 7.12. They clearly follow Arrhenius behaviour in all three phases. The apparent activation energies for the high-, intermediate- and low-temperature phases amount to 13.5 kJ mol^{-1}, 7.4 kJ mol^{-1}, and 6.4 kJ mol^{-1}, respectively. The values for the high-temperature phase are lower than those reported for pyridinium iodide, pyridinium tetrafluorobo-

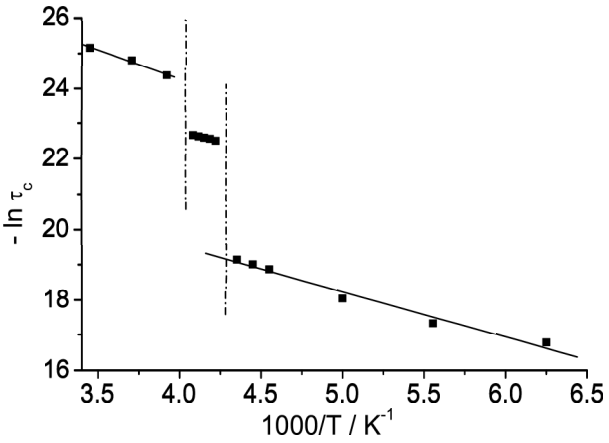

Figure 7.12: Arrhenius plot of the correlation time τ_c derived from simulations of the T_{1Z} relaxation data. Vertical lines represent the phase transition temperatures.

rate and pure solid benzene.[65,112,119,120] The corresponding preexponential factors are 2.32×10^{13} s^{-1}, 6.96×10^{11} s^{-1}, and 5.3×10^{10} s^{-1} for the high-, intermediate- and low-temperature phases, respectively. To judge these values, the preexponential factor is estimated assuming that it is the attempt frequency to cross the energy barrier in the forward or backward direction, which is given by twice the frequency of the cations´ librational oscillation frequency. The harmonic force constant for the oscillating motion is then given by the second derivative at the potential minimum (eq. 7.1):

$$\frac{\mathrm{d}^2U}{\mathrm{d}\Psi^2} = -\frac{U_1^0}{2}\sin(\Psi - \frac{\pi}{2}) - 18U_6^0\sin(6\Psi - \frac{\pi}{2}) \; . \tag{7.1}$$

In the high-temperature phase, rotational jumps occur between degenerate 6-fold potential wells, the 1-fold potential being zero (eq. 3.9), and this gives the force constant value of $k = 18V_6^0 = 243$ kJ mol^{-1}. Thus the frequency of the cation librational motion with moment of inertia I amounts to

$$v = \sqrt{\frac{k}{4\pi^2 I}} = 0.93 \times 10^{12} \text{ s}^{-1} \tag{7.2}$$

or 62.24 cm^{-1}.

This translates into an attempt frequency of 1.87×10^{12} s^{-1} in the ground state and 1.25×10^{13} s^{-1} in the Boltzmann average at 298 K, which is in near quantitative agreement with the observed Arrhenius preexponential factor. The remaining factor of 1.8 may be due to the fact that the actual potential is of a cosine rather than

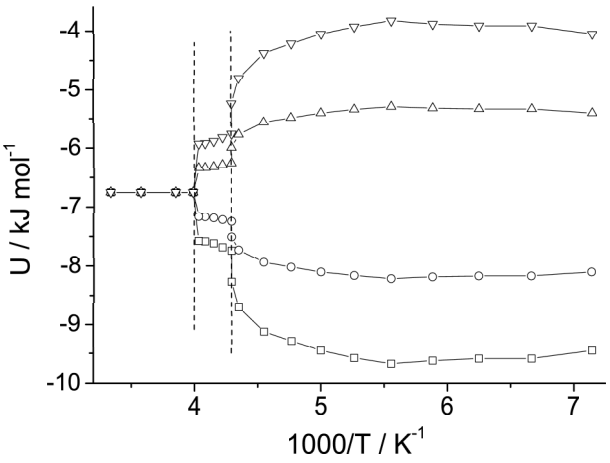

Figure 7.13: Potential vs. temperature ($\Psi = 0°$ - $\square$, $\Psi = \pm 60°$ - $\circ$, $\Psi = \pm 120°$ - $\triangle$ and $\Psi = \pm 180°$ - $\bigtriangledown$). Vertical lines represent the phase transition temperatures.

the assumed parabolic (harmonic) shape. The vibrational frequency has not yet been measured for this compound.

Because the crystal is more densely packed at lower temperatures, it seems unreasonable that the activation energies are lower for the intermediate- and low-temperature phases. Furthermore, the preexponential factor is expected to stay roughly constant. The discrepancy between expectation and observation suggests the presence of additional process that affects the apparent Arrhenius parameters. An increasing 1-fold potential, arising from the build up of ferroelectricity with decreasing temperatures, seems a very plausible origin of this unreasonable behaviour.

From the Arrhenius plot of the high temperature phase, the 6-fold part of the potential (U_6^0) is determined using eq. 3.9. In order to theoretically calculate the potential dependence at other temperatures, the U_6^0 is assumed to remain constant over the whole temperature range and with use of the U_1^0 potentials from the simulations of the NMR spectra the U for every orientation was calculated. As seen in Figure 7.13 the potential changes with the temperature and the degeneracy is lifted because of the 1-fold potential. With respect to the distribution of populations (Figure 7.6), it means that not all of the cations feel the same potential. The potential felt by the cation further influences the force constant, the relaxation, etc. The force constant for the intermediate and the low temperature phase is calculated using eq. 7.1. As it can be seen in Figure 7.14, the force constant is not changing significantly with the temperature and therefore it may be assumed that the preexpenential factor of the high

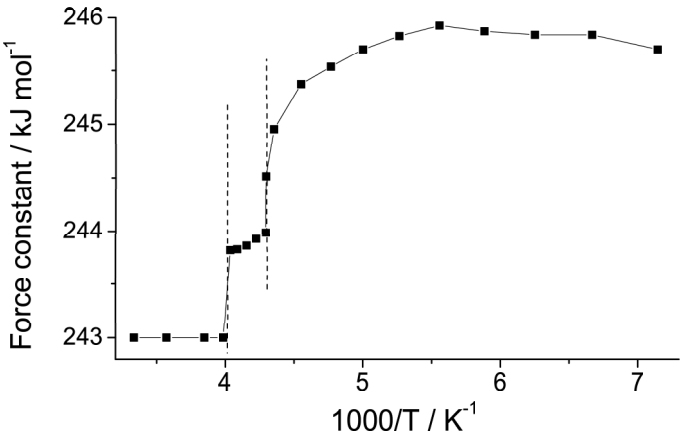

Figure 7.14: Force constant vs. inverse temperature. Vertical lines represent the phase transition temperatures.

temperature phase remains the same. However, it is important to mention that in the low and intermediate temperature phase the structure is somewhat different and that as well influences the activation energies. In the outcome all of this makes the activation energy obtained from the Arrhenius plot in the intermediate and the low temperature phase not entirely reliable. Due to all of this the activation energies are calculated by assuming that the preexponential factor remains constant. In the following, the values of the effective activation energies from the experimentally measured correlation times were calculated using eqs. 7.3 and 7.4:

$$\tau = \tau_c e^{\frac{\Delta E}{RT}} \tag{7.3}$$

or

$$\Delta E = RT(\ln \tau_c - \ln \tau) \ . \tag{7.4}$$

In eq. 7.4 value of $\ln \tau_c$ from the high temperature phase is introduced and the following results were obtained. To a first order the behaviour is as expected. The calculated activation energies show now the expected *increase* to ca. 16 and 22 kJ mol^{-1} over the two phase transitions toward the lower temperatures, but within the intermediate- and lower-temperature phases, the activation energies still decrease slightly with decreasing temperature. The activation energies were calculated as the mean of all values from Figure 7.15 for each phase separately. However, within the intermediate- and lower-temperature phases, the activation energies still decrease slightly with decreasing temperature. Constant or moderately increasing activation energies would require

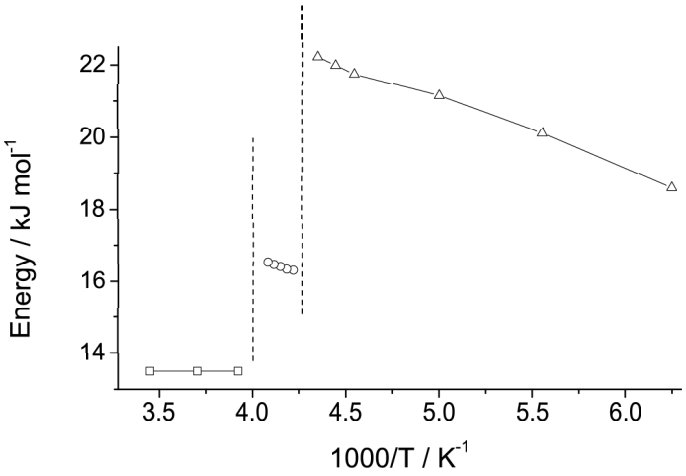

Figure 7.15: Activation energies vs. inverse temperatures (△ - high temperature phase, ○ - intermediate temperature phase, □ - low temperature phase). Vertical lines represent the phase transition temperatures.

increasing preexponential factors with decreasing temperature, which may be possible when the effect of the increase of V_1 is larger than that of the decreasing Boltzmann term.

7.4 Conclusions

The ^{2}H NMR data (quadrupole echo and inversion recovery experiments) of $PyClO_4$ can be quantitatively reproduced on the basis of a rotational jump motion of the pyridinium cations about their pseudo-C_6 axes. The high-temperature phase above 248 K is fully disordered, and the pyridinium cations undergo fast jumps between equally populated sites. In the intermediate- and low-temperature phases, motion occurs between unequally populated sites and results in domains of almost completely static and fully aligned cations near 140 K. The intermediate-temperature phase can still be considered as disordered, but the reorientation of the pyridinium cations occurs in a way that the average dipole moment along the ferroelectric axis is nonzero, giving rise to temperature-dependent domain polarization. Sublattice displacement gives an additional small positive contribution to the macroscopically observed polarization in this phase. Heat released during cooling originates mainly from the ordering of cation dipole moments. The difference between the heat released at the phase transitions and the heat necessary for ordering of the cations, appearing mainly at the higher phase

transition, is attributed to other possible processes such as spring-loading the lattice or anion ordering.

8 Comparison of ferroelectric and nonferroelectric pyridinium salts

8.1 General remarks

In the family of ferroelectric pyridinium salts, the "carriers" of the ferroelectricity are the pyridinium cation electric dipole moments, but the "governors" of the phase transition temperatures are the anions, since the cations are always the same.

Unit cell of the ionic crystal is composed of empty space (ES), and the Z anions and cations with the corresponding volumes V_{Anion} and V_{Cation}, as in eq. 8.1:

$$V_{\mathrm{Cell}} = Z_{\mathrm{Cation}} V_{\mathrm{Cation}} + Z_{\mathrm{Anion}} V_{\mathrm{Anion}} + ES \ . \tag{8.1}$$

The unit cell volume divided by the number of ions Z (specific unit cell volume) for the case of pyridinium salts gives (as long as $Z_{\mathrm{Cation}} = Z_{\mathrm{Anion}}$):

$$\frac{V_{\mathrm{Cell}}}{Z} = V_{\mathrm{Pyr}} + V_{\mathrm{Anion}} + \frac{ES}{Z} \ , \tag{8.2}$$

abbreviated as

$$\frac{V_{\mathrm{Cell}}}{Z} = V_{\mathrm{Anion}} + const. \tag{8.3}$$

within the assumption that ES/Z remains of similar value in this family of salts.

Eq. 8.3 shows that the specific unit cell volume is mainly dependent on the anion volume. Therefore, in this chapter the properties of anions in this family of pyridinium salts were correlated with specific unit cell volumes.

Table 8.1: Properties of the anions derived from ab initio calculations.

Anion	Ordering temperature / K	α* / $10^{-30}\,m^{-3}$	Dipole moment / D	Atom-atom pair	Bond lengths / Å	Partial atomic charges / e
BF_4^-	240 (fe)	3.05557	/	B-F	1.4173	B (+1.066) F (-0.516)
ClO_4^-	248 (fe)	5.59397	/	Cl-O	1.5006	Cl (+0.235) O (-0.309)
FSO_3^-	282 (fe)	5.12571	0.3713	S-F	1.5290 **	S (+0.558) F (-0.332) O (-0.409)
$FCrO_3^-$	258 (fe)	6.00148	0.1889	Cr-O	1.6500 **	O (-0.499) F (-0.546) Cr (+0.042)
ReO_4^-	333 (fe)	7.88491	/	Re-O	1.74346	Re (+2.203) O (-0.800)
IO_4^-	321 (fe)	8.69548	/	I-O	1.80181	I (+1.235) O (-0.559)
Cl^-	∼340 (afe)	2.34393	/	/	/	-1
Br^-	270 (afe)	3.76734	/	/	/	-1

* - Isotropic value for a static electric field,
** - Mean distance between central and all outer atoms,
fe: paraelectric-ferroelectric, afe: paraelectric-antiferroelectric

8.2 Comparison with other ferroelectric pyridinium salts

Anion properties in the whole family of pyridinium compounds were examined with the help of ab initio calculations. Results are listed in the Table 8.1. Figure 8.1 (right hand side) shows that the paraelectric-ferroelectric phase transition temperature increases with the specific unit cell volume. The trend is not linear and shows deviations for FSO_3^- and ReO_4^-. For the case of FSO_3^- it is conceivable that this is due to the presence of a significant dipole moment of the anion, as shown in Table 8.1. At first sight, such an increase with specific unit cell volume is unexpected. For the more voluminous anions the distance between pyridinium dipoles is larger, thus decreasing the direct electrostatic dipole-dipole interaction energy which can be balanced by thermal energy already at lower temperature so that the phase transition temperature should be expected to increase with *decreasing* unit cell volume. In the case of $PyClO_4$, $PyBF_4$ and

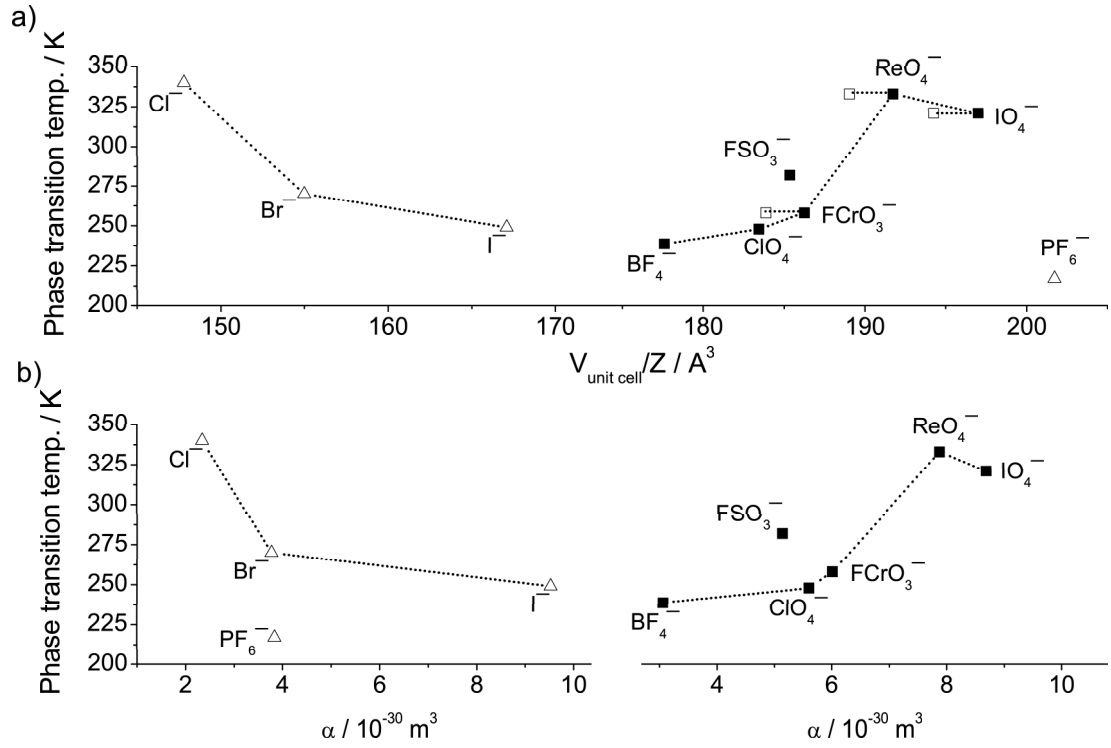

Figure 8.1: a) Order-disorder phase transition temperature vs. unit cell volume of the high temperature phase for antiferroelectric (△) and ferroelectric (■) pyridinium salts. Where known, the unit cell volume is also given for the phase below the ordering transition (□). b) Order-disorder phase transition temperature vs. polarizability of the anion for anitferroelectric (left) and ferroelectric salts (right).

$PyFSO_3$ sheets of coplanar cations are sandwiched between sheets of anions, and the anion diameter determines the distance between the cation sheets. In other cases the cations are slightly tilted, but the diameter of the anion still determines the distance between the cation sheets. The two-dimensional periodic structure with cation dipoles at the corners of equilateral triangles within one sheet is an arrangement of relatively low ferroelectric dipolar interaction energy which in the average between one dipole and its six nearest neighbours amounts to only 12.5% of its maximum possible value of one pair. In this situation it is conceivable that the coupling in the third dimension, between neighbouring cation sheets, is of crucial importance. The interspersed anions take a special role since they determine the distance between the cation sheets. Moreover, they play a more active role due to their polarizability which provides an indirect "super-exchange" coupling between the cation dipoles. When the cations are tilted,

this decreases the dipole-dipole interaction so that one should expect the ordering phase transition to occur at lower temperatures, which disagrees again with the experimental observations. The intermediate (ferroelectric) phase of $PyReO_4$, $PyIO_4$ and $PyFCrO_3$ is orthorhombic (still with non-coplanar cations). Despite these structural differences a systematic trend is observed, and these differences are probably responsible for the scatter in Figure 8.1a (right hand side). The unit cell volumes in Figure 8.1 are available for the paraelectric high temperature phase since the structures of the intermediate phases are often not known, but for some of the anions this information is available and given by an open symbol connected by a dotted line. It can be seen that these show the same trend. For a more precise discussion, anions should not be viewed as point charges, and cation dipole moments not as point dipoles since the distances between them are very small. In all compounds, the anions consist of a varying inner atom and of outer atoms which are almost exclusively oxygen atoms. Their partial charges which are given in Table 8.1 dominate the electrostatic interaction.

The anions are positioned more or less symmetrically about the cation. If the situation remains the same in the intermediate temperature phase than the interaction of the positive end of a cation dipole is always balanced by that of the negative end, and there is no net contribution of the anion to ordering. In the case of ReO_4^- the large deviation from the overall trend may be related to the very large partial charge of its outer atoms. A plausible explanation for the trend displayed in Figure 8.1 results from induced rather than permanent charges. This is demonstrated in Figure 8.1b (right hand side), which shows that the anion polarizability α exhibits a quite similar behaviour as a function of phase transition temperature as the unit cell volume. The anion polarization stabilizes both ends of a cation dipole and provides a super-exchange mechanism which stabilizes the ferroelectric phase so that the transition temperature in compounds with highly polarizable anions is higher. The anion polarizability might contribute to the antiferroelectric arrangement as well, but in the case of ferroelectric salts the contribution to the stabilization of the ferroelectric arrangement is much larger.

8.3 Comparison with nonferroelectric pyridinium salts

The high temperature phase of all pyridinium salts is found to be disordered. By comparing the nonferroelectric compounds PyCl, PyBr, PyI and $PyPF_6$[112] and the ferroelectric salts (Table 8.1) it is observed that with the exception of $PyPF_6$ the fer-

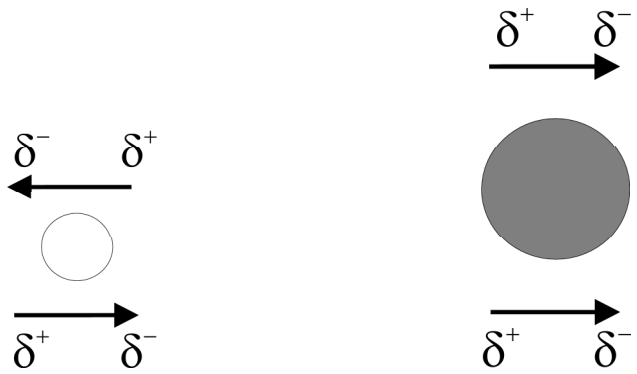

Figure 8.2: Left: direct coupling of the pyridinium cation sheets when the anion is small, right: indirect coupling when the anion is big. The arrow denotes the pyridinium cation dipole moment. δ^+ and δ^- denote the approximate positions of positive and negative partial charges.

roelectric ones have a much larger unit cell volume due to the larger anion diameters, resulting in a better separation of the cation layers. In fact, unlike for the ferroelectric compounds, among these nonferroelectric salts[112] the phase transition temperature decreases with increasing anion radius (Figure 8.1a, left hand side). An ordered antiferroelectric arrangement was observed in the low temperature phase of PyCl,[121] and the same has been suggested for other PyX salts as well (X = Br, I and PF_6).[112] The different behavior may be explained in the following way. When the cation sheets are separated above a certain distance, determined by the anion radius, the super-exchange interaction among cations dominates and causes ferroelectric ordering as shown in the Figure 8.2, right hand side. For the smaller anions the super-exchange interaction between cation sheets is decreased. In this case the energetically favoured arrangement is antiferroelectric where cation sheets interact directly as shown in the Figure 8.2, left hand side. Due to direct interaction of the cation sheets, the positive part of the cation dipole moment is positioned above the negative part of the cation dipole in the next sheet and the cation dipole moments are oriented in the opposite directions. The small anions have small polarizabilities as well, as seen in the Figure 8.1b, left hand side. $PyPF_6$ represents an exception from this behaviour. This anion is large (Figure 8.1a, right hand side) but it has a relatively small polarizability (Table 8.1 and Figure 8.1b, left hand side) due to the compact nature of the fluorine atoms. The partial charge on its peripheral atoms is the smallest among all pyridinium salts examined here. As it can be seen in Figures 8.1a and 8.1b, PyI and $PyBF_4$ are the border line cases. I^- has a large polarizability, but the distance between sheets is too small, and BF_4^- has a relatively small polarizability, but the distance between sheets is large, confirming that the distance between the cation sheets plays an important role. For $PyFCrO_3$ and

$PyReO_4$ the high temperature phase is paraelectric, the intermediate one is ferroelectric, but the order of the low temperature phase is antiferroelectric. This demonstrates that the behaviour of pyridinium salts is influenced by a delicate balance of numerous factors.

8.4 Phase transition order

$PyClO_4$ has two first-order phase transitions, $PyReO_4$ and $PyIO_4$ have second order-phase transitions while $PyBF_4$ is a limiting case,[65] and for other compounds, the phase transition order is not known. What influences the character of the phase transition is not clear. It was previously suggested that, with raising an applied pressure on PyI, PyBr, PyCl and PyF_6 salts, the phase transition would change to second order.[113] This is due to the disappearance of the phase transition volume change (which is typical for second-order phase transitions) with increasing external pressure, which has a similar effect as a chemical pressure. Chemical pressure arises due to the reduced anion radius and a smaller distance between the cation sheets.[113] The pyridinium rings of ferroelectric $PyClO_4$ and $PyBF_4$ in the high- and in the intermediate-temperature phases are coplanar, and the structural changes are known to be minimal. The cations in $PyReO_4$ and $PyIO_4$ are noncoplanar (tilted), and the paraelectric-ferroelectric phase transition is of second order. An arrangement where the positive partial charge of the pyridinium ring is directed toward the negative charge of the neighbouring pyridinium ring is energetically favoured.

It seems that the phase transition character is determined by the internal pressure in the crystal and the packing of the pyridinium rings as well. Better-packed crystals (canted cations) require a smaller structural rearrangement (insignificant phase transition volume change), and the phase transition is of second order.

8.5 Conclusions

The high polarizability of large anions is suggested to be a key property that is responsible for ferroelectric ordering by an *indirect* mechanism via superexchange, whereas compounds with small anions in which the *direct* cation dipole-dipole interaction dominates become antiferroelectric. This is revealed by correlations of the ordering phase transition temperatures with the anion polarizability and the anion size.

9 Summary

This work demonstrates how ordering of solvent molecules in the vicinity of the dipolar free radicals, in this case cyclohexadienyl type radicals, increases their methylene proton hyperfine coupling constants.

In the first part of this work the methylene proton hyperfine coupling constant of the cyclohexadienyl radical was measured in several neat solvents and solvent mixtures of different polarities. To explain the observed behaviour in dipolar liquids the dipole-dipole reaction field model of Reddoch and Konishi was used, which was previously developed to explain the solvent dependence of the ^{14}N hyperfine coupling constant in the di-tert-butyl-nitroxide radical. This model predicts that the hfc should be proportional to the solvent dipole moment concentration multiplied with the magnitude of the dipole moment and this behaviour was confirmed for the cyclohexadienyl radical. Ab initio calculations were carried out with the radical in an electric field to model the electric field due to the electric dipole moments of the surrounding solvent molecules. They show a linear dependence of the methylene proton hfc on the electric field, as was also suggested by the dipole-dipole reaction field model.

An extension of the dipole-dipole reaction field model to include the dipole-quadrupole interaction was developed here to account for the larger methylene proton hfc in benzene compared with octadecane, and it predicts that the hfc should be proportional to the concentration of quadrupole moments to the 4/3 power.

Comparison with the gas phase data permitted a separation of vibrational effects on the methylene proton hfc and revealed that ca. 28 % of the temperature dependence in water is due to increasing solvent disorder. The rest comes mainly from the intramolecular vibrations.

The next step in this work were studies of substituted cyclohexadienyl radicals, more precisely hydrogen adducts to 2-phenylethanol and 5-phenylpentanol. Methylene proton hyperfine coupling constants of these radicals were measured and in general their relative behaviour was similar and linear with the solvent polarity measured by the concentration of the dipole moments multiplied with the dipole moment magnitude. The behaviour of methylene proton hfcs of hydrogen adducts to 2-phenylethanol and

5-phenylpentanol can also be accounted for by a dipole-dipole reaction field model of Reddoch and Konishi. However some anomalies from linear behaviour of hydrogen adducts to 2-phenylethanol were observed. It was found that the conformation of the substituent group plays an important role contributing to the deviations from the linear behaviour. Exceptions from the linear behaviour were observed in some mixtures and were found to originate in preferential solvation in the vicinity of the dipolar radical. The largest deviations from linearity were observed for the para PEA-Mu radical in environments where no water molecules are present. More precisely a discontinuous increase of the methylene proton hyperfine coupling constant is observed in water containing solvent molecules. It was suggested that solute-solvent interactions originating in different hydrogen bonding effects lead to this deviation.

The behaviour of the methylene proton hyperfine coupling constants of the hydrogen adducts to 5-phenylpentanol is very similar to that of cyclohexadienyl radical. In the case of hydrogen adducts to 5-phenylpentanol the substituent group is much longer and its influence on the methylene proton hyperfine coupling constants is significantly decreased.

The next step was to study the conformations of the hydrogen adducts to 2-phenylethanol and 5-phenylpentanol. The aim was to investigate intramolecular hydrogen bonding between the hydrogen from the hydroxyalkyl substituent group and a π-electron system of the radical ring. This interaction causes the folding of the substituent group. A conformational study of hydrogen adducts to 2-phenylethanol and 5-phenylpentanol revealed that preferred position of the substituent group is eclipsed with the p_z orbital of the C_α atom at the phenyl ring. The differences originate due to the length of the substituent hydroxyalkyl group. In the case of hydrogen adducts to 2-phenylethanol, the dynamical balance between folded and non-folded conformation shifts towards the folded conformation in the water or in water containing mixtures. Results show that the methylene proton hyperfine coupling constant increases for the folded conformation. Therefore, it is concluded that the methylene proton hfc deviation from the linear dependence on the solvent polarity originates from the shift of the conformational balance in the direction of the folded conformation in water containing solvents. In the case of hydrogen adducts to 5-phenylpentanol the intramolecular hydrogen bonding is found to be insignificant due to the increased hydroxyalkyl substituent group length.

The behaviour of ferroelectric and thermodynamic parameters of pyridinium-perchlorate ($PyClO_4$) was simulated based on experimental NMR data and properties of the individual constituting ions. The dynamic ^2H NMR spectroscopy was used to

investigate the order-disorder character of ferroelectricity in $PyClO_4$. Quadrupole echo and inversion recovery experiments were performed in the range from 140 K to 300 K. The spectra can be simulated by a rotational jump motion of the pyridinium cations about their pseudo-C_6 axis. This confirms that the ferroelectricity of this compound below a first-order phase transition at 248 K is primarily due to the ordering of cations along a ferroelectric axis. In an intermediate phase between 248 K and 233 K the cation-anion sublattice displacement mechanism also gives a small positive contribution to ferroelectricity.

In the family of the ferroelectric pyridinium salts, the para-ferroelectric phase transition temperature increases with the size and polarizability of the constituting anions, revealing that the main interaction for ferroelectric ordering occurs via an indirect super-exchange mechanism, whereas in compounds with small anions of low polarizability the direct dipole-dipole interaction dominates and leads to antiferroelectric order.

Future work should be done in order to test the proposed dipole-quadrupole reaction field model. One of the options for performing this is by studying the cyclohexadienyl radical in mixtures of cyclohexane and benzene as these solvents are of similar shapes but of very different quadrupole moment values. This is important in order to avoid the preferential solvation in the vicinity of the cyclohexadienyl radical. It would be of great interest to monitor the behaviour of cyclohexadienyl type radicals with substituent groups containing no hydrophylic parts in various solvents. In this case it is expected that the deviations from linear behaviour are much smaller as no intramolecular hydrogen bonding takes place. A rigidity of the environment is expected to give very interesting effects on the conformation of the cyclohexadienyl type radicals and the conformational studies of these radicals in cell membrane-like environments would be very informative. In order to achieve large values of macroscopic polarization and higher paraelectric-ferroelectric phase transition temperatures the suggestion is to synthesise new ferroelectric molecular ionic crystals consisting of cations with large electric dipole moment values and of anions with large volumes and polarisabilities.

10 Zusammenfassung

10.1 Einleitung, Motivation und Methode

Freie Radikale spielen im täglichen Leben eine wichtige Rolle. Im menschlichen Immunsystem wirken sie gegen eindringende Bakterien und Viren.[1] Zellen nutzen freie Radikale zur Nachrichtenübermittlung untereinander.[1] Falls freie Radikale in zu hoher Konzentration vorhanden sind, können sie gesundheitsschädlich sein. Oxidative Beschädigung durch freie Radikale ist an der Entstehung vieler Krankheiten beteiligt.[2] Wenn wichtige Biomoleküle oxidiert werden, dann können sie, entgegen ihrer normalen Funktion, schädlich sein.[3] Freie Radikale haben eine große Bedeutung für viele Prozesse, die auch für industrielle Anwendungen wichtig sind, so z.B. bei der Synthese von Polymeren,[4] aber auch bei Abbau und Alterungsprozessen, wie die von Polymeren[5] und Brennstoffzellenmembranen[6] und allgemein bei der Materialalterung. Alle diese Vorgänge finden in der flüssigen oder in der amorphen Phase statt, daher ist es von großer Wichtigkeit, die zugrundeliegenden Wechselwirkungsmechanismen der Radikale mit der Umgebung zu verstehen.

Ein ausreichendes und systematisches Verständnis davon, wie die Molekülstruktur mit den physikalischen und den chemischen Eigenschaften eines Materials zusammenhängt, ist die Grundvoraussetzung für die Entwicklung von neuen Materialen und Prozessen. Eines der Ziele dieser Arbeit ist die Ermittlung der Beziehung zwischen den Eigenschaften und der Bewegung individueller Moleküle mit den Messungen der makroskopischen Phänomene. Für die praktische Verwendung von ferroelektrischen Salzen ist es am wichtigsten, ein Material zu synthetisieren, das Ferroelektrizität bei höchst möglicher Temperatur zeigt. Die Kontrolle der Phasen-Übergangstemperaturen in ferro- und antiferroelektrischen Materialen ist für viele Bereiche der Wissenschaft und der Industrie von Bedeutung.

In dieser Arbeit wurden die Methylenprotonen-Hfk ($A_{\mathrm{p}}^{\mathrm{met}}$) der Cyclohexadienyl-Radikale (C_6H_7), der Wasserstoffaddukte des 2-Phenylethanols (PEA-Mu) und des 5-Phenylpentanols (PPA-Mu) untersucht. Die Konformation der Radikale beeinflusst die Hyperfeinkoppelungskonstante (Hfk) und kann auch bei Radikalreaktionen eine große

Rolle spielen. Die bevorzugte Konformation kann durch Komplexbildung mit den Wasser-Molekülen geändert werden.[21,22] Deswegen wurden die Konformationsveränderungen von Wasserstoffaddukten des 2-Phenylethanols und 5-Phenylpentanols durch die Überwachung der β-Methylen-Hfk in polaren und unpolaren Flüssigkeiten untersucht. Im letzten Teil der Arbeit wurden Untersuchungen am feroelektrischen Pyridiniumperchlorat ($PyClO_4$) durchgeführt, sowie der Einfluss der Anionen in der Klasse der Pyridiniumsalze untersucht. Genauer gesagt, wurde die Beziehung zwischen der Ionenstruktur und die Phasenübergangstemperatur für ferro- und nichtferroelektrische Pyridiniumsalze untersucht.

Die Experimente in Rahmen dieser Arbeit wurden am Paul Scherrer Institut, Villigen, Schweiz und am Institut für Physikalische Chemie, Universität Stuttgart durchgeführt.

Um die Cyclohexadienyl-Radikale zu untersuchen, wurde die Methode der Myonenspinresonanz (μSR), genauer gesagt ihre Varianten "Avoided Level Crossing"- und "Transverse Field"-μSR (abgekürzt ALC-μSR und TF-μSR), genutzt.[32] Diese Methode ermöglicht eine sehr einfache Erzeugung und Überwachung der freien Wasserstoffaddukt-Radikale. Diese Methode ist mit der einzigartigen Eigenschaft des Myons begründet, ein großes magnetisches Moment zu besitzen. Das Myon kann daher in der Wissenschaft als magnetische Sonde eingesetzt werden. Es kann in den meisten Umgebungen ein Elektron abziehen und so das wasserstoffähnliche Atom Myonium bilden, das chemisch fast gleich dem normalen Wasserstoffatom ist.[32] Dieses Atom addiert sich an die Doppelbindungen organischer Moleküle und kann so ein Radikal bilden. Um die Pyridiniumsalze zu untersuchen, wurde die ^{2}H-NMR-Methode eingesetzt.[51] Diese Technik nutzt das große Quadrupolmoment des Deuteriumatoms. Die dritte verwendete Methode in dieser Arbeit waren ab initio Rechnungen.[7] Diese wurden überall dort eingesetzt, wo die experimentellen Methoden nicht ausreichten.

10.2 Lösungsmitteleffekte auf das Cyclohexadienyl-Radikal

Ein geeignetes Lösungsmittel kann die Reaktionsgeschwindigkeit und die Reaktionsausbeute wesentlich vergrößern.[3,9–11] Die Lösungsmitteleffekte auf die Radikale können über die Hfk beobachtet werden. Es wurden viele Untersuchungen von Lösungmitteleffekten auf stabile Radikale, wie zum Beispiel des Di-tertbutyl-nitroxid-radikals (DTBN) durchgeführt. Die Lösungsmitteleffekte wurden typisch durch verschiedene

Kontinuumsmodelle beschrieben,[12] die als Vorbild die Modelle von Onsager[13] und Kirkwood[14] genutzt haben. Alle diese Modelle verwenden die Dielektrizitätskonstante als die Größe, die die Lösungsmitteleffekte bestimmen. Zum Beispiel wurde in den Untersuchungen von Al-Bala'a et al. ein Kontinuumsmodell verwendet. Dabei ergab sich, dass die Hfk mit (ε-1)/(ε+1) korreliert, wobei ε die Dielektrizitätskonstante des Lösungsmittels ist.[15] Vor kurzem wurde die konventionelle theoretische Kontinuumsbeschreibung der dipolaren Lösungsmittel erweitert, um die Effekte zu berücksichtigen, die durch das molekulare Quadrupolmoment des Lösungsmittels verursacht werden.[16] Diese Beschreibung wurde jedoch noch nicht auf freie Radikale angewendet.

Die großten Mängel des Kontinuumsmodells sind, dass die Wechselwirkungsenergie in Funktion der Dielektrizitätskonstante zu schnell sättigt und dass explizite Wechselwirkungen zwischen den gelösten Molekülen und den Lösungsmittelmolekülen vernachlässigt werden. Eine detailiertere Beschreibung der Mängel findet sich in der Literatur.[17] Das Kontinuumsmodell lässt sich durch die Einführung einer lokalen Dielektrizitätskonstanten verbessern,[18] allerdings verliert die Dielektrizitätskonstante so ihre Bedeutung, da sie als Bulk-Eigenschaft definiert ist.

Reddoch und Konishi (RK) entwickelten ein Dipol-Dipol-Reaktionsfeldmodell für die Beschreibung der Lössungsmitteleffekte auf die ^{14}N-Hfk des DTBN-Radikals.[17] Mittels der modifizierten Hückelmolekülarorbital-Methode haben RK bewiesen, dass die ^{14}N-Hfk vom elektrostatischen Potentialunterschied zwischen dem Sauerstoff- und dem Stickstoff-Atom linear abhängig ist. Die Substituentengruppen schützen die NO-Gruppe von allen Raumsrichtungen außer von einer. Deswegen ist es möglich den Einfluss aller Moleküle zu vernachläsiggen, außer derer, die auf der Achse der NO-Gruppe liegen. Auf diese Weise haben RK das Reaktionsfeld im Zentrum der NO-Gruppe berechnet und festgestellt, dass die ^{14}N-Hfk von der Dipolemomentkonzentration multipliziert mit der Große des Dipolmoments, dem [μ_S]-Parameter, linear abhängig ist. Dieses Modell wurde als Basis für diese Arbeit genutzt.

Im erstem Teil der Arbeit wurde A_p^{met} des C_6H_7-Radikals in Lösungmitteln und Mischungen verschiedener Polaritäten gemessen. Es wurde gezeigt, dass die A_p^{met} zu [μ_S] direkt proportional sind (Bild 4.5), mit der Ausnahme des Benzols, das nicht auf der Trendgerade liegt. Dieses Verhalten ist so, wie es das RK-Dipol-Dipol-Reaktionsfeldmodell erwarten läßt.

Um die Gültigkeit dieses Modells zu bestätigen wurden ab initio Rechnungen durchgeführt. Es wurde gezeigt, dass A_p^{met} dem elektrischen Potentialunterschied zwischen den Methylen- und dem Para-Kohlenstoff (in Bild 4.2 definiert) direkt proportional ist (Bild 4.6). Dadurch sind die beiden Voraussetzungen des RK-Modells

gegeben. Aus diesen Gründen kann man feststellen, dass das RK-Modell für das Cyclohexadienyl-Radikal anwendbar ist.

Ein weiteres Ergebnis war, dass die $A_{\mathrm{p}}^{\mathrm{met}}$-Veränderung teilweise durch die Änderung der Struktur im elektrischen Feld verursacht wird, nämlich zu ≈15% der gesamten Veränderung (Bild 4.6).

Für den Fall von C_6H_7 in Benzol wurde das RK-Modell für quadrupolare Flüsigkeiten erweitert. Das Quadrupolmoment des Lösungsmittelmoleküls ist in diesem Modell die für die Wechselwirkung entscheidende Moleküleigenschaft. Dieses Modell sagt voraus, dass die $A_{\mathrm{p}}^{\mathrm{met}}$ von der Quadrupolmoment-Konzentration hoch $4/3$ abhängig ist (Gleichung 4.15).

Die Temperaturabhängigkeit von $A_{\mathrm{p}}^{\mathrm{met}}$ wurde besonders für den Fall des C_6H_7-Radikals in Wasser untersucht. Es wurde gezeigt, dass die $A_{\mathrm{p}}^{\mathrm{met}}$-Veränderung von den größeren Vibrationsamplituden (≈68% des Effekts), der größern Unordnung (temperaturverursacht; ≈28% des Effekts) und der Veränderung der Lösungsmitteldichte (≈4% des Effekts) verursacht wird.

Der Ansatz, der diesen Untersuchungen zu Grund liegt, hat im Vergleich zum klassischen Kontinuumsmodell[15,30] einige Vorteile. Er berücksichtigt, dass sich die Hfk in Lösungsmitteln ähnlicher Dielektrizitätskonstante stark unterscheiden können. Dieser Ansatz ist in besserer Übereinstimmung mit den experimentellen Ergebnissen. Er ist auch allgemeiner anwendbar, da er den Einfluß des elektrischen Feldes auf die Radikale erklärt, was nicht nur in Flüssigkeiten von Bedeutung ist.

Dieser Ansatz erklärt, wie es möglich ist, ein großes Reaktionsfeld in den nicht-dipolaren Lösungsmitteln mittels Molekülen mit großen elektrischen Multipolmomenten zu erreichen. Das kann wichtig für chemische Reaktionen sein, wenn die Reaktandenlöslichkeit in polaren Lösungsmiteln begrenzt ist.[8]

Das Dipol-Dipol-Reaktionsfeldmodell und seine Erweiterung auf Dipol-Quadrupol-Wechselwirkungen sollte auch für andere Moleküle und Radikale gültig sein. Diese Radikale sollten konformativ stabil sein, weil die Konformationsveränderungen oft größere Effekte auf die Hfk haben können.[23] Diese Radikale sollten auch ein großes Dipolmoment besitzen, um eine Teilordnung in ihrer Umgebung zu verursachen.

10.3 Lösungsmitteleffekte auf Wasserstoffaddukte des 2-Phenylethanols und des 5-Phenylpentanols

Im zweiten Teil der Arbeit wurde die Anwendbarkeit des RK-Modells auf die substituierten Cyclohexadienyl-Radikale untersucht. Auch die Untersuchung des Einflusses der Substituenten-Gruppe auf die Hfk der substituierten Cyclohexadienyl-Radikale wird hier beschrieben. In diesem Teil der Arbeit wurde $A_{\mathrm{p}}^{\mathrm{met}}$ für die Wasserstoffaddukte (Myoniumaddukte) des 2-Phenylethanols (PEA-Mu) und des 5-Phenylpentanols (PPA-Mu) bestimmt. In Abhängigkeit von dem Additionsort des Wasserstoffatoms (Myoniumatoms) am Phenylring entstehen drei verschiedene Radikale: para (Additionsort: Para-Ringkohlenstoffatom), ortho (Additionsort: Ortho-Ringkohlenstoffatom) und meta (Additionsort: Meta-Ringkohlenstoffatom).[90]

Es wurde gezeigt, dass $A_{\mathrm{p}}^{\mathrm{met}}$ zu $[\mu_{\mathrm{S}}]$ direkt proportional ist (Bilder 5.5 und 5.6), wie es das RK-Modell voraussagt. Es gibt aber einige Abweichungen vom idealen Verhalten. Die größten Abweichungen ergeben sich in Lössungsmitteln, die Wasser enthalten, besonders für das Para-PEA-Mu-Radikal. In diesem Fall wird ein diskontinuierlicher Sprung der $A_{\mathrm{p}}^{\mathrm{met}}$ beobachtet (Bild 6.2). $A_{\mathrm{p}}^{\mathrm{met}}$ zeigt für PPA-Mu-Radikale ein sehr ähnliches Verhalten wie für das C_6H_7-Radikal (Bild 5.6).

Die Abweichungen vom idealen Verhalten wurden durch die bevorzugte Solvatation und unterschiedliche intramolekulare Wasserstoffbrückenbindungen verursacht. Die Störung der π-Elektronen auf dem Phenylring, die von der OH-Grupppe verursacht wird, ist umso kleiner je länger die Hydroxyalkyl-Substituentenkette ist. Die Untersuchungen, in denen diese Radikale verwendet wurden, um die Verteilungskoeffizienten der gelösten Moleküle zwischen der flüssigen und der Bilayer-Phase zu bestimmen, machen es wünschenswert, diese Effekte zu verstehen.[19,20,100]

10.4 Konformationsuntersuchungen der Wasserstoffaddukte des 2-Phenylethanols und des 5-Phenylpentanols

In diesem Teil der Arbeit wurde gezeigt, dass ALC-μSR zu Konformationsuntersuchungen in Umgebungen verschiedener Polarität nutzbar ist. Die ALC-μSR-Resonanzen der "in-plane"- und β-Methylen-Protonen der PEA-Mu-Radikale und PPA-Mu-Radikale wurden hier erstmals identifiziert und angegeben. Besondere Beachtung findet

A_{p}^{β} der PEA-Mu-Radikale in Wasser und Oktadekan und der PPA-Mu-Radikale in Methanol und Oktadekan. Über die McConnell-Gleichungen kann man aus dem A_{p}^{β}-Temperaturverhalten Information über die Konformation des Radikals erhalten.[45]

Aus der positiven Temperaturabhängigkeit von A_{p}^{β} ergibt sich, dass die günstigste Konformation die ist, bei der die Substituentengruppe und das p_z-Orbital des C_α-Atoms des Phenylrings eclipsed zueinander stehen. Ab initio-Rechnungen der ortho-, para- and meta-PEA-Mu-Radikale in der Gasphase zeigen, dass die gefaltete Konformation die stabilste ist. Die gefaltete Konformation ist die Form der PEA-Mu-Radikale, bei der die OH-Gruppe mit den π-Elektronen des Phenylrings wechselwirken kann (Bild 6.1 links). Ab initio Rechnungen der ortho-, para- and meta-PEA-Mu-H_2O-Cluster zeigen dieselben Ergebnisse. Daraus kann man ableiten, dass Wasser die gefaltete Konformation aller PEA-Mu-Radikale stabilisiert.

Es wurde festgestellt, dass die sterischen Hinderungen der Methylen-Protonen im ortho-PEA-Mu-Radikal, die stärkere intramolekulare Wasserstoffbrücke des para-PEA-Mu-Radikal und die Unterschiede im einfach besetzten Molekülorbital die Ursachen für das unterschiedliche Verhalten der PEA-Mu-Radikale sind, die in vorherigen Teil dieses Arbeits (Sektion 10.3) beschrieben sind.

Die positive Temperaturabhängigkeit von A_{p}^{β} der PPA-Mu-Radikale zeigt auch, dass die Substituentengruppe meistens eclipsed zum p_z-Orbital des C_α-Atoms des Phenylrings steht. Ab initio Rechnungen von ortho-, para- und meta-PPA-Mu-Radikalen in der Gasphase zeigen, dass die ungefaltete Konformation stabiler ist. In Verbindung mit den A_{p}^{β}-Ergebnissen bedeutet das, dass die intramolekulare Wasserstoffbrückenbindung in diesem Fall nicht von Bedeutung ist.

Es wurde auch nachgewiesen, dass die Konformation und die Komplexierung mit Lösungsmittelmolekülen großen Einfluss auf das einfach besetztes Molekülorbital der Cyclohexadienyl-Radikale haben können.

10.5 Ferroelektrizität des Pyridiniumperchlorats

Die Pyridiniumsalze stellen ein ausgezeichnetes Beispiel sowohl für die Untersuchung der Orientierungsunordnung als auch für den Ursprung von Ferroelektrizität dar. Das Pyridinium-Kation ist ein Molekül mit einem großen elektrischen Dipolmoment. Die Symmetrie ähnelt der des Benzolmoleküls, was die theoretische Behandlung vereinfacht. Der Ordnungs-unordnungs-Mechanismus der Ferroelektrizität des $PyClO_4$ wurde mittels des Modells von Beck et al. hier besonders untersucht.[65]

Ferroelektrische Pyridinium-Salze weisen zwei fest-fest-Phasenübergänge auf. Der erste (bei höherer Temperatur) Unordnungs-Ordnungs-Phasenübergang findet zwischen einer paraelektrischen und einer ferroelektrischen Phase statt. Der zweite Phasenübergang (Unordnung-Ordnung) passiert in der ferroelektrischen Phase.

Die ^{2}H-NMR Spektren (Quadrupol-Echo- und Inversion-Recovery) des $PyClO_4$ konnten quantitativ unter der Annahme einer Rotations-Sprung-Bewegung um die pseudo C_6-Achse[65] simuliert werden (Bilder 7.5 und 7.7). Die Hochtemperaturphase oberhalb 248 K ist völlig ungeordnet, da die Pyridinium-Kationen schnelle Sprünge zwischen den gleichbesetzten Orientierungen unternehmen. In der mittleren- und in der Niedrigtemperatur-Phase findet die Bewegung zwischen ungleich besetzten Orientierungen statt. Mit sinkender Temperatur wird die Bewegung behindert, das führt bei 140 K zu nahezu statischen und vollorientierten Kationen.

Die Korrelation zwischen aus den ^{2}H NMR-Spektren ermittelten Kationensorientierungen und der makroskopischen Polarisation (Bild 7.9) zeigte, dass die Ferroelektrizität des $PyClO_4$ durch die Orientierung der Kationdipolemoments entsteht. Die mittlere Phase ist teilweise ungeordnet, aber die Umorientierung der Kationen findet so statt, dass das durchschnittliche Dipolmoment in Richtung der ferroelektrischen Achse nicht null wird (Bild 7.9). Die Verschiebung des Ionenuntergitters führt zusätzlich zu einem kleinen positiven Beitrag zur makroskopischen Polarisation (Bild 7.10).

Die Wärmeabgabe während der Abkühlung kommt zum größten Teil aus der Ordnung des Kationendipolmoments (Bild 7.11). Der Unterschied zwischen der freigesetzten Wärme an der Phasenübergangstemperatur und der Wärme, die zur Ordnung der Kationen notwendig ist, kommt von anderen möglichen Prozessen, wie Gitterdeformation oder Anion-Anordnung.

10.6 Vergleich mit anderen ferroelektrischen und nicht-ferroelektrischen Pyridiniumsalzen

Die para-ferroelektrischen Phasenübergangstemperaturen in der Klasse der Pyridiniumsalze wurden verglichen, und der Einfluss der Anionen auf die Ferroelektrizität wurde mit Hilfe von ab initio Rechnungen untersucht. In der Klasse der Pyridiniumsalze sind die "Träger" der Ferroelektrizität die elektrischen Dipolmomente der Pyridiniumkationen. Die Anionen haben einen bestimmenden Einfluss auf die Phasenübergangstemperatur, da die Kationen immer gleich sind.

Bei ferroelektrischen Pyridiniumsalzen steigt die Phasenübergangstemperatur mit

zunehmendem spezifischem Volumen der Elementarzelle (Volumen der Elementarzelle geteilt durch Zahl der Ionenpaare; abgekürzt V_{Zelle}), wie in Bild 8.1a gezeigt ist. Bei nichtferroelektrischen Pyridiniumsalzen ist das V_{Zelle} kleiner und die Phasenübergangstemperatur sinkt mit zunehmendem V_{Zelle}. Für ferroelektrische und nichtferroelektrische Salze besteht zwischen der Phasenübergangstemperatur und der Polarisierbarkeit ein ähnlicher Zusammenhang (Bild 8.1b).

Es wurde vorgeschlagen, dass die hohe Polarisierbarkeit der großen Anionen die wichtigste Voraussetzung zur Entstehung der ferroelektrischen Ordnung über den *indirekten* Mechanismus via Superwechselwirkung ist. Im Gegensatz dazu werden Stoffe mit kleinen Anionen antiferroelektrisch, wenn die *direkte* Kationen-Dipol-Dipol Wechselwirkung dominant ist.

Bibliography

[1] Guzik, T. J.; Korbut, R.; Adamek-Guzik, T. *Journal of Physiology and Pharmacology* **2003,** *54,* 469.

[2] Rhodes, C. J. *Toxicology of the Human Environment - the critical role of free radicals;* Taylor and Francis: London, 2000.

[3] Lazar, M.; Klimo, V.; Rychly, J.; Pelikan, P. *Free Radicals in Chemistry and Biology;* CRC Press: Boca Raton, Florida, USA, 1989.

[4] Trost, B. M.; Fleming, I. *Comprehensive Organic Synthesis;* Pergamon: Oxford, UK, 1991.

[5] Mitov, S.; Panchenko, A.; Roduner, E. *Chem. Phys. Lett.* **2005,** *402,* 485 and references therein.

[6] Panchenko, A.; Dilger, H.; Kerres, J.; Hein, M.; Ullrich, A.; Kaz, T.; Roduner, E. *Phys. Chem. Chem. Phys.* **2004,** *6,* 2891 and references therein.

[7] Levine, I. N. *Quantum chemistry;* Prentice Hall Inc.: New Jersey, USA, 2000.

[8] Reichardt, C. *Solvents and solvent effects in organic chemistry;* VCH: Weinheim, Germany, 1988.

[9] Litwinienko, G.; Ingold, K. U. *J. Org. Chem.* **2004,** *60,* 5889.

[10] Yorimitsu, H.; Nakamura, T.; Shinokubo, H.; Oshima, K.; Omoto, K.; Fujimoto, H. *J. Am. Chem. Soc.* **2000,** *122,* 11041.

[11] Li, C. J.; Chen, L. *Chem. Soc. Rev.* **2006,** *35,* 68.

[12] Tomasi, J.; Mennucci, B.; Cammi, R. *Chem. Rev.* **2005,** *105,* 2999 and references therein.

[13] Onsager, L. *J. Am. Chem. Soc.* **1936,** *58,* 1486.

[14] Kirkwood, J. G. *J. Chem. Phys.* **1934,** *2,* 767.

[15] Al-Bala'a, I.; Bates, R. D. *J. Mag. Reson.* **1987,** *73,* 78.

[16] Jeon, J.; Kim, H. J. *J. Chem. Phys.* **2003,** *119,* 8606.

[17] Reddoch, A. H.; Konishi, S. *J. Chem. Phys.* **1979,** *70,* 2121.

[18] Marsh, D. *Eur. Biophys. J.* **2002,** *31,* 559.

[19] Scheuermann, R.; Tucker, I. M.; Dilger, H.; Staples, E. J.; Ford, G.; Fraser, S. J.; Beck, B.; Roduner, E. *Langmuir* **2004,** *20,* 2652.

[20] Martyniak, A.; Scheuermann, R.; Dilger, H.; Tucker, I. M.; Burkert, T.; Hashmi, A. S. K.; Vujoševič, D.; Roduner, E. *Physica B* **2006,** *374-375,* 328.

[21] Mons, M.; Robertson, E. G.; Snoek, L. C.; Simons, J. P. *Chem. Phys. Lett.* **1999,** *310,* 423.

[22] Mons, M.; Robertson, E. G.; Simons, J. P. *J. Phys. Chem. A* **2000,** *104,* 1430.

[23] Krusic, P. J.; Meakin, P.; Jesson, J. P. *J. Phys. Chem.* **1971,** *75,* 3438.

[24] Abe, H.; Terauchi, M.; Matsuda, A.; Shuto, S. *J. Org. Chem.* **2003,** *68,* 7439.

[25] Zalar, B.; Laguta, V. V.; Blinc, R. *Phys. Rev. Lett.* **2003,** *90,* 37601-1.

[26] Scott, J. F. *Springer series in advanced microelectronics: Ferroelectric memories;* Springer: Berlin, Germany, 2000.

[27] Francombe, M. H., Ed.; *Handbook of film devices: Ferroelectric film devices;* volume 5 Academic: New York, USA, 2000.

[28] Estupiñán, E.; Villenave, E.; Raoult, S.; Rayez, J. C.; Rayez, M. T.; Lesclaux, R. *Phys. Chem. Chem. Phys.* **2003,** *5,* 4840.

[29] Fleming, D. G.; Shelley, M. Y.; Arseneau, D. J.; Senba, M.; Pan, J. J.; Roduner, E. *J. Phys. Chem. B* **2002,** *106,* 6395 and references therein.

[30] Owenius, R.; Engström, M.; Lindgren, M.; Huber, M. *J. Phys. Chem. A* **2001,** *105,* 10967.

[31] Percival, P. W.; Kiefl, R. F.; Kreitzman, S. R.; Garner, D. M.; Cox, S. F. J.; Luke, G. M.; Brewer, J. H.; Nishiyama, K.; Venkateswaran, K. *Chem. Phys. Lett.* **1987,** *133,* 465.

[32] Roduner, E.; Reid, I. D. *Israel Journal of Chemistry* **1989,** *29,* 3.

[33] Yu, D.; Percival, P. W.; Brodovitch, J. C.; Leung, S. K.; Kiefl, R. F.; Venkateswaran, K.; Cox, S. F. J. *Chem. Phys.* **1990,** *142*, 229.

[34] Fleming, D. G.; Arseneau, D. J.; Pan, J. J.; Shelley, M. Y.; Senba, M.; Percival, P. W. *Appl. Magn. Reson.* **1997,** *13*, 181.

[35] Thall, E. *J. Chem. Educ.* **1996,** *73*, 481 and references therein.

[36] Roduner, E. *Appl. Magn. Reson.* **1997,** *13*, 1.

[37] Roduner, E. *Physica B* **2003,** *326*, 19.

[38] Pajak, Z.; Maluszynska, H.; Szafranska, B.; Czarnecki, P. *J. Chem. Phys.* **2002,** *117*, 5303.

[39] Tolkachev, V. A.; Molin, Y. N.; Tchkeidze, I. I.; Buben, N. Y.; Voevodsky, V. V. *Dokl. Akad. Kauk. S.S.S.R.* **1961,** *141*, 911.

[40] Fessenden, R. W. *J. Chem. Phys.* **1963,** *38*, 773.

[41] Barnes, R. G. *Deuteron quadrupole coupling tensors in solids;* J. A. S. Smith: 1974 p. 335.

[42] Alam, T. M.; Drobny, G. P. *Chem. Rev.* **1991,** *91*, 1545.

[43] Spiess, H. W. *Adv. Polym. Sci.* **1985,** *66*, 23.

[44] Harriman, J. E. *Theoretical foundations of electron spin resonance;* Academic Press: New York, 1978.

[45] McConnell, H. M. *J. Chem. Phys.* **1956,** *24*, 764.

[46] Straka, M.; Kaupp, M.; Roduner, E. *Theor. Chem. Acc.* **2005,** *114*, 318.

[47] Roduner, E. *The positive muon as a probe in free radical chemistry: potentials and limitations of the μSR technique. Lecture notes in chemistry, vol. 49;* Springer-Verlag: Germany, 1988 and references therein.

[48] R. Scheuermann, PhD thesis, 1997, University of Stuttgart.

[49] Lectures of Prof. Dr. E. Roduner and Dr. I. McKenzie, University of Stuttgart.

[50] Brodovitch, J. C.; Addison-Jones, B.; Ghandi, K.; McKenzie, I.; Percival, P. W.; Schüth, J. *Can. J. Chem.* **2003,** *81*, 1.

[51] Fyfe, C. A. *Solid state NMR for Chemists;* CFC Press: Ontario, Canada, 1983.

[52] Ernst, R. R.; Bodenhausen, G.; Wokaun, A. *Principles of Nuclear Magnetic Resonance;* Clarendon: Oxford, 1987.

[53] Mehring, M. *Principles of High Resolution NMR in Solids;* Springer-Verlag: Berlin, 1983 second edition.

[54] Lectures of Prof. Dr. K. Müller, University of Stuttgart.

[55] Schmieder, J.; Müller, K. *J. Phys. Chem. A* **1998,** *102,* 1181.

[56] Greenfield, M. S.; Vold, R. L.; Vold, R. R. *Mol. Phys.* **1989,** *66,* 269.

[57] Meirovitch, E.; Krant, T.; Vega, S. *J. Phys. Chem.* **1983,** *87,* 1390.

[58] Poupko, R.; Furman, E.; Müller, K.; Luz, Z. *J. Phys. Chem.* **1991,** *95,* 407.

[59] Grant, G. H.; Richards, W. G. *Computational chemistry;* Oxford University Press: Oxford, UK, 1995.

[60] Szabo, A.; Ostlund, N. S. *Modern quantum chemistry: Introduction to advanced electronic structure theory;* McGraw Hill: 1989.

[61] Koch, W.; Holthausen, M. C. *A chemist's guide to density functional theory;* Wiley-VCH: Weinheim, Germany, 1999.

[62] Hohenberg, P.; Kohn, W. *Phys. Rev.* **1964,** *136,* B864.

[63] "MINUIT-Function Minimization and Error Analysis, CERN Program Library Entry D506", .

[64] Heaton, N. J.; Vold, R. R.; L.Vold, R. *J. Magn. Res.* **1988,** *77,* 572.

[65] Beck, B.; Villanueva-Garibay, J. A.; Müller, K.; Roduner, E. *Chem. Mat.* **2003,** *15,* 1739.

[66] Beck, B. PhD thesis, University of Stuttgart, 2003.

[67] Szafraniak, I.; Czarnecki, P. *J. Phys.: Condens. Matter* **2002,** *14,* 3321.

[68] Personal communication with P. Czarnecki.

[69] Maluszynska, H.; Scherf, C.; Czarnecki, P.; Cousson, A. *J. Phys.: Condens. Matter* **2003,** *15,* 5663.

[70] Frisch, M. J. *et al.* "Gaussian 98, Revision A.11", 2001.

[71] Improta, R.; Barone, V. *Chem. Rev.* **2004,** *104,* 1231.

[72] Frisch, M. J. *et al.* "Gaussian 03, Revision B.04", 2003.

[73] Hay, R. J.; Wadr, W. R. *J. Chem. Phys.* **1985,** *82,* 270.

[74] Hay, R. J.; Wadr, W. R. *J. Chem. Phys.* **1985,** *82,* 284.

[75] Bader, R. F. W.; Keaveny, I.; Cade, P. E. *J. Chem. Phys.* **1967,** *47,* 3381.

[76] Lovas, F. J. *J. Phys. Chem. Ref. Data* **1978,** *7,* 1445.

[77] Griller, D. *J. Am. Chem. Soc.* **1978,** *100,* 5240.

[78] Chipman, D. *J. Phys. Chem.* **1992,** *96,* 3294.

[79] Abe, T.; Tero-Kubota, S.; Ikegami, Y. *J. Phys. Chem.* **1982,** *86,* 1358.

[80] Meyer, E. A.; Castellano, R. K.; Diederich, F. *Angew. Chem. Int. Ed.* **2003,** *42,* 1210 and references therein.

[81] Raschke, T. M.; Levitt, M. *Proc. Natl. Acad. Sci. USA* **2005,** *102,* 6777.

[82] Keutsch, F. N.; Saykally, R. J. *Proc. Natl. Acad. Sci. USA* **2001,** *98,* 10533.

[83] Schwager, M.; Roduner, E.; Reid, I. D.; Kreitzman, S. R.; Percival, P. W.; Brodovitch, J.-C.; Leung, S.-K.; Sun-Mack, S. *Z. Phys. Chem.* **1995,** *190,* 29.

[84] Schwager, M.; Dilger, H.; Roduner, E.; Reid, I. D.; Percival, P. W.; Baiker, A. *Chem. Phys.* **1994,** *189,* 697.

[85] Chelli, R.; Cardini, G.; Ricci, M.; Bartolini, P.; Righini, R.; Califano, S. *Phys. Chem. Chem. Phys.* **2001,** *3,* 2803.

[86] Buckingham, A. D. *Q. Rev. Chem. Soc.* **1959,** *13,* 183.

[87] Cabaco, M. I.; Danten, Y.; Besnard, M.; Guissani, Y.; Guillot, B. *J. Phys. Chem. B* **1997,** *101,* 6977 and references therein.

[88] Battaglia, M. R.; Buckingham, A. D.; Williams, J. H. *Chem. Phys. Lett.* **1981,** *78,* 421.

[89] Mathematica 5.2, Wolfram Research, Inc.

[90] Scheuermann, R.; Tucker, I. M.; Creeth, A. M.; Dilger, H.; Beck, B.; Roduner, E. *Phys. Chem. Chem. Phys.* **2002,** *4,* 1510.

[91] Schneider, H. . In *Solute-Solvent Interactions*; Coetzee, J. F.; Ritchie, C. D., Eds.; Dekker: New York, 1969 vol. 1 p. 301.

[92] Frankel, L. S.; Langfor, C. H.; Stengle, T. R. *J. Phys. Chem.* **1970,** *74,* 1376.

[93] Hinton, J. F.; Amis, E. S. *Chem. Rev.* **1967,** *67,* 367.

[94] Popov, A. I. . In *Solute-Solvent Interactions*; Dekker: New York, 1976 vol.2, p. 271.

[95] Dimroth, K.; Reichardt, C. *Z. Anal. Chem.* **1966,** *215,* 344.

[96] Dawber, J. G.; Ward, J.; Williams, R. A. *J. Chem. Soc., Faraday Trans. 1* **1988,** *84,* 713.

[97] Wypich, G. *Handbook of Solvents;* ChemTec Publishing: Toronto, Canada, 2001 and references therein.

[98] Bagno, A. *J. Phys. Org. Chem.* **2002,** *15,* 790 and references therein.

[99] Dixit, S.; Crain, J.; Poon, W. C. K.; Finney, J. L.; Soper, A. K. *Nature* **2002,** *416,* 829.

[100] Martyniak, A.; Dilger, H.; Scheuermann, R.; Tucker, I. M.; McKenzie, I.; Vujoševiċ, D.; Roduner, E. *Phys. Chem. Chem. Phys.* **2006,** *8,* 4723.

[101] Godfrey, P. D.; Jorissen, R. N.; Brown, R. D. *J. Phys. Chem. A* **1999,** *103,* 7621.

[102] Barnard, K.; Hargrave, K. R.; Higgins, G. M. C. *J. Chem. Soc.* **1956,** 2845.

[103] v. R. Schleyer, P.; Wintner, C.; Trifan, D. S.; Backsai, R. *Tetrahedron Lett.* **1959,** *14,* 1 and references thereein.

[104] Mateos, J.; Cram, D. J. *J. Am. Chem. Soc.* **1959,** *81,* 2756.

[105] Kirchner, H. H.; Richter, W. Z. *Phys. Chem. Neue Folge* **1972,** *81,* 274.

[106] Spassov, S. L.; Simenov, M. F.; Randall, E. W. *J. Mol. Struct.* **1981,** *77,* 289.

[107] Dickinson, J. A.; Hockridge, M. R.; Kroemer, R. T.; Robertson, E. G.; Simons, J. P.; McCombie, J.; Walker, M. *J. Am. Chem. Soc.* **1998,** *120,* 2622.

[108] Fischer, H. *Z. Naturforsch.* **1965,** *20a,* 428.

[109] Isaacs, E. D.; Shukla, A.; Platzman, P. M.; Hamann, D. R.; Barbiellini, B.; Tulk, C. A. *J. Phys. Chem. Solids* **2000,** *61,* 403.

[110] Hübner, G.; Roduner, E. *J. Mater. Chem.* **1999,** *9,* 409.

[111] Behar, D.; Rabani, J. *J. Phys. Chem.* **1988,** *92,* 5288.

[112] Ripmeester, J. A. *Can. J. Chem* **1976,** *54,* 3453.

[113] Szafranski, M.; Szafraniak, I. *J. Phys.: Condens. Matter* **2003,** *15,* 5933 and references therein.

[114] Czarnecki, P.; Wasicki, J.; Pajak, Z.; Goc, R.; Maluszynska, H.; Habrylo, S. *J. Mol. Structure* **1997,** *404,* 175.

[115] Maluszynska, H.; Czarnecki, P.; Lewicki, S.; Wasicki, J.; Gdaniec, M. *J. Phys.: Condens. Matter* **2001,** *13,* 11053.

[116] Wasicki, J.; Czarnecki, P.; Pajak, Z.; Nawrocik, W.; Sczepanski, W. *J. Chem. Phys.* **1997,** *107,* 576.

[117] Pajak, Z.; Czarnecki, P.; Maluszynska, H.; Szafranska, B. *J. Chem. Phys.* **2000,** *113,* 848.

[118] Wasicki, J.; Kozak, A.; Pajak, Z.; Czarnecki, P.; Belushkin, A. V.; Adams, M. A. *J. Chem. Phys.* **1996,** *105,* 9470.

[119] Pajak, Z.; Grottel, M.; Koziol, A. *J. Chem. Soc. Faraday Trans. 2* **1982,** *78,* 1529.

[120] Wasicki, J.; Pajak, Z.; Kozak, A. *Z. Naturforsch.* **1990,** *45a,* 33.

[121] Rerat, P. *Acta Cryst.* **1962,** *15,* 427.

List of abbreviations and symbols

ALC-μSR	Avoided Level Crossing Muon Spin Resonance
TF-μSR	Transverse Field Muon Spin Resonance
PEA	2-phenylethanol
PPA	5-phenylpentanol
Ortho PEA-Mu	Ortho muonium adduct to 2-phenylethanol
Para PEA-Mu	Para muonium adduct to 2-phenylethanol
Meta PEA-Mu	Meta muonium adduct to 2-phenylethanol
Ortho PPA-Mu	Ortho muonium adduct to 5-phenylpentanol
Para PPA-Mu	Para muonium adduct to 5-phenylpentanol
Meta PPA-Mu	Meta muonium adduct to 5-phenylpentanol
Ortho PEA-H	Ortho hydrogen adduct to 2-phenylethanol
Para PEA-H	Para hydrogen adduct to 2-phenylethanol
Meta PEA-H	Meta hydrogen adduct to 2-phenylethanol
Ortho PPA-H	Ortho hydrogen adduct to 5-phenylpentanol
Para PPA-H	Para hydrogen adduct to 5-phenylpentanol
Meta PPA-H	Meta hydrogen adduct to 5-phenylpentanol
Hfc	Hyperfine coupling constant
A_{μ}^{met}	Methylene muon hyperfine coupling constant
$A_{\mathrm{p}}^{\mathrm{met}}$	Methylene proton hyperfine coupling constant
A_{p}^{β}	β-methylene proton hyperfine coupling constant
% *aq.char.*	% aqueous character
$\rho_{\mathrm{p}}^{\mathrm{met}}$	Spin population at methylene proton
$\rho_{\mathrm{p}}^{\mathrm{o}}$	Spin population at ortho in-plane ring proton
$\rho_{\mathrm{p}}^{\mathrm{m}}$	Spin population at meta in-plane ring proton
$\rho_{\mathrm{p}}^{\mathrm{p}}$	Spin population at para in-plane ring proton
RK	Reddoch and Konishi
C_6H_7	Cyclohexadienyl radical
DTBN	di-tert-butyl-nitroxide radical
D_2O	Deuterated water
MeOH	Methanol

EtOH	Ethanol
PrOH	Propanol
ButOH	Buthanol
HexOH	Hexanol
OctOH	Octanol

List of Figures

List of Tables

Acknowledgments

This work was performed in Paul Scherrer Institute, Villigen, Switzerland and in the Institute of Physical Chemistry, University of Stuttgart, Stuttgart, Germany.

First of all I want to thank to Prof. Dr. Emil Roduner for his active engagement and numerous inspiring scientific discussions. These were especially helpful during all phases of the work and in broadening the scope of my scientific interests.

Coaching of Prof. Dr. Klaus Müller during the NMR part of the work is gratefully acknowledged. His active support and experience in this field were of great importance in improving the quality of this part of the work.

Taking the chair of the examination board of Prof. Dr. Wolfgang Kaim is kindly acknowledged.

Without the support of Dr. Herbert Dilger, Dr. Robert Scheuermann, Dr. Iain McKenzie and Aleksandra Martyniak during the measurements at the Paul Scherrer Institute finishing this work would have been impossible. Without all of them the measurements at the Paul Scherrer Institute would have been not as pleasant as they were.

Excellent conditions for these measurements provided by Dr. Ulrich Zimmermann and Dr. Aleksey Stoykov from the Paul Scherrer Institute are gratefully acknowledged. I thank Dr. Thomas Handel and Dr. Jorge Antonio Villanueva-Garibay for support during NMR experiments.

The discussions with Prof. Dr. Martin Kaupp, Prof. Dr. Thomas Schleid, Dr. Bettina Beck, Dr. Eva Zurek and Dr. Stefan Jagiella were very inspiring. Members of the Graduate College on Modern Methods of Magnetic Resonance in Material Science as well as colleagues from the Institute of Physical Chemistry contributed to a pleasant working atmosphere and to interesting scientific discussions.

Financial support by the Deutsche Forschunggemeinschaft within the Graduate College on Modern Methods of Magnetic Resonance in Materials Science is gratefully acknowledged.

And last but not least, the support and encouragements of my parents, brother and of my friends during this work were of invaluable importance to me and they are gratefully acknowledged.

Danksagung

Diese Arbeit wurde im Paul Scherrer Institut in Villingen, Schweiz und im Institut für Physikalische Chemie der Universität Stuttgart in Stuttgart, Deutschland durchgeführt.

Zunächst möchte ich mich bei Prof. Dr. Emil Roduner bedanken für sein aktives Engagement und unzählige inspirierende wissenschaftliche Diskussionen. Diese haben mir in allen Phasen meiner Arbeit sehr geholfen und haben mein Blickfeld für wissenschaftliche Sachfragen erweitert.

Herzlich möchte ich mich bei Prof. Dr. Klaus Müller für die Einarbeitung auf dem NMR während dieser Phase der Arbeit bedanken. Seine Unterstützung und Erfahrung waren von großer Bedeutung in dieser Arbeitsphase.

Ich danke auch Prof. Dr. Wolfgang Kaim für den Vorsitz des Untersuchungsausschusses.

Ohne die Unterstützung von Dr. Herbert Dilger, Dr. Robert Scheuermann, Dr. Ian McKenzie und Alexandra Martyniak während der Messungen im Paul Scherrer Institut wäre die Vollendung meiner Arbeit unmöglich gewesen. Ohne sie wären die Messungen im Paul Scherrer Institut keinesfalls in einer solch angenehmen Atmosphäre verlaufen.

Ein großer Dank gilt Dr. Ulrich Zimmermann und Dr. Aleksey Stoykov vom Paul Scherrer Institut, die für die hervorragenden Messbedingungen verantwortlich sind. Ich danke auch Dr. Thomas Handel und Dr. Jorge Antonio Villanueva-Garibay für die Unterstützung während der NMR Experimente.

Die Diskussionen mit Prof. Dr. Martin Kaupp, Prof. Dr. Thomas Schleid, Dr. Bettina Beck, Dr. Eva Zurek und Dr. Stefan Jagiella waren für mich eine große Inspiration. Den Mitarbeitern des Instituts für Phyikalische Chemie sowie den Mitgliedern des Graduiertenkollegs Magnetische Resonanz gebührt mein Dank für die äußerst angenehme Arbeitsatmosphäre und interessante wissenschaftliche Diskussionen.

Für die finanzielle Unterstützung möchte ich der Deutschen Forschungsgemeinschaft innerhalb des Graduiertenkollegs Magnetische Resonanz einen großen Dank aussprechen.

Und zu guter Letzt danke ich meinen Eltern, meinem Bruder und Freunden für die unschätzbare Unterstützung und Ermutigung während meiner Arbeit.